Chapter 3 Results and discussion of the resistive switching properties in the HfOx-based memory devices

3.1 Introduction

Resistive switching induced by an applied electric field has been extensively studied for its potential application in the resistance random access memories (RRAM). The RRAM offers a possibility of high density integration, lower power operation, easier down-scaling and CMOS (complementary metal-oxide-semiconductor) compatibility [1-4]. As one of the reported material, HfO_2 has been actively studied for its low operation current (as low as to 25 uA), high on/off resistance ratio (> 1000), fast switching speed (5 ns), satisfactory switching endurance (> 10^6 cycles), and long retention time (10 years extrapolated at 200 °C) compared to the other binary transition metal oxides such as NiO and MgO, which lend them to serve as candidates a basis for future-generation oxide-based RRAM technologies [5].

3.2 Experimental details

Resistive memory devices were fabricated as follows. TiN metal as a bottom electrode was deposited on an 8 inch Si wafer by sputtering. Then, nonstoichiometric HfO_x films with a thickness from 5 to 20 nm were deposited by atomic layer deposition (ALD) (ASM, Polygon 8200) at temperature of 300 °C. Hafnium tetrachloride ($HfCl_4$) and water (H_2O) with a compositional ratio of 5:2 and 5:3 were both used as reactants for HfO_x deposition. The primitive chemical-formula is shown as follows.

$$HfCl_4 + 4H_2O \rightarrow Hf(OH)_4 + HCl \uparrow \quad (3\text{-}1)$$

$$Hf(OH)_4 \text{ heating} \rightarrow HfO_2 + H_2O \quad (3\text{-}2)$$

After stacking HfO_x thin films on the bottom electrodes, various kinds of metals as top electrodes were deposited by dc sputtering using a shadow mask at room temperature, such as Pt, Pd, Cu, Ni, Ti, Al and etc. The thickness of metals was varied from 30 to 100 nm. For a further investigation on the effect of the reactive metal Al, the stacked top electrodes Pt/Al were also fabricated with the thickness of Al varied from 5-100 Å. To study the area dependence of the electrical properties, the circular top electrodes were formed with radiuses of 100-800 μm.

To investigate the rapid thermal annealing (RTA) effects on the HfO_x-based memory device, RTA treatment from 400 to 500 °C are treated on the HfO_x-based memory device in N_2 or O_2 ambient for 30, 60, or 90 seconds, respectively. Eventually, a 100-nm-thick Ni top electrode with a diameter of 200 μm was patterned through a metal mask to form a sandwich structure by a dc sputtering.

To fabricate the RRAM device, platinum (Pt) as a top electrode was deposited by sputtering using a shadow mask at room temperature. The thickness of Pt was about 60 nm. The surface morphology of HfO_x/TiN/Si samples was examined by atomic force microscopy (AFM) in tapping mode, and the composition depth profiles of HfOx films were carried out by X-ray photon-electron spectroscopy (XPS). Grazing incident-angle X-ray diffraction (GIAXRD) was adopted to characterize the crystal structure of HfO_x. The microstructure of the Pt/HfO_x/TiN/Si structure was investigated by cross-sectional transmission electron microscopy (XTEM) operated at 200 keV (Philips F20). The electrical properties of the RRAM devices were measured using a HP4284 LCR meter and a HP4156C semiconductor parameter analyzer. During measurement, the voltage was applied to the Pt electrode and the TiN electrode was grounded. The dielectric constant and current density of the HfO_x films were found to be ~21 and $1x10^{-8}$ A/cm^2 at 1V, respectively.

3.3 Unipolar resistive switching properties of HfOx thin films

3.3.1 Bulk HfOx films effect

In the beginning, we fabricated the HfO_x films with different reacting gas composition for investigation. Hafnium tetrachloride ($HfCl_4$) and water (H_2O) with a compositional ratio of 5:2 and 5:3 were used as reactants for HfO_x deposition. We defined the samples fabricated with compositional ratio of 5:2 and 5:3 as H5-2 and H5-3, respectively. Fig. 3-1 shows the electroforming characteristics of the two samples. A leakage current about 10 pA @ 1 V and forming voltage about 6 V can be observed on both the two samples. No obvious difference can be observed besides the fluctuant current curve. The H5-3 samples exhibit large fluctuant behavior during the I-V curves than that of H5-2 one. Fig. 3-2 shows the resistance values distribution of the two samples. A smaller high to low resistance ratio and short-lived resistive switching behavior can be observed on H5-3 samples, while the H5-2 samples can be continuously operated over 100 cycles without fatigue. Fig. 3-3 and 3-4 compares the operation voltage distribution of the H5-2 and H5-3 sample, respectively. As we can clearly see from the two figures, the voltage distribution on H5-2 samples is much dense than that of H5-3, indicating that the H5-2 is more prefer for the resistive switching memory application. Different compositional ratio of reactants for HfOx deposition may cause different thin film properties, grain size, crystallinity, and the electrical characteristics, which may be the main reason for the distinction switching properties.

3.3.2 Top electrode effect

As for the unipolar resistive switching (RS) mechanism, there are two main mechanisms suggested in the literature for the resistive switching. One is the filamentary mechanism where the formation and rupture of conducting paths are due

to the oxygen vacancy (defect control), which depends on the applied voltage [6,7]. This is from the characteristics of the bulk oxide film. Some groups further claimed that the rupture of the filament paths occurs at the anodic oxide films of about 3-10 nm [8]. This mechanism has been used to explain the unipolar RS in a variety of binary oxide materials such as NiO [9], TiO_2 [8], and HfO_2 [10]. The other one is the effect of the interface in the metal-insulator-metal (MIM) structure including the potential barrier height from the metal work function and the Fermi level of the oxide layer. Based on this mechanism, some of the unipolar RS behaviors could be elucidated such as NiO [11], TiO_2 [12], and Cu_2O [13]. The unipolar RS of NiO and TiO_2 films could both be explained by one or two of the above model. For the HfO_x films, though many experimental results have explained that the HfO_x films belongs to the filamentary mechanism [10], however, the electrode material dependence on the RS properties of HfO_x films has not been reported. For a universal understanding on the RS mechanism of the RRAM device, a detail investigation on the electrode effect to the HfOx films is essential to be studied. In this section, the dependence of the switching properties of HfO_x films on the top electrode material was evaluated for (top electrode)/HfO_x/TiN structure with various top electrode material such as Pt, Cu, Ni, Ti, and Al. The effect of the interfacial reactions and interlayer formation was also investigated.

The resistance value of the as-grown HfO_x film was in the initial resistance state (IRS). Before the RS operation, forming process was needed for these samples by applying a larger voltage (forming voltage). The purpose of forming process was to initiate the switching properties of HfO_x/TiN RRAM devices, and then the state could be switched from IRS to low resistance state (LRS). At LRS, current level can be higher than compliance current (CC) and then the film was switched to an HRS. The operation from high resistance state (HRS) to LRS and from LRS to HRS is denoted

as SET and RESET process. CC was always needed for the HfO_x films during the SET process to avoid completely breakdown of the HfO_x films. Fig. 3-5 compares the typical I-V characteristics of the Pt, Ni, Ti/HfO_x/TiN structures. From this figure, we clearly observed that the unipolar RS can be performed when using these three electrode materials, even there is a little difference on the switching parameters between the three samples. But there was no RS behavior observed on Al/HfO_x/TiN (AH) structure. In addition, in order to examine the reliability characteristic of the RS behaviors, the repetitive RS was tested. The resistance values of the Pt/HfO_x/TiN (PH), Ni/HfO_x/TiN (NH), and Ti/HfO_x/TiN (TH) samples in the HRS and LRS versus the number of switching cycles at 0.1 V reading voltage was measured and the results were shown in Fig. 3-6. The PH samples exhibit the short-lived RS properties and switching-failure among the several times of switching cycles, while the resistance values in both states are stable on NH and TH samples. The values of the resistance ratio measured at the bias voltage of 0.1 V are ~160 and 18 for the NH and TH samples, and switching cycles are 250 and 30 times for the NH and TH samples, respectively. We rationally suggest that the distinction on the RS characteristics was attributed to the different electrode metals and a different electrode has been found to cause a change in the underneath layer's stoichiometric material properties. So, a detailed investigation at the M/O interface is the ongoing project.

The effects of the top electrode material to the RS properties have been discussed by many groups and are mainly focused on two factors of metal itself. (1) One is the effect of the interface between the metal and the oxide film which is related to the carrier injection. In the case of the p-type binary oxide such as NiO [11], and Cu_2O [13], it was reported that an ohmic contact or a low Schottky barrier was needed to apply an effective electric field to the oxide film high enough to induce trapping or detrapping at defect states. In this case, RS was not observed for a well-defined

Schottky contact at the interface. As opposed to above, the RS of PCMO was observed with only Schottky contact [14]. Kim et al. proposed that the top electrode which have higher work function (WF) than TiO_2 (4.05 eV) is essentially of the Schottky type to demonstrate a unipolar RS phenomenon [12]. Interestingly, the HfO_x samples in this study did not show similar RS characteristics as reported above. Fig. 3-7 presents the log (I/V)-$V^{1/2}$ curves for the PH, NH, TH, and AH devices. The current level was measured up to the point where the soft breakdown occurred from the HRS. HfO_x film is known as an n-type (2.8 eV) wide-band-gap semiconductor due to oxygen vacancies, therefore, both high (Pt, 5.65 eV) and low (Ti, 4.33 eV) WF of the top electrodes deposited on HfO_x samples can form a well-defined Schottky barrier between the Pt/HfO_x and Ti/HfO_x interface, thus performing the unipolar RS characteristics. However, for the Al/HfO_x/TiN (AH) sample, no RS characteristic is observed after forming process even if there is Schottky barrier formed between Al/HfO_x shown in Fig. 3-7. Table 3-1 lists the comparison between the WF and RS parameters of various metal materials. All kinds of metal materials used as top electrode in this study on HfO_x film exhibits the unipolar RS characteristics, besides Al. Among the observed data, the work function and contact difference singly could not explain this RS phenomenon as the reported NiO, TiO_2, and Cu_2O films [11-13].

(2) Another factor is the electronegativity and free energy for oxygen. Hasan et al. proposed that under a positive bias, electromigration of oxygen ions forms thicker oxide layer, which dissociates under a negative bias, cause high and low resistance states, respectively. Afterwards, Lee et al. proposed that the importance of the reaction at the metal/NiO interface is demonstrated in relation to the free energy of oxide formation of electrode metals and Ni [15]. From the Ellingham diagram [16], we know that the free energies for oxide formation of the metal Ni, Cu, Ti, Al and Hf at RT is about -240.6, -167.4, -944.8, -1678.2, and -1113.5 kJ/mol, respectively. Once

reactive metal (with low free energy) contacts with oxide layer, these metal electrodes will easily react with the underlayer's oxide film and form an interfacial layer at the M/O interface. To further confirm the interface reaction and diffusion between the electrode and the HfO_x film, XPS and Auger depth profile were obtained as shown in Fig. 3-8. From Fig. 3-8(a), the XPS spectrum obtained from Pt layer, it was confirmed that there was no oxidation in the film. From Fig. 3-8(c) obtained from AES depth profile of the device structure, diffusion/oxidation at the interface was not observed when Pt was used as a top electrode. Also it can be confirmed that HfO_x layer is well contained between the top and bottom electrodes. On the other hand, reaction and interdiffusion at the M/O interface were observed when Ni, Ti, and Al were used as top electrode. In the case of the TH structure, TiO_y was observed at the interface from XPS spectrum, as shown in Fig. 3-8(b) and 3-8(d), obtained from AES depth profile shows that titanium oxide was formed at the Ti/HfO_x interface. Under the unipolar RS, the oxygen ions extracted to the top electrode under the field effect during SET process, and back to reoxidize with the HfO_x film by the Joule heating effect during RESET process is the proposed switching mechanism for the unipolar RS phenomenon [17]. In addition, the oxygen ions migration between the electrode and HfO_x film under the applied voltage is responsible for whether the SET or RESET operation succeeds or not. And the residual thickness of about 3-10 nm oxide layer beneath the anode electrode dominates the resistance values of HRS and LRS [8]. That is to say, a distinct thin oxide layer beneath the anode electrode between M/O causes the significant difference on the electrical characteristics. Therefore, we rationally suggest that the distinction on the RS properties was attributed to the difference of the free energy for oxygen, which will form an interfacial layer (IL) at the M/O interface. This IL composition depends on metal's free energy for oxygen, implying the competition between metal electrode and Hf for oxygen would occur at

the interface [15]. This is a key issue to dominate whether if the RS behavior exists. When using Pt as top electrode, oxygen ions extracted from HfO_x film during the positive operation could not be confined near the conducting filamentary paths. The non-oxidizing property of Pt provides the easy movement of oxygen ions or atoms along the grain boundaries to the atmosphere, and it possesses the random distribution of oxygen ions for the short-lived switching behaviors, as shown in Fig. 3-6. However, for the metal with free energy for oxygen a little higher than Hf, such as Cu, Ni and Ti, oxygen ions are confined near the conducting filament paths by oxidizing with the reactive anode during the SET process. This is confirmed from the XPS data as shown in Fig. 3-8(c). During RESET process, the oxidized oxygen atoms can back to reoxidize with HfO_x film and result in rupture of the conducting filaments because of Joule heating. For the Al electrode, the formation energy of Al_2O_3 is much lower than that of HfO_2. The oxygen atoms are more willing to react with Al than that of Hf, resulting in the tendency of forming conducting paths but not rupture them under the same polarity of positive applied bias. Furthermore, the bonding of Al-O is stronger than that of Hf-O [18], which causes the bonding between Al and O hard to break under Joule heating during the RESET process. Therefore, an Al_2O_3 layer will be formed at the Al/HfO_x interface but the oxygen atoms are hard to back to reoxidize with HfO_x, which results in no RS behavior. Although the Ti electrode can form TiO_y at many different ionic states from x=1 to near 2 with different electric properties, such as conductivity and free energy for oxygen, however, the fluctuant ionic states of TiO_y at the M/O interface can guarantee easy movement of oxygen ions inside TiO_y film to accompany the rupture of the conducting paths. So, there still RS exists. However, the random distribution on the composition of TiO_y film causes degradation on the switching stability and endurance. Among the experimented data, the Ni electrode is the most suitable metal for HfO_x film because of its free energy for

oxygen is negative and is still larger than Hf metal. Furthermore, the diffusivity of Ni inside HfO_x film is quite low. So, a more stable and reliable RS properties would be obtained on NH samples.

The distribution of the SET and RESET voltage in the case of dc sweep of NH and TH was measured, as shown in Fig. 3-9. The amount of oxygen ions absorbed and extracted by Ni top electrode is better controlled compared to other metal top electrodes. Lee et al. have claimed that the variations in the conduction band offset (CBO) for the Ru/HfO_2 interface may be attributed to the variation in the oxygen concentration at the Ru/HfO_2 interface during the switching cycles, which causes a wide fluctuation of the operation voltage [10]. Therefore, the more dispersed operation voltage is rationally suggested that owing to the existence of many different ionic states of TiO_y film. Fig. 3-10 shows the retention characteristics of the NH and TH sample in both HRS and LRS measured at RT. Both of them on NH sample are stable at 0.1 V reading voltage for more than 30000 s. A little gradual decrease on HRS is observed on NH, but a high to low resistance ratio about 2 orders of magnitude can be kept, as shown in Fig. 3-10, indicating the potential for nonvolatile memory applications. However, the HRS data failed quickly on TH sample for less than 2000 s. This might be attributed to the gradual change on the interface layer beneath anode electrode under the continuous positive bias stress, because the TiO_x film will easily change its ionic state and over-extract oxygen ions from the HfO_x film. The electrode effect is a key issue for a reliable and endurable RS characteristic.

3.3.3 Modified resistive switching behavior of HfOx using Pt/Al stacked top electrode

In this section, the electrical characteristics of HfO_x film was investigated by inserting Al thin layer between Pd/HfO_x interface. HfO_x and Al materials exhibit good

compatibility with standard CMOS technology, low cost, and low leakage current due to high band gap of HfO_x, which serves as a good candidate for RRAM application. In addition, we can modulate the composition of anodic oxide layer of HfO_x film by depositing Al layer above it to improve thermal stability of HfO_x film. TEM and XPS depth profile analysis were used to reveal the information at the interface of Al/HfO_x layer. A HfAlO laminate was observed to be formed above HfO_x film to play an important role in terms of resistance switching behaviors and endurance property. Correlation between the thickness of the Al thin layer and the resistive switching properties were also studied.

$Pd/HfO_x/TiN$ (PH) and $Pd/Al(50\ Å)/HfO_x/TiN$ (A50H) samples both show RS behavior after forming process, and the electrical characteristics operated by a continuous dc voltage sweep are shown in Fig. 3-11(a) and 3-11(b), respectively. A continuous dc voltage sweep method by an automatic measurement program is used to measure the I-V curves of the two samples. It is obviously noticed that I-V curves with successive memory switchings are greatly stabilized by inserting Al thin layer at Pd/HfO_x interfaces. Furthermore, we observed a very good stability and reproducibility even after an I-V sweep of up to 100 cycles shown in Fig. 3-11(b). Compared with the PH samples, not only the resistive switching stabilizes considerably, but also the endurance enhances significantly. This result can be reconfirmed by replotting the switching parameters with the accumulation percentage as shown in Fig. 3-12(a). The state switches from high resistance state (HRS) to low resistance state (LRS) and from LRS to HRS is defined as SET and RESET process, and the voltage values when SET or RESET occurs are called V_{set} or V_{reset}. Resistance values of LRS and HRS is named as R_{on} and R_{off}. The improvements are especially obvious in dispersions of V_{set} and V_{reset}. A switch failure phenomenon, which is a failure of switching from R_{off} state to R_{on} state by applying V_{set} or R_{on} state to R_{off}

state by applying V_{reset}, observed several times in PH samples effectively disappears by Al layer inserted. The switch failure result in readout disturbance of 0 or 1 state at 0.4 V shown in left side of Fig. 3-12(b). A current reading at 0.4 V reveals about 30 times of resistive change of A50H sample shown in Fig. 3-12(b). A great improvement on the electrical characteristics of RS behavior only by inserting Al thin film in the Pd/HfO_x interface, indicating the reactive metal is beneficial for improvement of voltage dispersion.

On the basis of the proposed switching mechanism, the unipolar switching property is considered to be due to the formation and rupture of conducting filaments at the anodic side of insulator film [10]. From the previous literature reports, the instability of unipolar switching characteristics mainly attributed to the variation in the oxygen concentration at the top electrode/HfO_x interface during switching cycles [10]. We suggest that the improvement of the RS characteristics by inserting Al layer at the Pd/HfO_x interface contribute to forming a HfAlO laminate above HfO_x film to stabilize the oxygen concentration during switching. During SET process, oxygen ions or atoms are extracted to anode. For PH sample, the non-oxidizing property of Pd guarantees easy movement of oxygen ions or atoms along grain boundaries, which possesses random distribution of oxygen ions for the fluctuant switching behaviors. In contract to this, Al is an aggressively reactive metal with low Gibbs free energy for the formation of Al_2O_3 film (-1678.2 kJ/mol) [19], so that a thin interfacial layer will be formed at the Al/HfO_x interface under applied positive bias, but not observed on Pd/HfO_x sample. When oxygen atoms are extracted to anode, they are confined near the conducting filaments terminals by oxidizing with the inserted Al metal [20], so that the oxygen concentration at the interface during each cycle can be maintained. Fig. 3-13 shows the cross-sectional TEM image of A35H sample after several RS cycles. A clearly bright gray layer above HfO_x film can be identified as the HfAlO

thin layer from EDX analysis. From the literature, some reports have revealed that when Al were doped inside HfO_2 film, the HfAlO compound layer was suggested to formed in the interface because this laminate would be thermodynamically favorable, and needs the lowest formation energy [21-23]. We believe that this HfAlO laminate is beneficial and very critical for the stable properties.

Then, a continuous positive bias is applied to the anode to perform the RESET process. The conducting filaments thermally disrupted which leads to rearrangement of the atom distribution under joule heating with high temperature. For PH sample, since HfO_x has low crystallization temperature about 400 °C, which is much lower than that of joule heating temperature during RESET process of 700 K [24], so crystallization of HfO_x near anode can be easily induced locally during RESET process. Because of its low crystallization temperature, the fluctuant and distributed filaments inside HfO_x matrix easily triggered the SET or RESET process, which causes a random fluctuation of RS properties during switching process, as shown in Fig. 3-11(a). The grain boundaries in crystallized HfO_x can be the fast paths for electron conduction which results in easy breakdown of the dielectric films. Once Al thin layer is inserted at the Pd/HfO_x interface, this new-formed HfAlO layer not only serves as an oxygen source or sink to preserve the oxygen atoms near conducting filaments [21], but also increases the binding strength with oxygen atoms compared to Hf-O [18]. Higher thermal stability of HfAlO layer can effectively prevent the thermal noise against the unintentional stimulus, so the RS characteristics will be much better than that of PH sample. This can well explain why the RS property of PH is much unstable compared to A35H sample.

To have a clear understanding about the influence of different thick of Al layer on the switching characteristics, Pd/Al/HfO_x/TiN structure with different thickness of inserted Al thin layer in the range of 20-200 Å is experimented. The initial off-state

resistances (R_{off}) of all the as-grown films do not show difference at the same voltage. Forming process is needed in the beginning to activate the RS behavior, and the forming voltage for all samples is about 5.5 V. This implies that the as-grown samples with different inserted Al layer exhibit almost identical dielectric strength before forming. Fig. 3-14(a) compares the I-V curves of Pd/Al/HfO_x capacitor with different thickness of inserted Al layer of 35, 70, 100 and 150 Å (A35H, A70H, A100H, and A150H). Samples with inserted Al layer in the range of 20-100 Å all exhibits RS properties, while loses switching characteristics when Al thickness is larger than 100 Å. A continuous dc voltage measurement is also performed automatically to test the switching reliability of A35H, A70H, and A100H sample, respectively. Fig. 3-14(b) presents the reliance of the resistance on the repetitive switching cycles of PA35H, PA70H, and PA100H sample. As is shown from this figure, a very good stability and reproducibility even after an I-V sweep of up to 4000 cycles is observed on A35H sample, however, for A70H and A100H sample, only 500 and 400 switching cycles is obtained. Although samples with Al inserted layer ranging from 20 to 100 Å all demonstrate stable and reproducible RS with little voltage dispersion, but only when samples in the range of 20-35 Å thickness of inserted Al layer exhibit longer endurance than others. We suggest that the different Al layer thickness above HfO_x film modulates the properties and composition of interface layer during switching variously, which results in distinction of the switching characteristics.

The influence of different thickness of Al layer on the RS characteristics is discussed here. X-ray photoemission spectroscopy (XPS) depth profile was used to examine our MIM structure. Fig. 3-15(a) and 3-15(b) are the depth profiles of Al 2p core level XPS spectra of A35H and A150H samples after several switching cycles, respectively. The spectrum of the bottom (top) in Fig. 3-15(a) and 3-15(b) describes the top (bottom) Pd electrode. As shown in Fig. 3-15(a), the peak of the two spectra

assigned (denoted as A and B) to the location of alumina peak (74.7 eV), which indicates that the inserted Al thin layer is almost fully oxidized after switching. The spectra B is also analyzed its O 1s spectra for further confirmation, and the data is shown in Fig. 3-15(b). Deconvolution has been conducted to fit the spectra into the two peak (530.7 and 531.7 eV), which correspond to HfO_2 and Al_2O_3 states, respectively. These results are consistent with our previous elucidation that a HfAlO laminate will be formed in the Al/HfO_x interface to improve the RS characteristics. There is something needed to be noted that both the spectra A and B could be deconvoluted into the two oxide peak. For A150H sample, different phenomenon is demonstrated. As shown in Fig. 3-15(c), two peaks at 72.9 eV and 74.7 eV are both observed on different Al 2p spectra. Al 2p spectra at steps C, D and E exhibit a stronger peak at lower binding energy of 72.9 eV and a weaker peak at high binding energy of 75.3 eV. Peak at binding energy of 72.9 eV represents the metal Al, but the peak at 75.3 eV may be composed of various non-fully oxidized Al with different states. For the Al 2p spectra at steps F,G and H near HfO_x film, peak at 72.9 eV disappears, but peak at 74.7 eV gets stronger. This main peak shift from 72.9 eV to 74.7 eV indicates that the Al thin layer near HfO_x is oxidized after operation, while the rest remains the metal Al signal. O 1s spectra of step H is also analyzed and deconvoluted to fit the spectra into the two spectra of HfO_2 and Al_2O_3 states, respectively, as shown in Fig. 3-15(d). The O 1s spectra of A35H and A150H sample could be well fitted to HfO_2 and Al_2O_3 peak, and the A35H sample with a composition ratio of 66.6% and 33.4%, while the PA150H one is about 77.7% and 22.3%. Observation of the different composition ratio of the interfacial HfAlO layer can provide critical clues for understanding the endurance issue between A35H and A150H sample. Al is regarded to easily deprive oxygen atoms from HfO_x film, especially under repetitive positive bias. Therefore, once thicker Al layer is inserted at

the Pd/HfO_x interface, there would be some additional Al thin layer lay above HfAlO film, as shown in Fig 3-15(c). The excess Al will continuously vary the Al/HfAlO interface along with every switching cycle, which gradually alters the atomic composition of the self-formed HfAlO during every cycle and causes the endurance issue. Therefore, the oxygen concentration in the interface could be less stable, and degrades the endurance performance.

3.3.4 Rapid thermal annealing effect on HfOx thin films

(a) Under N_2 ambient

Fig. 3-16(a)-(c) shows the surface roughness of HfO_x thin films under different Ar RTA treatment conditions. The surface roughness of the samples of as-grown, Ar 400 °C for 90 s, and Ar 500 °C for 90 s, in room mean square (RMS) is about 4.03, 4.47, and 4.67 nm, respectively. Fig. 3-17 compares the forming process I-V curves of Ni/HfO_x/TiN sample on the as-deposited, RTA at 500 °C in Ar ambient for 30, 60 and 90 seconds. As we can clearly see that the RTA treatment time in Ar ambient is positively related to leakage current before forming process, indicating that the components and/or the related stoichiometry of the HfO_x thin film are altered. From X-ray diffraction analysis as shown in Fig. 3-18(a), the crystallinity increases with increasing the annealing temperature for longer time. In addition, we clearly confirm that the HfO_x film crystallizes in different orientation when samples are treated at 500 °C for 3 minutes in Ar ambient, as shown in Fig. 3-18(b). Therefore, we suggest that the leakage current increasing may be attributed to the crystallization of the HfOx film, because the crystallization temperature of HfO_x film was reported to be about 500 °C.

Fig. 3-19 demonstrates the resistive switching (RS) I-V curves of as-grown, RTA at 400 °C and 500 °C in Ar ambient for 90 seconds under 0.5 mA CC. The resistance

value of the as-grown HfO_x film was in the initial resistance state (IRS). Before the RS operation, forming process was needed for these samples by applying a larger voltage (forming voltage). The purpose of forming process was to initiate the switching properties of HfO_x/TiN RRAM devices, and then the state could be switched from IRS to low resistance state (LRS). At LRS, current level can be higher than compliance current (CC) and then the film was switched to an HRS. The operation from high resistance state (HRS) to LRS and from LRS to HRS is denoted as SET and RESET process. CC was always needed for the HfO_x films during the SET process to avoid completely breakdown of the HfO_x films. To find out the temperature effect to the memory reliability, we measured the RS characteristics by an automatic continuous measurement system up to 100 switching cycles. Fig. 3-20 shows the resistance values of as-grown, RTA at 400 °C and 500 °C in Ar ambient for 90 seconds on the HfO_x/TiN structure in the HRS and LRS versus the number of switching cycles at 0.1 V reading voltage. With the annealing temperature increases, the LRS resistance reduces monotonically while the HRS resistance becomes fluctuant distribution among the 100 switching cycles. Fig. 3-21 demonstrates the voltage distribution of the three samples in the SET and RESET operation continuously. A large variation was observed on the samples treated with RTA at 500 °C in Ar ambient for 90 seconds, while the as-grown one was quite stable even after 100 switching cycles.

Based on the proposed model, the formation and rupture of the conducting filamentary paths are well explained the switching mechanism of the HfO_x films owing to the abrupt decrease on the conducting current [17]. When samples are annealed at high temperature, the composition and/or the stoichiometry of HfO_x films may be altered according to the material property, and this was confirmed from Fig. 3-18(b). HfO_x films are well known to have low crystallization temperature of about

500 °C and the reports have shown that it crystallizes even under 400 °C for a period of time. This may be the main causes on the great increasing of the conducting current before forming. Furthermore, we also observed that when the oxide films are partially crystallized, such as the RTA 500 °C samples, the switching parameters such as resistance values on both HRS and LRS and operation voltage on both SET and RESET, becomes significantly dispersed. This may be attributed to random crystallization on the grain size induced at the critical temperature. Furthermore, the annealed samples exhibit more random grain size than that of as-grown one, which further confirms the crystallization of the HfO_x film. When samples were annealed at 600 °C, no RS behavior but only large leakage current was observed. Therefore, we conclude that how to improve the resistance to temperature effect of HfO_x films for the application of RRAM device is the ongoing project.

Fig. 3-22 shows the maximum current during the RESET process ($I_{reset(max)}$). From the previous reports, the switching mechanism of RESET process was related to Joule heating to induce the conducting filaments rupture during RESET process, and the highest temperature may occur at the $I_{reset(max)}$. Although the $I_{reset(max)}$ was sometimes a little higher than CC (CC is set at 0.5 mA in this case), a large variation was observed on the annealed samples while the as-grown one did not. We clearly observed that there was a highly correlation between the HRS resistance, SET voltage and $I_{reset(max)}$. The larger $I_{reset(max)}$ may cause higher Joule heating to the filaments, thus over rupture of the conducting filaments. This results in higher SET voltage was needed to form the conducting filaments during the SET process, which causes the poor RS characteristics. Similar results were also proposed by Seo et al. on NiO films. We believe that this was attributed to the alternation on the microstructure of HfO_x films, which was induced from the temperature effect. Further experiment is under progress in order to establish the relation between the degree of nonstoichiometric of

HfO_x and the corresponding operating voltages. Summary of the measured data under Ar RTA treatment is shown in Table. 2.

(b) Under O_2 ambient

The resistance value of the as-grown HfO_x film was in the initial resistance state (IRS). Before the RS operation, forming process was needed for these samples by applying a larger voltage (forming voltage). The purpose of forming process was to initiate the switching properties of HfO_x/TiN RRAM devices, and then the state could be switched from IRS to low resistance state (LRS). At LRS, current level can be higher than compliance current (CC) and then the film was switched to an HRS. The operation from high resistance state (HRS) to LRS and from LRS to HRS is denoted as SET and RESET process. CC was always needed for the HfO_x films during the SET process to avoid completely breakdown of the HfO_x films. Fig. 3-23 compares the typical I-V characteristics of as-grown, RTA at 400 °C in O_2 ambient for 30 (RA400-30), 60 (RA400-60) and 90 (RA400-90) seconds at 0.5 mA CC. The SET and RESET voltage values are clearly observed to increase gradually with the treatment time increasing.

To further find out the treatment effect to the memory reliability, we measured the RS characteristics by an automatic continuous measurement system up to 100 switching cycles. Fig. 3-24 shows the resistance values of as-grown, RTA for 30, 60, and 90 seconds in O_2 ambient on the HfO_x/TiN structure in both HRS and LRS versus the number of switching cycles at 0.1 V reading voltage. With the annealing temperature increases, both the resistance values of HRS and LRS of all the samples increase. This indicates that RTA treatment in O_2 ambient is beneficial for reducing conducting current and operation power, which serves as a good process technology for RRAM application. Once the treatment condition is well controlled, such as about

30 seconds in this case, it can contribute on stabilizing the RS characteristics as well as the switching parameters. A high to low resistance ratio spread from 50 to 400 is observed on as-grown sample, but is greatly reduced down to about 100-200 on RA400-30 sample. However, the dispersed RS properties occur among the 100 switching cycles when the treatment time up to 60 seconds. The LRS resistance becomes severe fluctuation at RA400-60 sample, which causes a severe dispersion on resistance ratio. Several times of switching-failure are observed on the RA400-60 samples, especially on the RA400-90 samples, causing a severe dispersion of the RS switching parameters. Fig. 3-25 shows the collective operating voltage of as-grown, RA400-30, and RA400-90 samples among the 100 switching cycles. The switching values of SET and RESET voltage of HRS and LRS state is 1.04~2.4 V and 0.24~0.8 V for as-grown sample, 1.04~1.28 V and 0.48~0.64 V for RT400-30 one, and 1.52~3.6 and 0.72~2.32 for RT400-90 one, respectively. The operation voltage dispersion on as-grown sample was improved when samples treated at 400 °C for 30 seconds, while further treatment time of about 90 seconds degrades the RS properties. We suggest that the film's microstructure was gradually altered under the oxygen ambient treatment during RTA. This reflects on distinction of the RS properties among these samples.

From the literature, the formation and rupture of the conducting filamentary paths are well explained the switching mechanism of the HfO_x films owing to the abrupt decrease on the conducting current. In addition, Kim et al. [8] have claimed that the rupture of the filament paths occurs at the anodic oxide films only about 3-10 nm. That is to say, the thin oxide layer near anode electrode can significantly dominate the RS properties, as well as stable RS, switching parameters dispersion, endurance cycles, and retention time. From our previous reports, we have provided that the improvement of switching characteristics and resistance dispersion is related

to the oxygen-rich HfO_2 layer formed at the M/O interface caused by UV light [25,26]. A newly formed HfO_2 layer can modify the electrical properties during switching because the switching characteristics of unipolar operation have been reported to be dominated within several nanometers of the thickness of the oxide layer near the anode. Therefore, we suggest that the improvement on the RTA400-30 samples in this study were attributed to the similar results. Fig. 3-26 shows the depth profiles of the hafnium and oxygen elements individually in the RTA400-90 sample. In Fig. 3-26, the oxygen contents in the HfO_x thin film decreases as increasing the annealing temperature, which causes an increase of oxygen concentration in the top electrode by means of oxygen diffusion. This confirms the oxygen-rich layer formed at the interface after RTA treatment. The oxygen-related defects could play an important role during switching on the physical and chemical changes which are intrinsically correlated to the electronic properties of the HfO_x film with high mobility of oxygen vacancies. When samples are treated under oxygen ambient at high temperature, the oxygen atoms would oxidize with the HfO_x interface to form a HfO_2 thin layer above the as-grown sample, which can confine the formation of the conducting filaments at some weak points and effectively stabilize the random oxygen ions' migration during RS. However, the treatment time have to be well controlled because longer annealing time will cause the inter-diffusion at the HfO_x/TiN interface, as shown in Fig. 3-26. Once inter-diffusion occurs, the composition of the HfO_x film would be varied, which leads to random distribution on the film's microstructure and degrades the RS characteristics. Furthermore, under a longer time annealing treatment, the oxygen ions will continuously migrate into the bulk of the HfO_x film along the grain boundaries, which causes a thick fully oxidized HfO_2 film. The V_{set} and V_{reset} values were observed to increase with the treatment time increasing, which represents that a thicker oxide layer was formed and a larger operation voltage was needed to drive the

RS behavior. A great increase on the LRS resistance values implies that the conducting filamentary paths become hard to be formed during SET process. Eventually, the MIM structure will lose the RS behaviors.

As a non-volatile memory (NVM), not only the stable RS characteristic but also the low power consumption is important to sustain a long time usage. Therefore, we further discuss the issue about operation power. Because the current level of RESET operation is about 2 orders of magnitude larger than that of SET operation, we may assume that the main power is mainly from the RESET process. Fig. 3-27 shows the maximum reset current ($I_{reset(max)}$) during RESET process of as-grown. The $I_{reset(max)}$ current demonstrates a little larger than the CC is sometimes observed on the unipolar RS, which is the largest current of a RS operation. From Fig. 3-27, the $I_{reset(max)}$ is clearly reduced after samples were treated by RTA for a period of time. Fig. 3-28 shows the operation power of as-grown, RTA400-30, and RTA400-90 samples tracing 100 switching cycles. The average power is about 0.415 mW for as-grown, 0.247 mW for RTA400-30, and 0.55 mW for RTA400-90 samples. Only the RTA400-30 sample exhibits the benefit of reducing operation power. Although the $I_{reset(max)}$ is slightly reduced compared to the as-grown sample, however, the operation voltage is greatly increased, which causes an totally increase on the operation power. Furthermore, because of the random distribution of the operation voltage and reset current, the needed RESET power of RTA400-90 samples are much dispersed than the other one. The best treatment condition is the RTA400-30 sample. The random distribution on the switching parameters such as operation voltage, RESET resistance values, and operation power, may be highly correlated to the fluctuant distribution of the film's composition and microstructure of RTA400-90 sample, as shown in Fig. 3-26. Summary of the measured data under Ar RTA treatment is shown in Table. 3.

3.3.5 Process effect

Using different resistance states as data storage, resistive random access memory (RRAM) has advantages of simple structure, low power consumption, fast switching speed, and easy integration with CMOS process. These merits make it a promising new solution for non-volatile memory [27,28]. Unipolar resistive switching (RS) has been extensively investigated owing to its many advantages in device operation [8,29,30], and a model has been proposed based on local conducting filaments. The unipolar RS features can be well explained in terms of the formation and rupture of conducting filaments [10]. More recently, the material properties of the electrode/oxide (E/O) interface have had a significant impact on the unipolar RS characteristics [7,31], and Kim et al. report that the formation and rupture of conducting filaments mainly occur near the E/O interface. More precisely, they claimed that the properties of TiO_2 around 3-10 nm from the anode electrode determine switching stability. Several factors have been reported to influence this thin layer near the anodic side, including external factors related to the transition metal oxide (TMO), such as the forming process [32], current compliance [33], electrode material [11,15], operating type [34] as well as the internal factors of TMO, such as the deposition process and condition [35], crystallinity [36], and treatment conditions of the TMO material [25,37]. However, less discussion has been devoted to the impact of sputter damage during sputtering deposition on RRAM electrical characteristics. Sputtering damage generates traps and interface states near the HfO_x film surface and causes oxide quality and reliability to deteriorate [38,39]. Several kinds of plasma damage may occur during the sputtering process such as (a) charges bombarding the binary metal oxide film, (b) ultraviolet (UV) light formation of e-h pairs, and (c) high energy particle bombardment damaging the film property. Therefore, if this thin layer

can be carefully managed, the RRAM device will acquire a good On/Off ratio which strongly relates to better percolation of conducting elements and reduced variation of V_{on} and V_{off} which depend on repeatability of the formation and rupture process during each consecutive switching.

This section investigates the effects of Pt top electrode deposition on HfO_x/TiN film. Two main types of metal deposition processes (i.e. e-beam evaporation and dc sputtering) were used to investigate the electrical characteristics of RRAM devices. Additionally, a stacked Pt electrode was tested by depositing an evaporated Pt layer prior to sputtering. The effect of the thickness of this evaporated Pt layer on the electrical characteristics is discussed through voltage-mode (VM) and current-mode (CM) measurement. The electrical characteristics of RS properties show high dependence on the fabrication process of the top electrode, and that the electrode fabrication process is a key factor in causing fluctuation in the switching parameters.

(a) Film characteristics:

Fig. 3-29(a) shows XPS analysis of the chemical properties of HfO_x gate stacks. The Hf 4f (7/2) peak is 17.5 eV, separated by 1.5 eV from the Hf 4f (5/2) peak at 19.0 eV. A shoulder begins to appear at a lower binding energy of 15.4 eV. These low binding energy components may be attributable to the Hf metal, suggesting that the HfO_x films are nonstoichiometric with metallic components due to insufficient oxidation of the Hf metal layer ($x < 2$). Fig. 3-29(b) shows typical XRD spectra of HfO_x films. Peak positions, taken from monoclinic-HfO_2 show polymorphism, are compatible with poly-crystalline non-stoichiometric hafnia. The polycrystalline structure can provide grain boundaries, oxygen vacancies, and defects for easy electron migration. This results in a much smaller breakdown electric field (i.e. 2.8 MV/cm) than what had been previously reported in the literature [40]. Only bias

voltage of 5.6 V is needed to fulfill the soft breakdown forming process.

(b) Operation mode:

The state switches from high resistance state (HRS) to low resistance state (LRS) and vice-versa is referred to as SET and RESET processes, and the voltage values when SET or RESET occur are called V_{set} or V_{reset}. Resistance values of LRS and HRS are named R_{on} and R_{off}. Fig. 3-30 shows typical I-V curves of Pt (E)/HfO_x/TiN samples respectively using the (a) VM operation for SET and RESET process, and (b) CM operation for SET and VM for RESET process. A forming process was needed in the beginning to activate the reversible RS phenomenon at a current compliance of 0.5 mA under both a VM and CM sweep. Following the forming process, the state was switched to LRS. As the applied voltage increases to a certain value around 2.5 V, an abrupt decrease of conducting current occurs and stable R_{off} is attained, as shown in Fig. 3-30(a). The resistive transition from HRS to LRS is triggered by increasing the voltage value up to 5 V again. This completes one RS cycle. V_{set} under CM is almost the same with VM shown in Fig. 3-30(b). A sudden jump of the measured voltage also occurs at 5 V under CM operation. Furthermore, resistance values under a continuous VM-controlled measurement are identical to the formation of stable R_{on} and R_{off} values, which may be attributed to the polycrystallinity of HfO_x films. No intermediate states or anomalous RS are observed on the Pt (E)/HfO_x/TiN sample shown in Fig. 3-30(b), and this can be explained by the fact that the filamentary conducting paths develop near stability and with no additional percolation paths produced at the current stress [9]. Even when current compliance value is set at 50 μA, no intermediate state is observed as shown in Fig. 3-30(c). This indicates that stable R_{on} values are available regardless of the current compliance value. The observed phenomenon gives important indications that film crystallinity is a key factor in

stabilizing R_{on} and R_{off} values.

(c) Fabrication process:

The impact of the top electrode fabrication process on the electrical characteristics of HfO_x RRAM devices was then investigated by different electrode fabrication processes. Typical I-V curves of Pt (S), Pt (E50+S), and Pt (E150+S) using the VM operation for the SET and RESET processes are shown in Fig. 3-31(a) ~ 3-31(c), respectively. During the RS, all samples are set at the same current compliance of 50 μA. The typical RS characteristic of wide dispersion at the HRS is observed on the Pt (S) sample as shown in Fig. 3-31(a). The large dispersion of R_{off} values is quite different from that of the Pt (E) sample, which highlights the importance of the fabrication process of the top electrode on the switching behaviors of RRAM devices. For the Pt (E50+S) sample, the inserted 50 Å evaporated layer slightly reduces the fluctuation of R_{off} resistance values, as shown in Fig. 3-31(b). Increasing the thickness of the inserted layer, considerably reduced the fluctuation of R_{off} values, as shown in Fig. 3-31 (c), with nearly identical results for R_{on}. In Fig. 3-32, the switching parameters from Fig. 3-31 are indicated as a cumulative percentage distribution of R_{on} and R_{off} values read at 0.4 V, for the three samples. Large dispersions (about five orders of resistance value from 10^6 to 10^{11} Ω) on R_{off} of the Pt (S) sample were observed, which was reduced by 3 orders of magnitude on the Pt (E150+S) sample.

(d) Sputter damage:

During a sputtering process, the plasma is complex and highly dependent on all the preparation parameters, including the partial pressure of Ar and H_2 [41], substrate heater temperature [42], and even the sputtering power level [43]. The evaporated

particles are determined by the e-beam irradiated source temperature (kTv), for which the energy is about 0.1 eV [44]. The evaporated particles are less energetic than that sputtered ones when the particles reach the growing film. Thus, the underneath layer is less effected. Generally, sputtered particles have kinetic energy of several eV (about 1-3 eV) which is up to one order of magnitude greater than that of the evaporated particles. Therefore, we suggest that the sputtered particles are more energetic and aggressive to the growing film. For a better understanding of the sputtering mechanism, we describe the sputter deposition process. Schematic illustrations of the generation and the primary collision process of the high-energy particles in the sputter-deposited films are presented in Fig. 3-33. In the dc sputtering system, an inert gas Ar plasma is initiated and maintained between a target and a substrate. A sheath voltage is set up near the target. Inert gas ions created in the plasma are accelerated across the sheath, striking the target surface at a near-normal-incident angle. These ions can have energies between 100 and 1000 eV. Their impact with the target results in the sputtering of metal atoms from the target. In addition, Ar^{o} is sometimes produced by the Auger neutralization and recoil of energetic incident Ar ions [45]. Negative oxygen ions (O^{-}) are given less consideration because the target surface was pre-sputtered for a period of time. These sputtered atoms are then transported toward the substrate. Before reaching the substrate, any sputtered species have to mediate through the plasma. These sputtered species will collide with the Ar atoms or ions and dissipate their kinetic energy, resulting in the scattering of unwilling deposited atoms such as Ar atoms or Ar^{+} to bombard the growing film's surface. In this study, a pressure of 7 mtorr was used and the calculated mean-free path of about 1-2 cm is significantly shorter than the 13 cm substrate-to-target distance in the sputtering system. Therefore, upon leaving the target, the kinetic energy of sputtered particles is mostly transferred to the plasma by collisions. Although the voltage drop was applied

across the anode sheath to determine the kinetic energy, the degree of damage caused to the growing film by the ionized species extracted from the plasma was determined by the plasma-substrate voltage drop. For a dc gas discharge, the correlation between the plasma-substrate voltage drop and dc sputtering power density is proposed as follows [46]

$$V_p - V_{sub} = a + b\ln W \quad (3\text{-}3)$$

Where V_p and V_{sub} are the voltages of the plasma and substrate, respectively, W is the power density, and a and b are the parameters related to ion impingement rate and electron temperature, respectively. When sputtering deposition was conducted under high sputtering power, a larger voltage drop is present across the plasma and substrate, resulting in more ionized species to bombard the growing surface, thus causing more damage to the growing surface and possibly increasing the surface roughness of the HfO_x films. This results in modifications to the film's microstructure such as shallow bulk atomic rearrangement, resputtering of surface adatoms and weakly bonded near-surface species during deposition [47]. We assume that most of the bombardment is attributed to the ionized species Ar^+ because only the Ar^+ will be dependent to the plasma-substrate voltage drop. Some of the energetic Pt or hyperthermal neutral atoms (Ar^o) would also be kicked onto the growing surface to bombard the surface's atoms. However, these neutral atoms may not be the main reason for the bombardment because they will not have been accelerated by the plasma-substrate voltage drop. Experimental studies in the literature have shown that hyperthermal adatoms (Ar^o) with incident energies of 20 eV or above can be reflected and/or induce resputtering depending on the incident angle [47]. The kinetic energy of hyperthermal adatoms is first dissipated by the plasma, then kicked onto the growing surface with a random distribution of incident angles, resulting in increasing the surface roughness. Therefore, it is suggested that the Ar^+ is the main cause of the damage or

bombardment on the growing surface. In addition, Moon et al. have reported that the sputter damage due to Ar^+ ion bombardment on metal surfaces is extremely low and that metal atoms in the ion impact zone recrystallize almost completely, in contrast to how they behave on semiconductor surfaces [48]. (The defect generation rate on the Pt surface is extremely low compared to that on Si, where the Si surface becomes completely amorphous.) Therefore, having an evaporated thin layer prior to sputtering helps reduce the impact of the bombardment induced by the sputtered particles.

Many studies have demonstrated that the unipolar switching characteristics of RRAM devices are significantly related to the electrode/oxide interface [49,50]. More recently, a different electrode has been found to cause a change in the lower layer's stoichiometric material properties or oxygen concentration. From this series of discussions, we suggest that ionized species (Ar^+) during deposition changes the properties of the interface stoichiometric material. This interface material modification is reflected on the V_{set}, V_{reset}, and R_{off} dispersion. The results from the report by Kinoshita's et al. [6] not only agree with the assumption that the RS between the two states occurs on the anodic side of the insulator film, but also provide a clue that the HRS data is easily lost due to exposure to the sputtered particles. They claim that the Ni-O bonding can be influenced by sputtered damage and result in data loss. Therefore, we suggest that the insertion of Pt thin film by e-beam evaporation, such as in the Pt (E50+S) and Pt (E150+S) samples, can contribute to release the Ar^+ ion bombardment during sputtering deposition, which results in more reliable RS characteristics, as shown in Figs. 3-31 and 3-32. We not only confirm that the sputtered damage has a great impact with respect to the switching properties, but we also demonstrate a way to reduce this damage by depositing a thin layer before sputtering or by using low sputtering power deposition.

(e) Switching parameters:

CM operations can reveal information unobservable in VM operation [9], and was used to learn more about the sputtered damage impact on R_{on} values during the SET process. Fig. 3-34(a) ~ 3-34(c) respectively shows the SET I-V curves of the Pt (S), Pt (E50+S), and Pt (E150+S) samples using CM operation. The intermediate resistance states and anomalous switching randomly occurred in different switching cycles on the three samples. Severe fluctuations of V_{set} and R_{on} (indicated by arrows) values are observed on the Pt (S) sample shown in Fig. 3-34(a). Although the abrupt switch from the R_{off} to the R_{on} state occurs at a trigger point, a zigzag phenomenon during the voltage switch was clearly observed. When the thickness of the inserted Pt electrode increases, the fluctuations of the R_{on} value decrease, as indicated by arrows in Figs. 3-34(b) ~ 3-34(c). That the fluctuation levels of the R_{on} values decreased with the increasing thickness of the inserted Pt layer is consistent with the decrease in fluctuation of the R_{off} value under VM operation shown in Figs. 3-31(a) ~ 3-31(c). Compared to the evaporated sample, the CM operation shown in Fig. 3-30(c) exhibits no zigzag phenomenon. The zigzag phenomenon of the measured voltage corresponds to the instability of the conducting current during the SET process. Filamentary conducting paths are generated in a random distribution, without any preference. The Pt (S) sample exhibits no RS properties at sputtering power levels higher than 200 W, which reveals the process condition is a critical factor in the RS phenomenon. Table 3-4 shows the collective switching parameters of the Pt/HfO_x/TiN samples under different top electrode fabrication processes. The dispersion of switching parameters on the V_{set}, V_{reset}, R_{on}, and R_{off} decreases as the thickness of the evaporated Pt thin layer increases. In our experiment, in addition to showing that the oxide layer near the anode plays an important role in the switching process, we also demonstrate that the effect of plasma has some significant impact on the electrical properties. Because the

plasma process is a common element in semiconductor technology, it is very crucial to isolate the stability of RRAM component systems from the effects of the plasma process. Further investigation is needed to explain in detailed the possible mechanism for energetic damage during sputtering deposition.

3.3.6 UV light exposure

In recent years, extensive research on resistive random access memory (RRAM) has been conducted on the basis of two different resistances of oxide materials. Due to its high potential advantages, such as small cell size, fast switching, low power consumption, and easy compatibility with the CMOS process [1], RRAM has become one of the best candidates for application in next generation non-volatile memory devices. In recent research, several factors have been reported to influence the switching properties of RRAM strongly, such as operating type [51], current compliance [33], forming process [32], electrode materials [11,15], and treatment condition [52]. However, based on the proposed factors, the switching mechanism for a RRAM device remains to be under debate. It is thus necessary to investigate other factors in order to determine a more reliable switching operation for a RRAM device.

The fully transparent RRAM (T-RRAM) device was achieved by Seo et al. using highly transparent ITO film as electrodes and high band-gap material ZnO as insulator film [53]. A completely see-through MIM capacitor structure with more than 85% transmittance for the visible light region can be obtained. However, for a fully transparent device, whether or not ultraviolet (UV) light influences the electrical characteristic of the electrode and insulator film is a critical issue. ITO thin film has been extensively studied in optoelectronic devices [54,55] because of its unique transparency and conducting properties. For a highly degenerated n-type semiconductor ITO film, electrical conductivity was reported to be easily affected by

UV-light [56,57] and ozone oxidation [56]. Meanwhile, UV laser impact on the oxide film greatly depends on the laser fluence and pulse duration of the laser beam, as well as the structural and compositional properties of oxide quality [58]. Although the laser-induced damage threshold (LIDT) value may be improved by laser pulse on some oxide materials [59], the problem of laser damage of thin oxide films, however, has not yet been solved [60]. Some groups have attempted to elucidate the origin of laser damage in oxide films using methods such as the pulse photothermal technique [61,62] and intrinsic absorption [63] among various others. Once the characteristic of the ITO or oxide film has been influenced by the UV laser, then the electrical properties will be altered simultaneously.

In this section, laser effect on the electrical properties of an ITO/HfO_x/TiN capacitor structure has been performed. Different exposure times of the UV laser were investigated to explore the corresponding switching properties. Electrical properties such as stability, endurance, and sheet resistance regarding UV irradiation were likewise widely explored.

In the beginning, some abbreviations on structure and treatment condition were made. The ITO/HfO_x/TiN capacitor structure is abbreviated as IHT, UV light exposure on HfO_x/TiN device before and after ITO deposition are denoted as #1 and #2, respectively, and exposure time is shown with various specifications, such as #1-120s or #2-30s. Fig. 3-35(a) shows the transmittance degree of the as-grown ITO material. With the 300-900 nm light wavelength, it irradiates from the ITO side and is received by the glass side. For the visible 400-800 nm region, the ITO material has an average of up to 85.28% degree of transmittance. Electrical characteristics of the forming process of different UV light exposures are shown in Fig. 3-35(b). The #1-samples exhibit much larger leakage current than the #2-samples during the forming process, indicating that the oxide quality of the #1-sample was considerably

deteriorated under direct UV light exposure. With even just 30 seconds of direct UV light exposure on the HfO_x surface - #1-30s sample, a leakage current larger than that of the #2-120s sample was induced. According to Druijf's report, several kinds of defects may be generated inside the bulk of the HfO_x film after UV light exposure [64]. The generated defects can enhance oxygen ion migration easily along the grain boundaries and result in increasing leakage current on the #1-samples. Meanwhile, a much lower leakage current was observed on the #2-samples, which was caused by other factors. More detailed mechanisms will be discussed later.

Basically, Fig. 3-35 presents the pristine leakage current of the #1- and #2-samples of the MIM structure under various times of UV light exposure. After a certain voltage was applied to result in a soft breakdown, the device will show RRAM characteristics. Fig. 3-36(a) and 3-36(b) compares the electrical characteristics of the ITO/HfO_x/ITO capacitor structure of the untreated and #2-120s samples, respectively. Under an automatic continuous dc voltage sweep measurement system, more than 100 switching cycles of set/reset test were demonstrated on the two samples. In Fig. 3-36(a), the unstable electrical characteristic of the untreated samples with large dispersion on the operation voltage and high resistance state (HRS) resistance values during the SET and RESET process was clearly observed. Interestingly, the switching stability will be significantly increased once the samples were placed under UV light. The #2-120s samples exhibit not only excellent stability and reproducibility of switching behaviors, but also less HRS resistance and voltage dispersion among 100 switching cycles operation as shown in Fig. 3-36(b). Many studies have demonstrated that different electrode metals have a strong impact on the set voltage (V_{set}) and reset voltage (V_{reset}) of RRAM characteristics [49,50]. More recently, a different electrode has been found to cause a change in the underneath layer's stoichiometric material properties or oxygen concentration. We hypothesize that UV exposure changes

interface stoichiometric material properties. This interface material modification reflects on V_{set}, V_{reset}, and HRS dispersion improvement on the #2-samples. The endurance characteristics were traced among the 100 switching cycles to clarify the resistance dispersion. The resistance values with the switching cycles of the untreated and #2-120s sample are shown in Fig. 3-37(a) and 3-37(b), respectively. In Fig. 3-37(a), the "reset failure" phenomenon, which is a failure in switching from R_{on} to R_{off} state at the application of V_{reset}, was observed at times on the untreated sample. This phenomenon is caused by a readout mistake owing to the random fluctuation of the V_{set} and V_{reset} values. On the contrary, an extremely confined distribution of the resistance values and no reset failure are observed on the #2-120s samples as shown in Fig. 3-37(b). The untreated sample with 1 order of magnitude on the HRS resistance dispersion was obviously reduced to within 1 order of magnitude of resistance fluctuation on the #2-120 samples. UV light with various exposure times from 30 to 600 seconds on switching properties is also investigated. In Fig. 3-38, the cumulative probability of resistance values during 50 successive resistive switching cycles in untreated, #2-120s, and #2-300s samples is compared. Obviously, the HRS resistance dispersion gradually reduces when the exposure time increases. Furthermore, a slight decrease in both HRS and low resistance state (LRS) resistance values as compared to the untreated sample is observed. However, the poor and short-lived switching characteristics of only 10 switching cycles are observed on the #2-600s samples. Stabilization of the conducting behaviors during the resistive switching of our IHT structure is only achieved by UV light exposure. Therefore, further analysis is required to determine the detailed physics.

The ITO film under UV light exposure is discussed next. The Rs of the ITO film under different exposure times of UV light is measured by a four-point probe. A slightly linear negative dependence between Rs and exposure time is observed on the

#2-samples, which indicates that the atomic compositional ratio of the ITO electrode was gradually affected by a longer UV light exposure. The UV light exposure will easily activate the oxygen ions inside the ITO film to the excited states once the ITO films are under UV light [65]. Due to the lower free energy to oxygen of Hf than In and Sn, the excited oxygen ions are more willing to oxidize with Hf metal and forms an oxygen-rich layer HfO_2 at the M/O interface. This newly formed HfO_2 layer can modify the electrical properties during switching because the switching characteristics of unipolar operation have been reported to be dominated within several nanometers of the thickness of the oxide layer near the anode [8]. Among many proposed models, the filament model may explain the switching properties here. The oxygen-related defects could play an important role during switching on the physical and chemical changes which are significantly correlated to the electronic properties of the HfO_x film with high mobility of oxygen vacancies. At the beginning, the forming process applied a high positive voltage in which, a large number of oxygen ions are extracted towards to the top electrode, and oxygen vacancies are formed. The #2-samples under UV light exposure exhibit distinct electrical characteristics which indicate a strong influence on the oxygen contents and oxygen-related defects in the interface and bulk of the HfO_x films. Druijf et al. reported that several kinds of defects, such as unstable fast donor states, slow donor states, and drifting ions, may be generated in the midgap between the anode and cathode [64]. The defects can facilitate easy migration of the oxygen ions along the grain boundaries and result in a large leakage current on the pristine samples. The generated defects caused by UV light exposure act as fast diffusion paths for oxygen ions migration during the switching cycles. Furthermore, the newly formed oxygen-rich HfO_2 layer at the M/O interface dominates the switching properties, which can confine the formation of the conducting filaments at some weak points and effectively stabilize the random oxygen ions' migration during

resistive switching. Therefore, the less dispersed switching parameters and reliable switching properties can be observed on the #2-samples. We believe that the difference of a newly formed oxygen-rich HfO_2 on different samples caused by UV light exposure may be the key for this improvement in switching properties.

For the #1-samples, there is no obvious improvement on the V_{set}, V_{reset} and HRS resistance dispersion. The clear evidence of the effect of UV light on electrical properties is that the endurance is greatly reduced under a longer UV exposure time. The improvement in HRS resistance dispersion is not observed, but the large leakage current observed, as shown in Fig. 3-35(b), confirms that the ITO electrode has a great influence on dispersion improvement under UV light irradiation. Further analysis is necessary to find out the detailed physics behind this result.

3.3.7 Abnormal resistive switching

The resistive switching (RS) phenomenon has attracted significant attention recently in view of its potential for nonvolatile memory application – resistive random access memory (RRAM). RRAM offers a possibility of high density integration, lower power operation, easier down-scaling and Si semiconductor compatibility [1]. This phenomenon has been demonstrated in different types of inorganic, organic, polymeric materials, and transition metal oxides. In recent research, several factors have been reported to influence the switching properties of RRAM strongly, such as operating type [51], current compliance [33], forming process [32], electrode materials [11,15], and treatment condition [52]. However, based on the proposed factors, the physical origin of the switching mechanism is still a subject of ongoing debate, though it is suggested to be closely related to the formation and rupture of conducting filamentary paths by an applied voltage. It is thus necessary to investigate other factors in order to determine a more reliable switching operation for a RRAM

device.

Using transparent conductive oxides (TCO) as electrodes provide the possibility to broaden the scope to optoelectronics, such as organic light emitting diodes (OLED), transparent thin film transistors (T-TFT), and transparent resistive random access memory (T-RRAM). For these kinds of electronic devices, a high transmittance for the visible light and a good performance for stable reliability are critical issue to be sustained. However, for a highly degenerated n-type semiconductor ITO film, electrical conductivity was reported to be easily affected by ultra-violet (UV) light [56,57] and ozone oxidation [56]. Furthermore, laser-induced damage on oxide films has become more serious with the increase in the high quality demand for a lower leakage current during the past years. UV laser impact on the oxide film greatly depends on laser flux and pulse duration of the laser beam, as well as structural and compositional properties of oxide quality [58]. Because of highly correlation between the electrical properties and oxide quality, once the characteristic of ITO or oxide film has been influenced by UV laser, then the electrical properties will be altered simultaneously.

In this paper, we investigate the effect of laser effect on the electrical properties of a ITO/HfO_x/TiN RRAM device. The UV light exposure on ITO/HfO_x/TiN and HfO_x/TiN structures was both experimented. The electrical characteristics of the ITO/HfOx/TiN devices show highly relationship on the exposure surface. Electrical properties such as I-V curves, endurance, devices yield, and switching mechanism was discussed in this paper. A probable switching mechanism was proposed based on the effect of the UV laser to explain the detail difference between these two device types.

Forming process was needed in the beginning to activate the resistive switching (RS) characteristics for all the devices. A positive voltage sweep from 0 to 5.5 V with

a current compliance triggers the current value to a high level abruptly at the forming voltage (V_{form}), and the state switches from initial resistance state (IRS) to low resistance state (LRS). The U-samples exhibit much larger leakage current than of S-samples during the forming process, indicating that oxide quality of the U-sample was considerably deteriorated under direct UV light exposure. Several kinds of defects may be generated inside the bulk of the HfO_x film after UV light exposure according to Druijf's report [64], which can induce high leakage current on U-samples. Afterwards, a positive voltage swept again from 0 to 4 V causes the abrupt decrease of the conducting current at certain voltage value, which was named reset voltage (V_{reset}). Then, the state was switched from LRS to a high resistance state (HRS). Hereafter, the state could be switched to HRS and LRS repeatedly under positive bias. The state switched from HRS to LRS and from LRS to HRS was defined as SET and RESET process. Fig. 3-39(a) and (b) shows the unipolar I-V characteristics of ITO/HfO_x/TiN devices that exposes under UV light for 120 s, the S- and the U-samples, respectively. The electrical properties of the S-samples show a typical I-V curve. Oppositely, the random occurrence of the abnormal resistance switching (ARS) behavior, where the current suddenly jumps to high current level at the end of the RESET process, is observed on the U-samples (indicated by arrows). The type of ARS was often observed on U-Samples (about 70%), but is less on the S-ones. The U-samples using Pt as top electrode also demonstrating the ARS behavior shown in the inset of Fig. 3-39(b), which confirms the influence of UV. We suggest that the distinction between the two types of the I-V curves was dominated by different switching mechanism, which was attributed to the effects of the UV light exposure.

To evaluate the reliability of the ITO/HfO_x/TiN devices under UV light irradiation, endurance test was investigated. Resistance values with the switching

cycles of S- and U-samples under UV light exposure for 120 s are presented in Fig. 3-40. The resistance values were both read out at 0.1 V in each dc sweep. Although the resistance values of both HRS and LRS show some fluctuations, the on/off ratios are about 7 without any obvious degradation within 100 cycles for S-samples, while on/off ratios with severe overlap within 30 cycles for U-samples. The distribution of the V_{set} and V_{reset} values versus switching cycles is shown in Fig. 3-41(a) and 3-41(b) for the S- and U-samples, respectively. V_{set} and V_{reset} are the two critical switching parameters to determine when the state is switched to another state, and the fluctuation on V_{set} and V_{reset} values has been considered to be an arduous issue to be ameliorated. V_{set} and V_{reset} distributes in a range of 4.2 to 5.8 V and 2.6 to 3.7 V on the S-samples (average V_{set} and V_{reset} is about 4.8 and 3.4), and in a range of 3.3 to 6.4 V and 2.3 to 4.0 V on the U-samples (average V_{set} and V_{reset} is about 4.6 and 3.1), respectively. As it can be clearly seen that the programming voltages of the U-samples are a little lower than that of S-samples under the same time of UV light exposure. In addition, the dispersion of V_{set} and V_{reset} on the U-samples are worse than that of S-ones. Some factors have been reported to have a strong impact on the V_{set} and V_{reset} dispersion, such as electrode material [49], implanting dopants [66], interfacial defects [67], fabrication process [68], inserting an additional layer above the oxide film [69], etc. Because the same electrode materials and deposition process were adopted on all our samples, we suggest that the different electrical characteristics between the two types of samples may be attributed to the effect of UV light exposure. Since Druijf had claimed that some oxygen-related defects may be generated or induced inside the HfO_x film under UV light exposure, a large amount of defects are existed inside the U-samples [64]. Furthermore, Choi et al. reported a $Au/NiO/SiO_2/p^+$-Si RRAM device with less V_{set}, V_{reset}, and less fluctuation in SET process with increasing SiO_2 thickness (from 50 to 300 nm) due to reduction of

localized state density inside thicker SiO_2 layer [67]. Therefore, we rationally suspect that the oxygen-related defects preexisted inside HfO_x film under UV light irradiation can be corresponding for the fluctuation degree of V_{set} and V_{reset}.

Among the many proposed models, the formation and rupture of the conducting filaments based on Joule heating effect inside the HfO_x matrix may explain the switching mechanism observed in this study, due to abrupt switching of the conducing current from LRS to HRS [17,40]. Oxygen-related defects could play an important role on physical and chemical changes during switching, which is significantly correlated to the electronic properties of the HfO_x film. Liu et al. utilized random circuit breaker (RCB) network to elucidate the observed random ARS behaviors on Pt/NiO/Pt structure, and well simulated the possible change on the microstructure during the RESET process [70]. According to their reports, we hypothesize that the shapes of the conducting filaments between S- and U-samples are different after forming process. The schematic diagram is shown in Fig. 3-42(a) ~ 3-42(d) for S- and U-samples to demonstrate the switching mechanism in each step. Fig 3-42(a) and 3-42(c) represents the structure of S- and U-samples after UV light exposure. The HfO_x interface of U-samples is homogeneous damaged by direct UV light exposure and induced lots of defects on it (shown in Fig. 3-42(c)) [64], providing an isotropic formation of conducting channels during forming process (shown in Fig. 3-42(d)); while the S-samples, only about 50% intensity of the UV light at wavelength of 365 nm (not shown here) on the HfO_x film does not large enough to cause severe damage to the oxide quality. Moreover, once the ITO films are under UV light, the UV light exposure will easily activate the oxygen ions inside the ITO film to the excited states [65]. Because of Hf metal has lower free energy to oxygen than In and Sn, the excited oxygen ions are more willing to oxidize with Hf metal and forms an oxygen-rich thin layer HfO_2 at the M/O interface, as shown in Fig. 3-42(a). Therefore, an anisotropic

formation of conducting filaments during forming process makes the filaments more confined near the ITO/HfO_x interface on S-samples, as illustrated in Fig 3-42(b). The filament types on U-samples easily cause formation and rupture at the same time during RESET process and lead to larger variation [70]. This different UV light exposure sequence causes a structural distinction at the HfO_x film interface between the U- and S-samples, which reflects a variance on leakage current, I-V curves, and fluctuation of V_{set} and V_{reset} values. The TE ITO with higher oxygen contents (oxygen partial pressure is about 33% during ITO deposition) was also experimented for verification. No ARS phenomenon and less voltage dispersion was observed on the oxygen-rich ITO samples. The results are similar to the reports that an additional oxide layer formed at the interface is efficient to suppress the fluctuation of V_{set} and V_{reset} [40]. It needs intensive investigation to explain the detailed physics of UV laser for reliable RRAM characteristics.

3.4 Bipolar resistive switching properties of HfO_x thin films

In the as-deposited HfO_x films, resistance switching (RS) behavior cannot be found before forming process. A large voltage value applied on the top electrode can lead to the conducting paths formed clusters of point defects, similar to soft breakdown. The forming process is needed for all the samples to activate the RS characteristics with a current compliance (CC) setting. The CC is used to protect devices from hard breakdown. First of all, we operate the samples by switching to LRS by negative bias and back to high resistance state (HRS) by positive one (clockwise - CW). After the forming process, the HfO_x/TiN device reaches its low resistance state (LRS). Fig. 3-43 shows the bipolar I-V curves of the Pd/HfO_x/TiN (PH) and Pd/Al/HfO_x/TiN (PA) samples. Both PH and PA samples can be operated to LRS by negative bias and back to HRS by positive one (clockwise - CW). The PH

sample exhibits a large high to low resistance ratio of 60 at 0.2 V, while the PA one of only 7 is observed. In addition, the opposite sweep loop (counter-clockwise - CCW) was also performed on PH and PA samples to study the switching mechanism. Only PA samples exhibit the CCW RS loop. It means that the PH samples demonstrate the polarity-dependent RS characteristics while PA samples show the polarity-independent RS, which can be rationally suggested that the distinct difference on the RS properties may be caused by this inserted Al thin layer. The coexistence of CW and CCW RS curves of PA sample are shown in Fig. 3-44. The switching properties obviously depend on the operation polarity, with a larger operating current and smaller operating voltage observed on CW RS loop. Asymmetry between CW and CCW RS curves may be attributed to the structural asymmetry.

TiN has been reported to serve as a good oxygen reservoir and can control and modulate the distributions of migrated oxygen ions and oxygen vacancies inside insulative matrix [71]. As it was reported that TiN/ZnO/Pt [72] and Pt/TiO_2/TiN [73] memory devices exhibited high resistive switching performance, the TiN electrode possesses the specific properties to absorb and extract oxygen ions reproductively, resulting in the RS characteristics on both PH and PA samples. However, once the reactive metal Al was inserted at the Pd/HfO_x interface, the polarity-dependent RS will change to polarity-independent RS, as observed on PA samples shown in Fig. 3-44. As we known, the RS properties were highly correlated to the electrode/oxide interface reported by many groups [74]. More recently, a reactive metal inserted at the electrode/oxide interface has been proposed to modulate the RS characteristics. Hasan et al. [75] observed that the RS loop was changed from CCW to CW loop after inserting a thin samarium (Sm) metal layer at the Mo/LCMO interface. Furthermore, an oxide (SmO_x) layer consequently forms due to the reaction between the reactive Sm and O^{2-}. Formation and deformation of the SmO_x layer at the interface during the

applied positive and negative bias voltage dominate the resistance values to high or low resistance state. Lin et al. [76] modified the resistive switching behavior of ZrO_2 memory films by using Ti top electrode. They claimed that a series resistance between Ti and ZrO_2 film will be formed, composed of a TiO_x layer and a ZrO_y layer, causing the RS characteristics from unipolar RS to bipolar RS behaviors. In this study, we suggested that the inserted Al thin layer played a similar role as reported above. A metal oxide layer AlO_y will be formed at the interface to modulate the oxygen migration under applied bias. To further confirm the interface reaction and diffusion between the electrode and the HfO_x film, XPS and Auger depth profile were obtained as shown in Fig. 3-45. From Fig. 3-45(a), the XPS spectrum obtained from Pd layer, it was confirmed that there was no oxidation in the film, while formed a metal oxide layer composed of AlO_y and HfO_z at the Al/HfO_x interface as shown in Fig. 3-45(c). Fig. 3-45(b) obtained from AES depth profile of the device structure, diffusion/oxidation at the interface was not observed when Pd was used as a top electrode. Also it can be confirmed that HfO_x layer is well contained between the top and bottom electrodes. On the other hand, reaction and interdiffusion at the M/O interface were observed when Al thin layer was used as top electrode. We believe the difference on the film's structure will be responsible for the polarity-dependent or -independent RS characteristics. The thin AlO_y layer formed at the M/O interface can modulate the oxygen ions and vacancies distribution at the near anode oxide, even under the applied voltage. Reactive metal Al will easily oxidize with the oxygen ions under applied positive bias, which confines the oxygen contents at the interface. Therefore, the oxygen contents can be maintained at the interface like the role of oxygen reservoir TiN, although there might be some detailed difference between them. So, the RS behavior will change from polarity-dependent to polarity-independent when Al thin layer was inserted at the interface.

Based on the proposed switching mechanism, migration of oxygen ions during switching may be the possible switching mechanism on HfO_x/TiN devices for CW and CCW RS loop. For CW RS, The TiN electrode was an effective oxygen reservoir. During the set process, soft breakdown happened and nonlattice oxygen ions and oxygen vacancies were generated at the same time. The new generated oxygen ions are absorbed and reserved by the TiN electrode while oxygen vacancy conducting filamentary paths formed in the HfO_x thin films. On the contrary, during the reset process, the applied negative electrical field extracted oxygen ions from TiN bottom electrode into HfO_x thin films to recover the oxygen vacancies near the interface region, resulting in the rupture of the oxygen vacancy conducting filamentary paths. Therefore, both the PH and PA can be performed the CW RS loop. For CCW RS, when Al thin layer was inserted at the Pd/HfO_x interface, a AlO_y metal oxide will be formed near the interface. The reactive AlO_y layer plays a similar role like TiN electrode, which can absorb oxygen ions inside AlO_y film. Under applied positive bias, the Al oxidizes with the extracted oxygen ions at the interface and the oxygen contents are preserved near the conducting filamentary paths. Then, followed by the negative bias, the oxygen ions reverse back to annihilate the oxygen vacancies. This is what the Pd top electrode can not achieve because of noble metal properties of Pd and high mobility for oxygen ion inside Pd metal. Therefore, both the CW and CCW loop can be performed on PA samples, while only CW is observed on PH samples.

To further evaluate the performance of the PA memory device, the cycling endurance characteristics were measured on CW and CCW loop in dc voltage sweep mode. The device under CW loop could be continuously switching between HRS and LRS for more than 1000 cycles without switching failure, as shown in Fig. 3-46, while only 26 cycles under CCW loop (not shown here). The accumulation percentage of the set and reset voltage in both case was calculated, as shown in Fig. 3-47. Set

voltage and reset voltage distributes in a range of -0.7 ~ -0.9 V and 0.8 ~ 1 V on the CW operation, and in a range of 2.8 ~ 5.7 V and -1.1 ~ -2.2 V on the CCW operation, respectively. There might be other factors included in CCW loop such as oxidation and reduction of AlO_y, thus the RS mechanism may become complex to control. On the contrary, the amount of oxygen ions absorbed and extracted by TiN electrode is better controlled than the Al top electrode, which further confirms that the TiN can serve as a good oxygen reservoir under continuously switching cycles. Further detailed studies on the microscopic electrode/oxide interface are necessary to better control the RS characteristics for the nonvolatile memory application.

3.5 Conclusion

In this chapter, we discuss on a variety of factors to the resistive switching characteristics, including electrode effect, electrode thickness effect, rapid thermal annealing effect in Ar or O_2 circumstance, electrode process effect, and UV light irradiation effect. A model based on formation and rupture of the conducting filamentary paths through the preexisted oxygen vacancies or grain boundaries may be the possible switching mechanism for our HfO_x thin film. The electrode is a critical issue to determine the switching properties. Top portion of the HfO_x thin film is responsible for the resistance switching under the applied bias and can be well modulated by inserting reactive metal Al, thermal annealing and/or recovery, electrode process, and UV light exposure. To sum up, once more oxygen ions are induced onto the HfO_x surface, the switching properties can be greatly improved on operation voltage dispersion and high and low resistance values dispersion. However, the conducting paths may be stemmed when the treatment condition is longer. When the crystallinity of the HfO_x surface was changed, then the switching behaviors become unstable and the switching parameters become dispersed. A well chosen

electrode material and fabrication process effectively improves the resistive switching reliability.

The bipolar resistive switching characteristics also greatly depend on the electrode materials. The Pd/HfO_x/TiN devices only exhibit the clockwise current loop, while the Pd/Al/HfO_x/TiN devices can perform both the clockwise and counterclockwise current loop. This may be attributed an interfacial layer formed at the Al/HfO_x interface, because the reactive metal Al will easily oxidize with the underlying HfO_x. The interfacial layer HfAlO composed of defects such as oxygen vacancies or metallic defects, may be responsible for the migrated oxygen ions under applied bias. In addition, the effect of inserted Al thin layer can improve switching characteristics owing increasing the crystallization temperature of HfO_x film. Since the devices are free from thermal fluctuation factor, the structure of Pd/Al/HfO_x/TiN structure provides a better nonpolar resistive switching characteristic and reliable switching behavior, which widen the nonvolatile memory devices application.

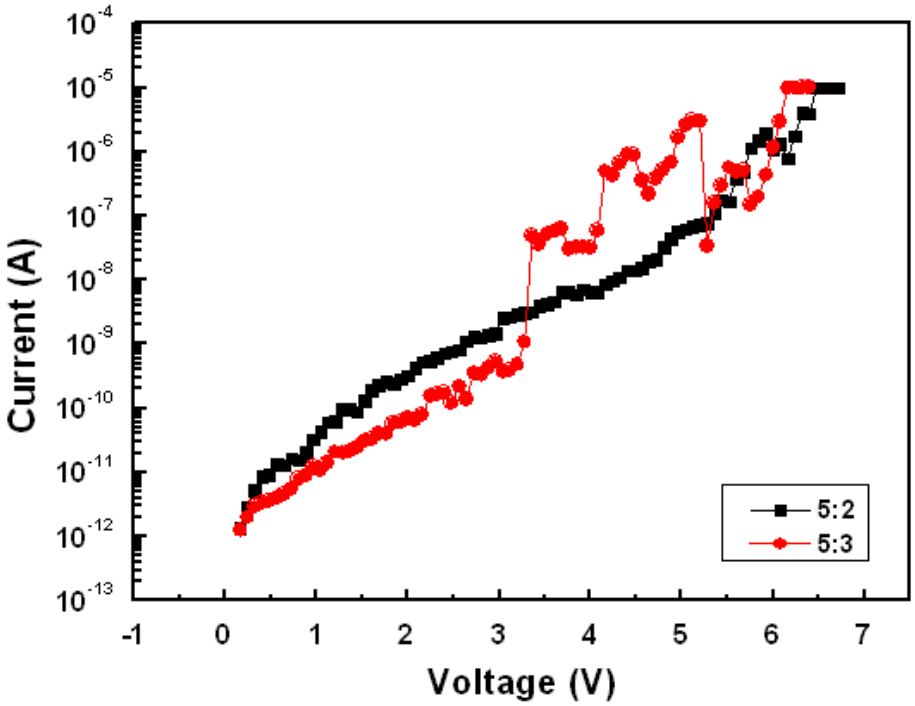

Fig. 3-1 The forming characteristics of the HfO_x samples fabricated with different composition reactants ratio of $HfCl_4$: H_2O = 5 : 2 or 5 : 3 during ALD process.

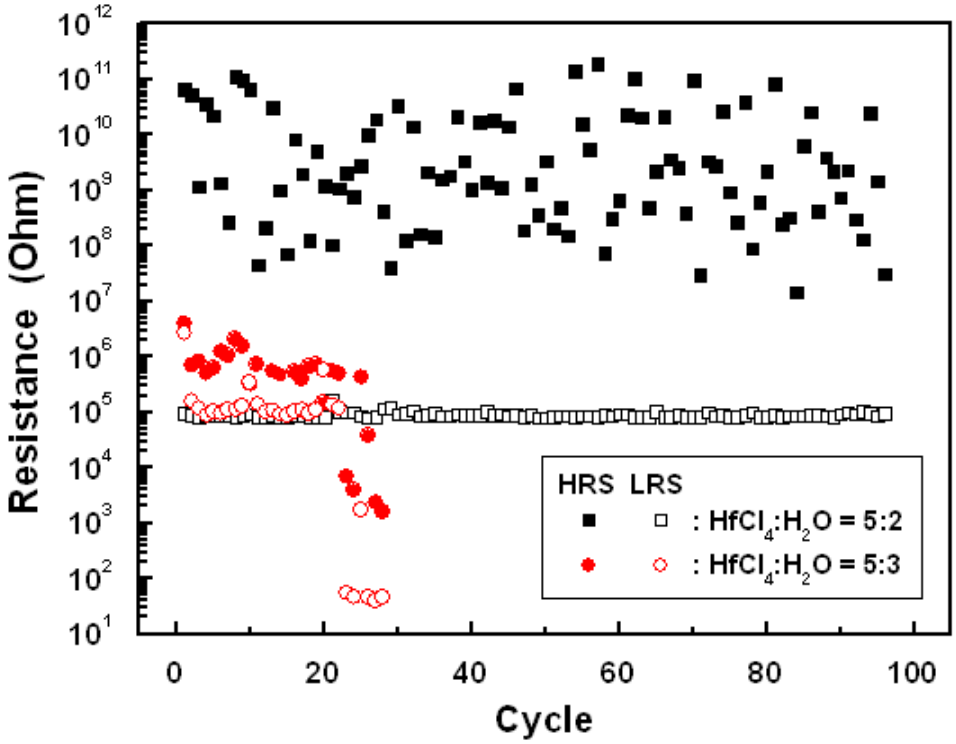

Fig. 3-2 The high and low resistance values of HfO_x/TiN device with different composition reactants ratio of $HfCl_4$: H_2O = 5 : 2 or 5 : 3 during ALD process

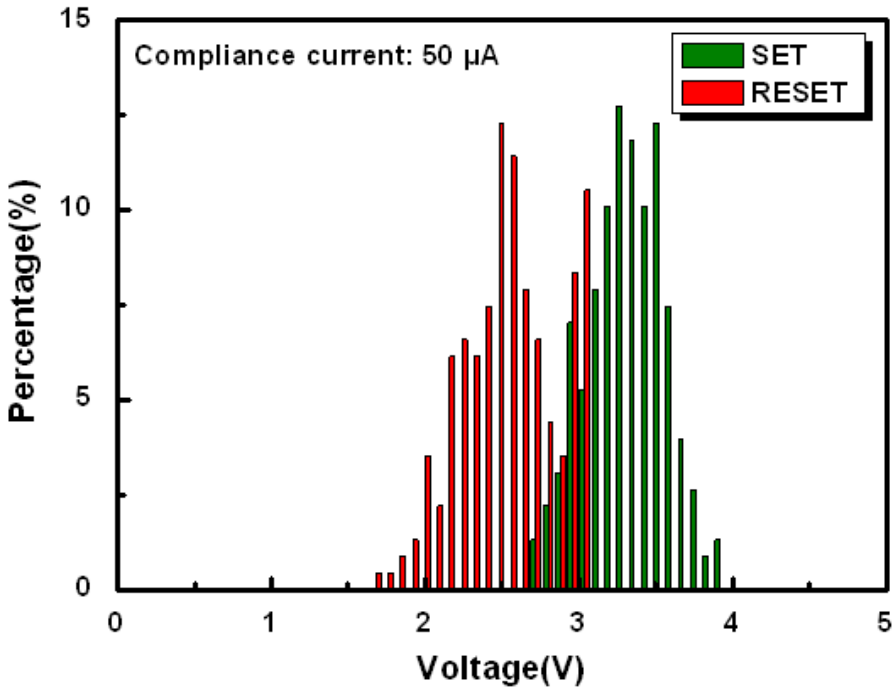

Fig. 3-3 The operation voltage percentage distribution of the HfO_x samples fabricated with composition reactants ratio of $HfCl_4$: H_2O = 5 : 2 during ALD process.

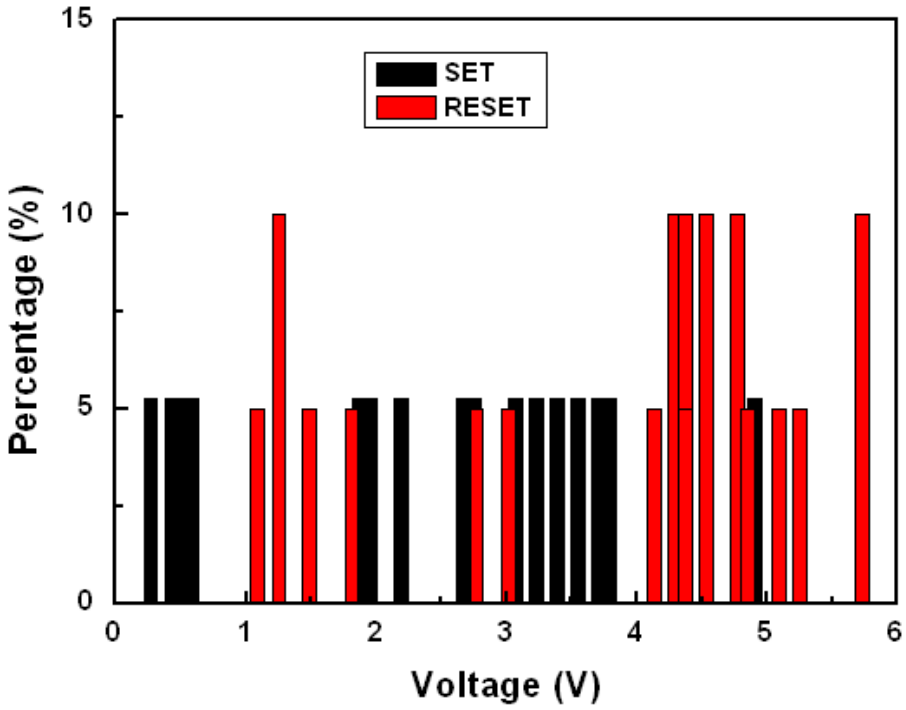

Fig. 3-4 The operation voltage percentage distribution of the HfO_x samples fabricated with composition reactants ratio of $HfCl_4$: H_2O = 5 : 3 during ALD process.

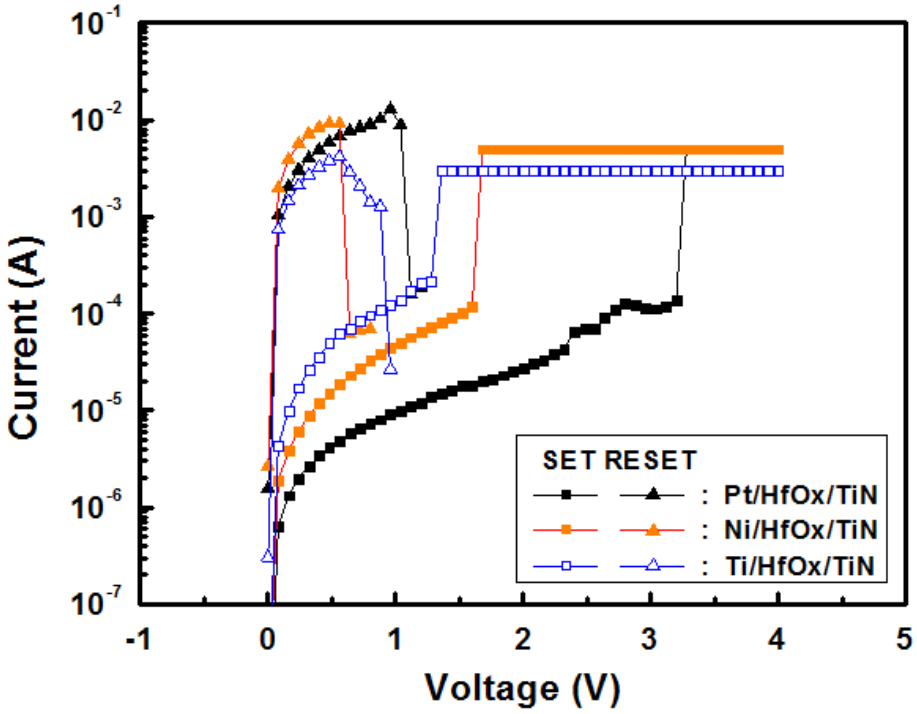

Fig. 3-5 The resistive switching behaviors of HfO_x/TiN device using Pt, Ni, and Ti top metal electrode.

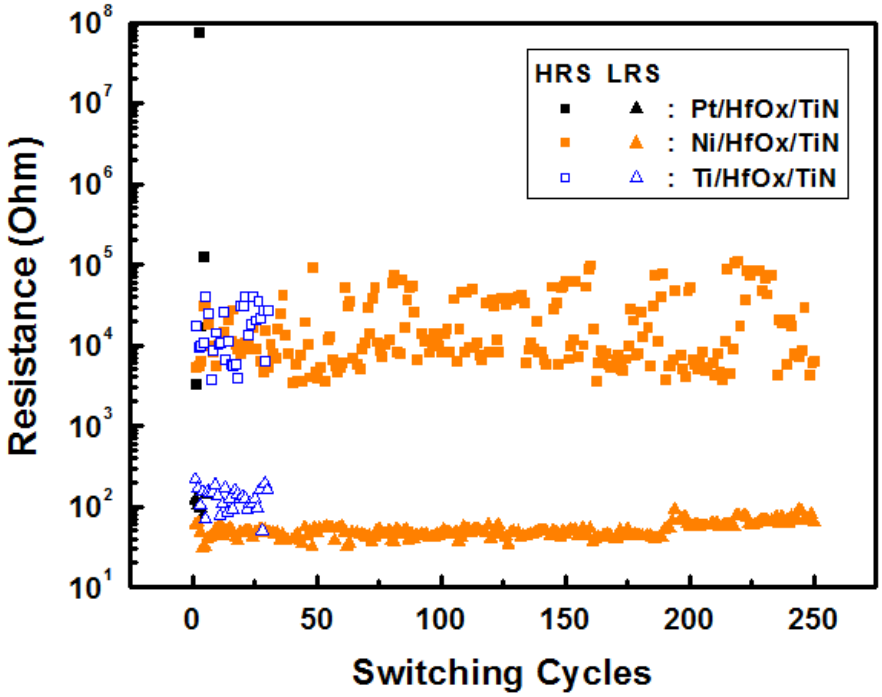

Fig. 3-6 The resistance values of high and low resistance state at 0.1 V of HfO_x/TiN device using Pt, Ni, and Ti top metal electrode.

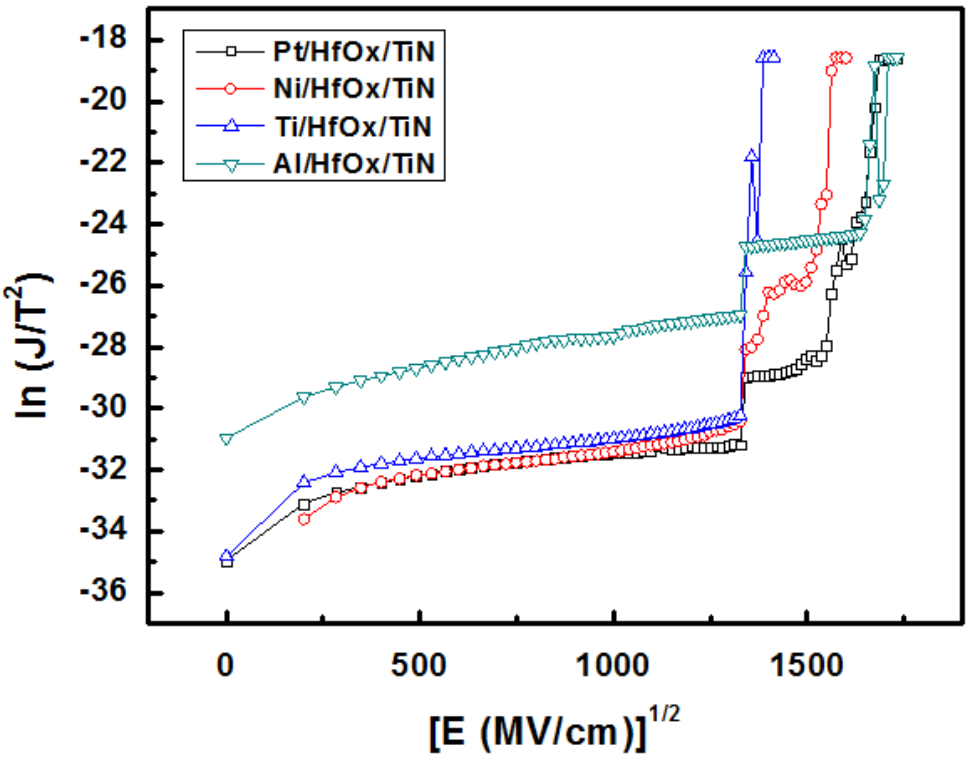

Fig. 3-7 Ln (J/T^2)-$E^{1/2}$ plot of the TE/HfO_x/TiN structure with top electrode TE=Pt, Ni, Ti and Al.

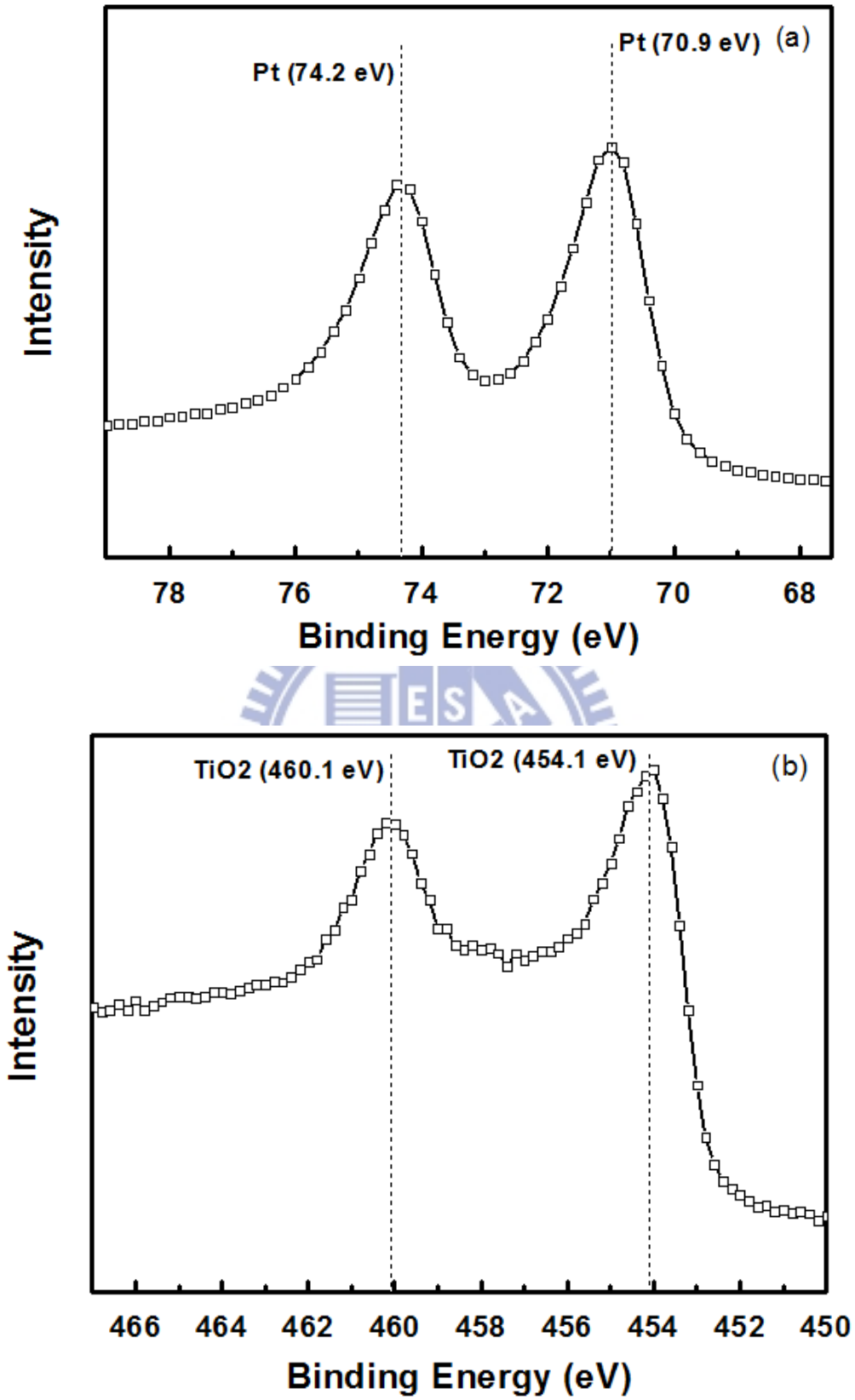

Fig. 3-8 XPS core level spectra of (a) Pt 4f and (b) Ti 2p at the interface region.

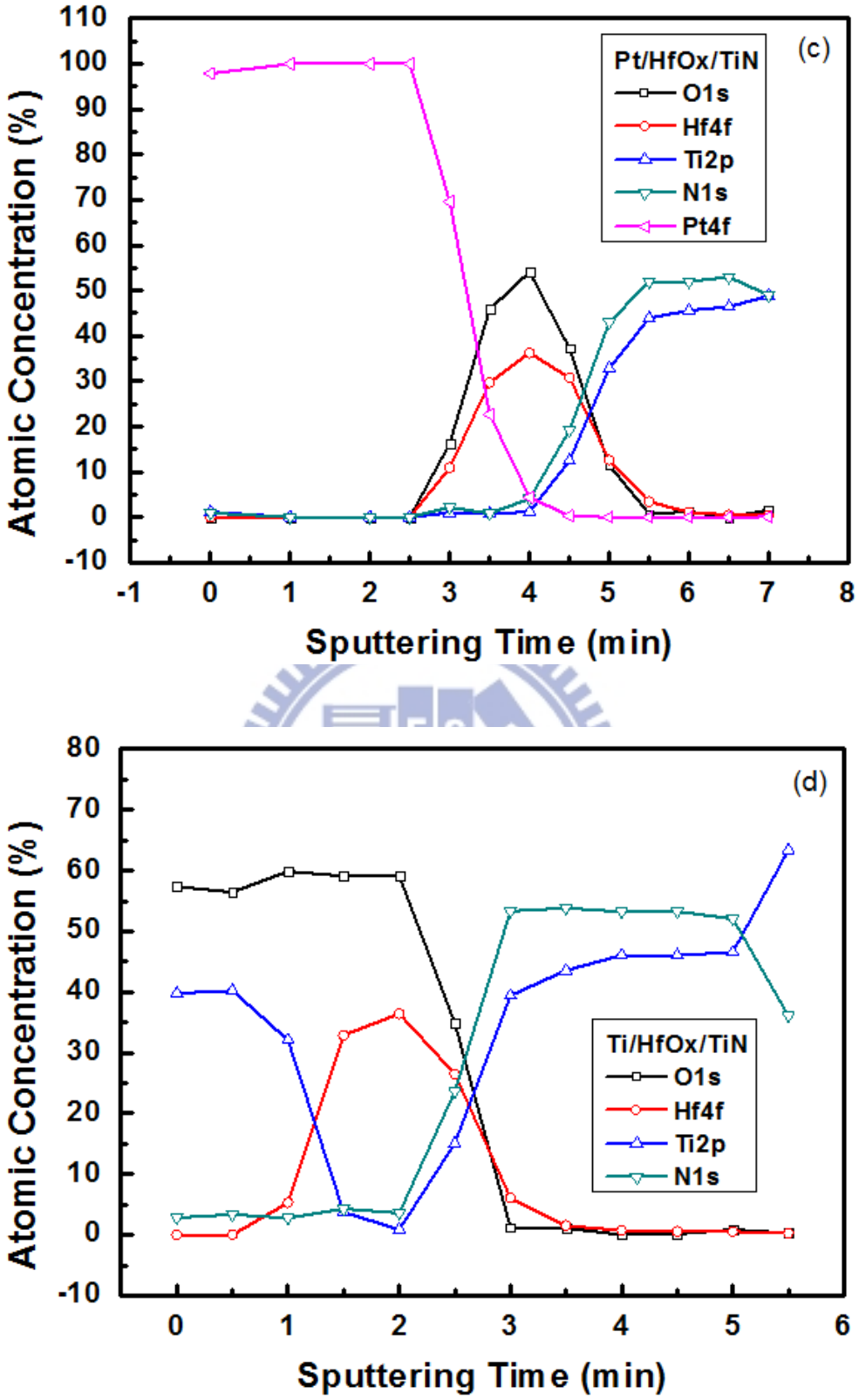

Fig. 3-8 AES depth profile of (c) Pt/HfO_x/TiN and (d) Ti/HfO_x/TiN structure.

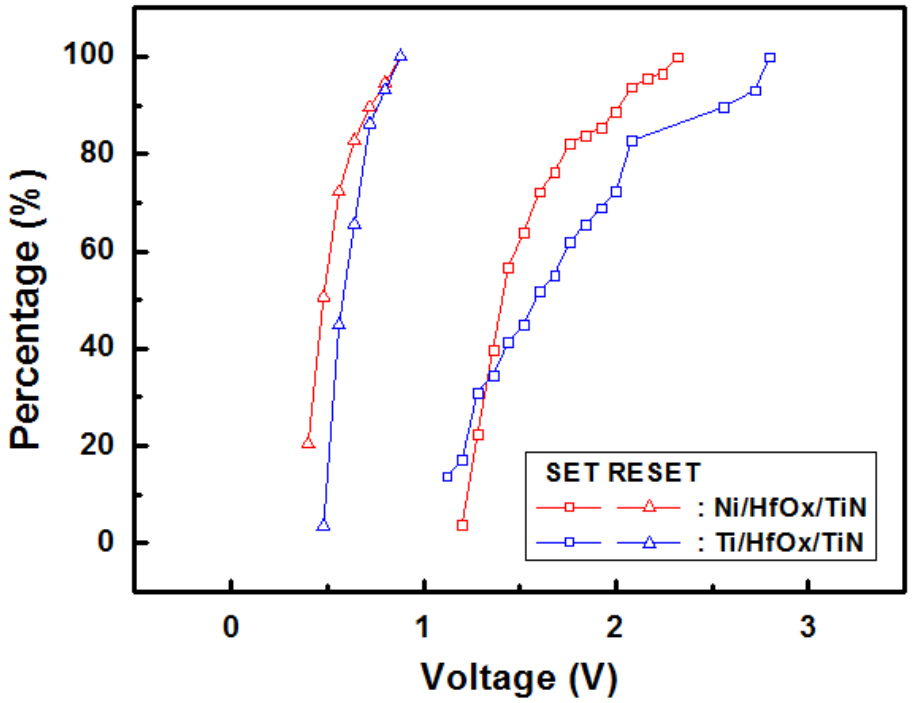

Fig. 3-9 Accumulative percentage of the operation voltage of Ni/HfO_x/TiN and Ti/HfO_x/TiN capacitor device.

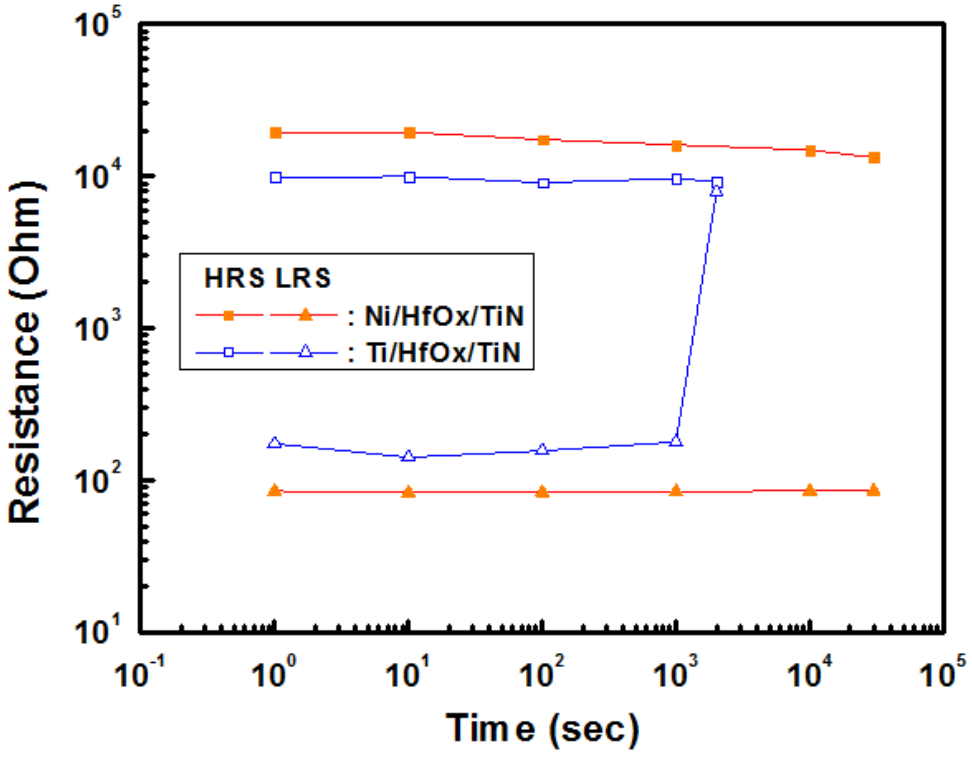

Fig. 3-10 Data retention test result of both high and low resistance values at 0.1 V of Ni/HfO_x/TiN and Ti/HfO_x/TiN capacitor device.

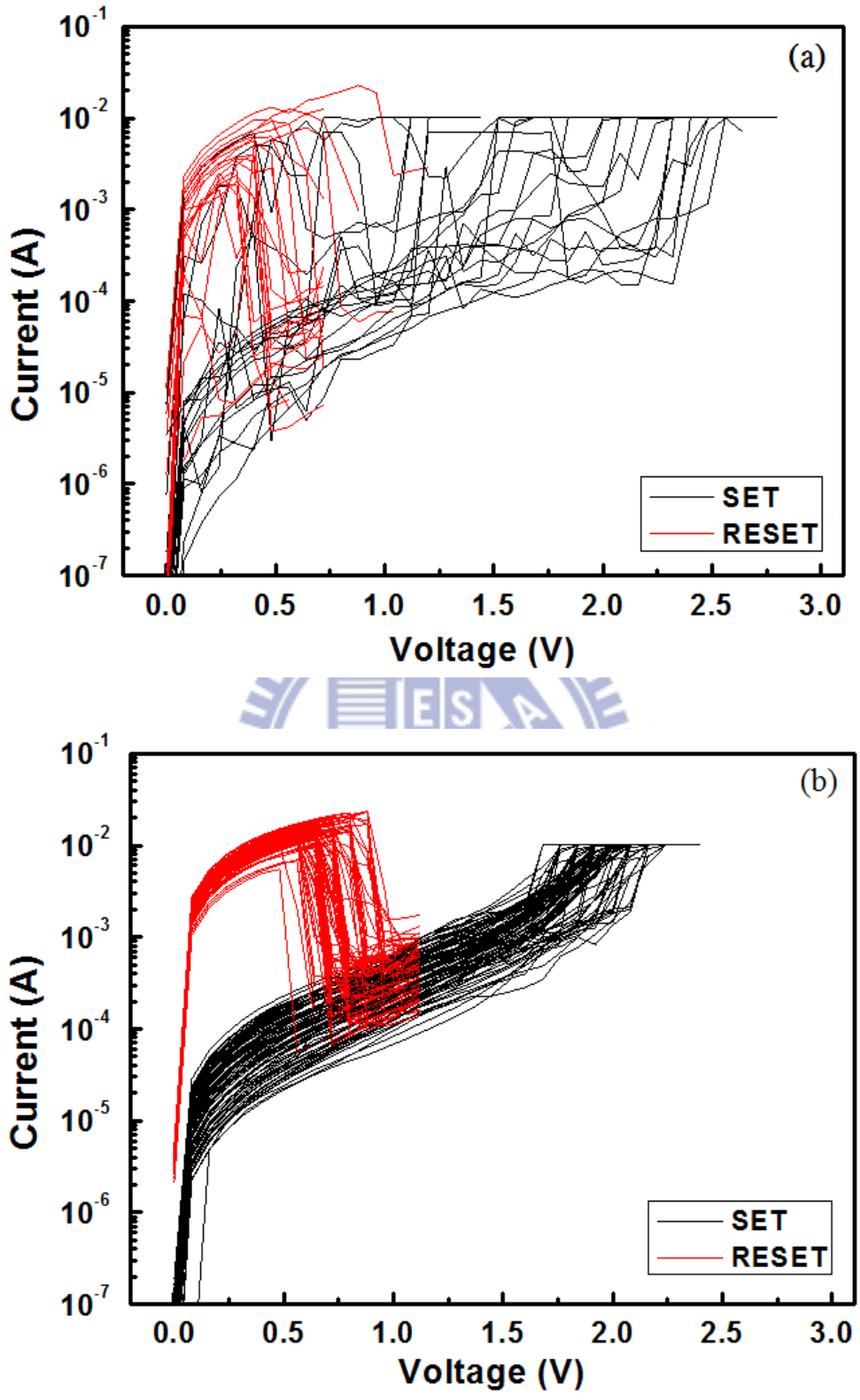

Fig. 3-11 The continuous unipolar resistive switching I-V curves in (a) Pd/HfO_x/TiN and (b) Pd/Al(50Å)/HfO_x/TiN capacitor device.

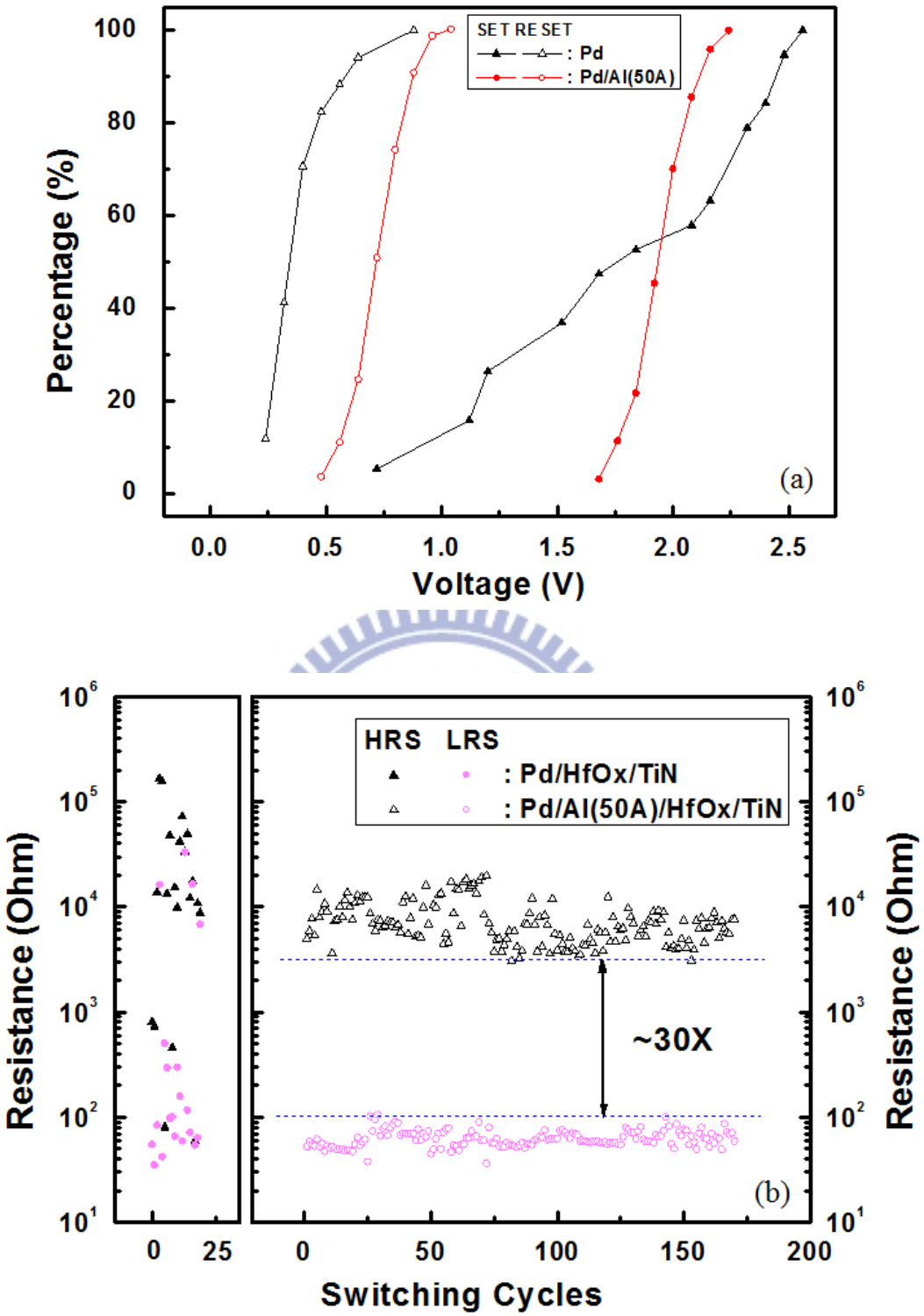

Fig. 3-12 (a) Accumulative percentage of the operation voltage of Pd/HfO_x/TiN and Pd/Al(50Å)/HfO_x/TiN capacitor device. (b) Endurance test of Pd/HfO_x/TiN (left) and Pd/Al(50Å)/HfO_x/TiN (right) capacitor device at 0.4V.

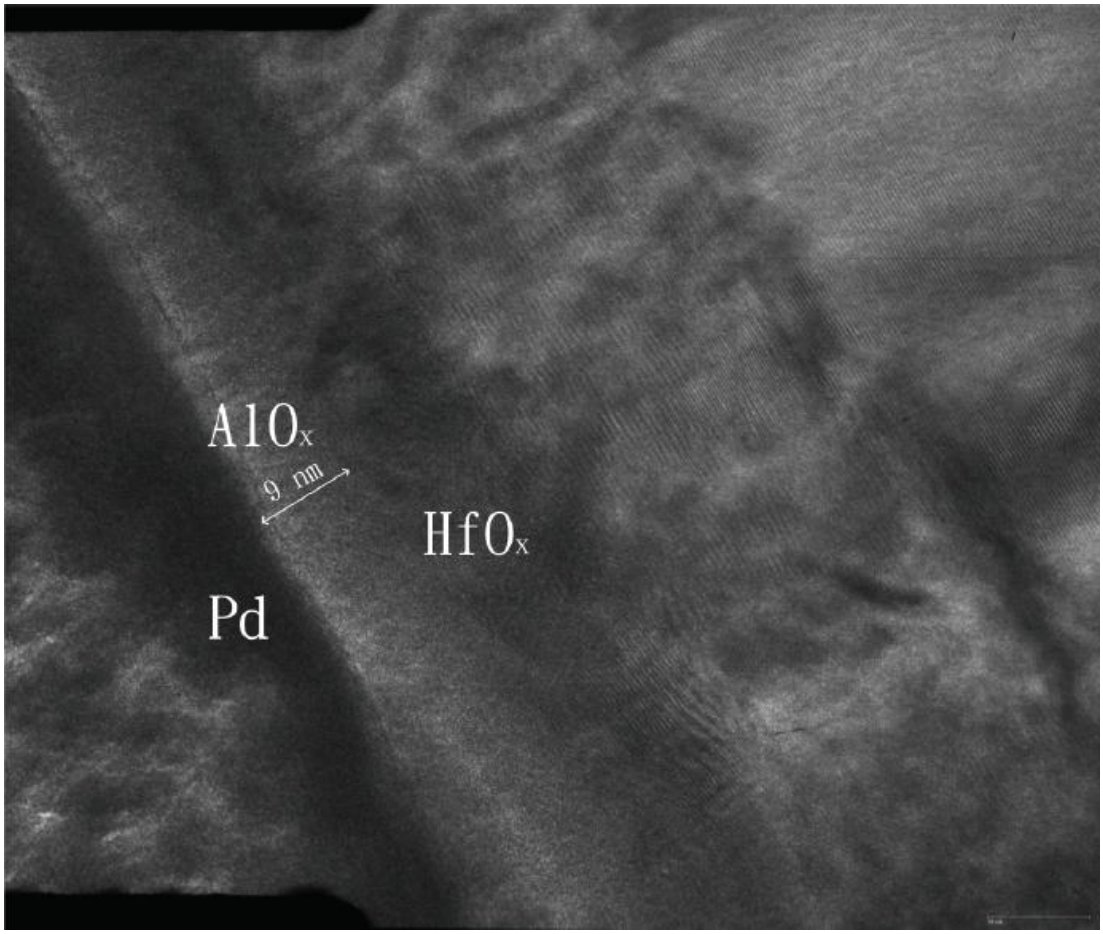

Fig. 3-13 The cross-sectional TEM iamge of the Pd/Al(35Å)/HfO_x/TiN structure.

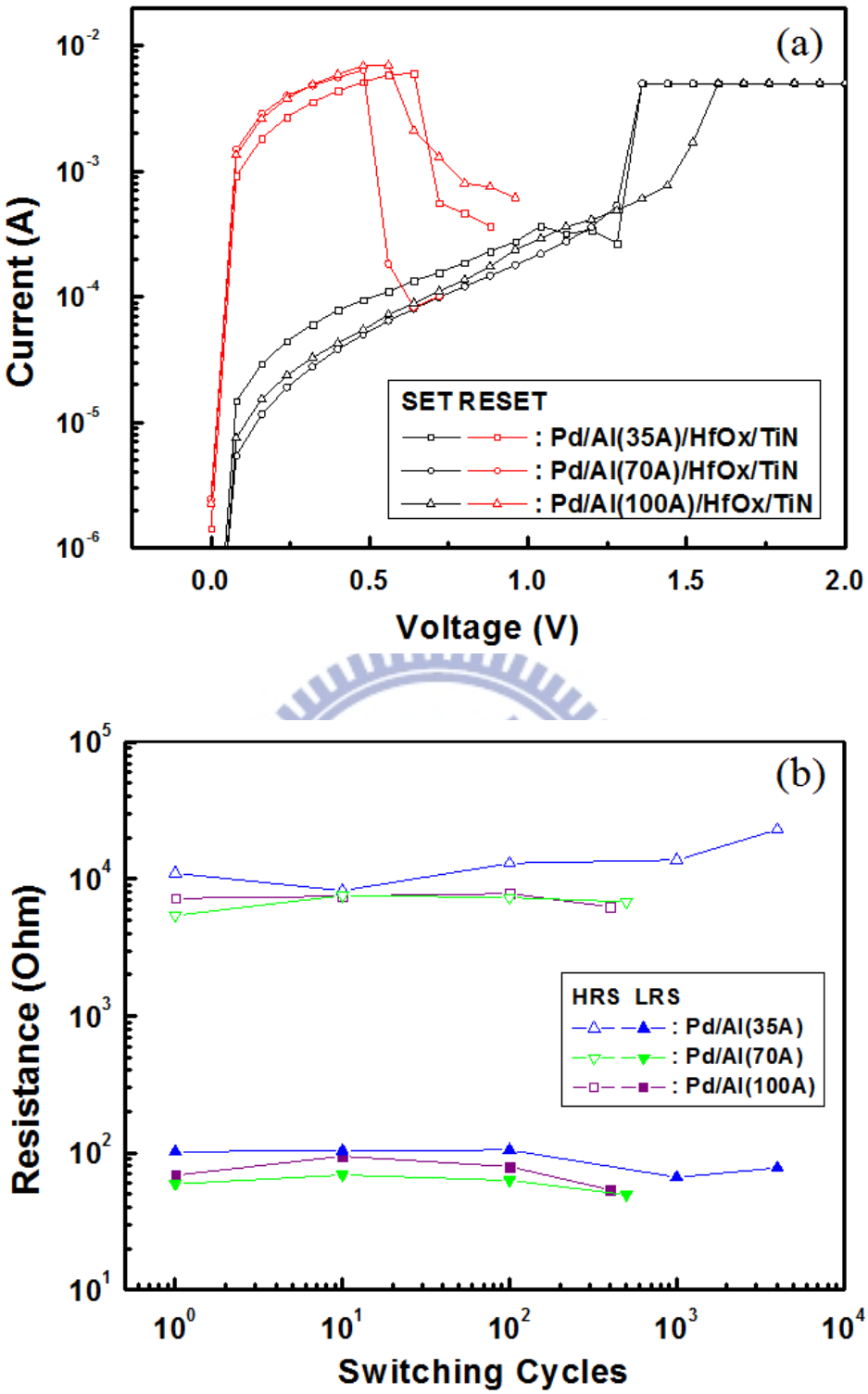

Fig. 3-14 (a) The resistive switching behaviors of the Pd/HfO_x/TiN device with Al layer inserted of 35Å, 70Å, and 100Å. (b) Comparison of the endurance test of Pd/HfO_x/TiN device with Al layer inserted of 35Å, 70Å, and 100Å.

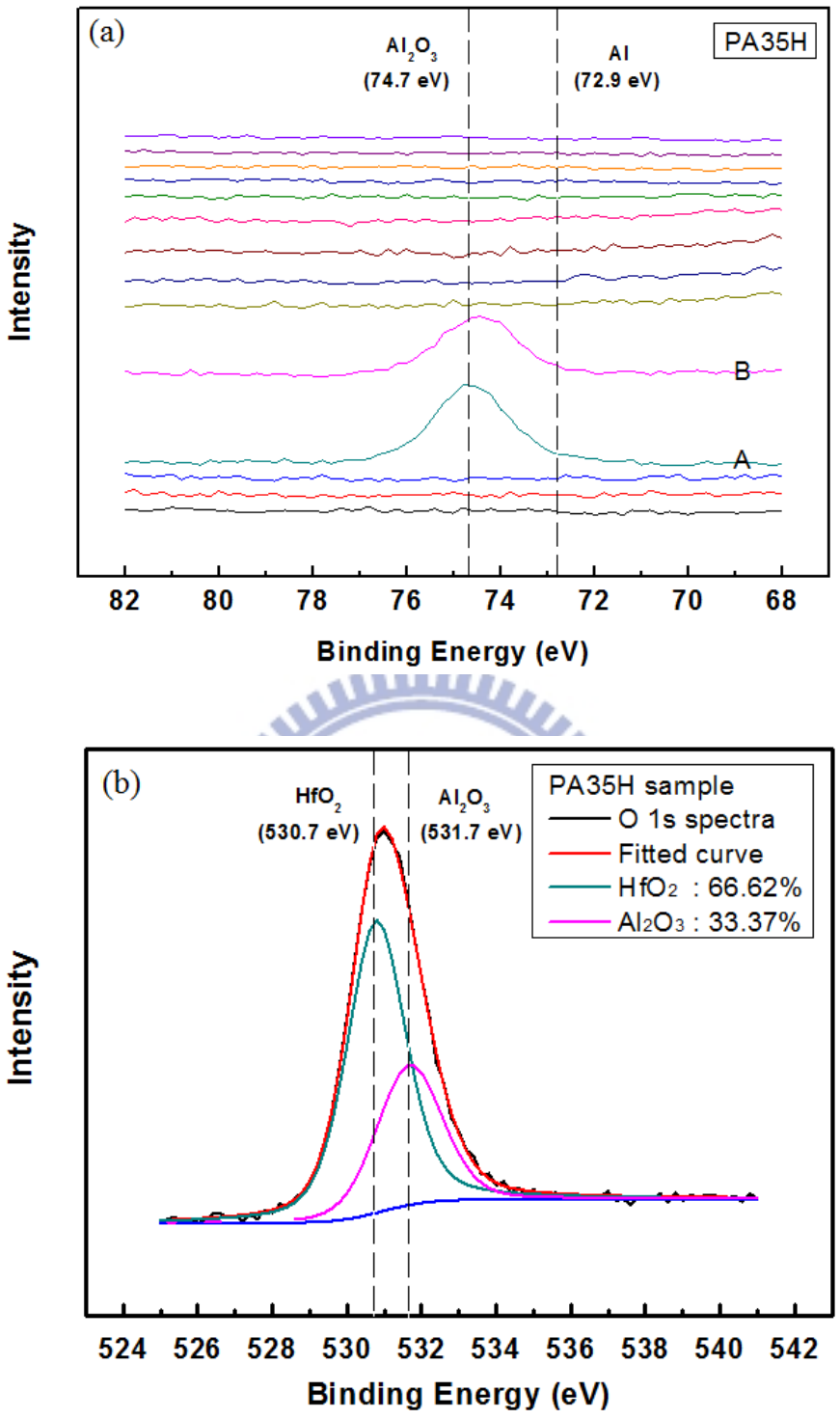

Fig. 3-15 Depth profiling of Al 2p core level spectra of Pd/HfO_x/TiN structures with thickness of (a) 35Å Al layer inserted after every 2 min Ar+ ion sputtering. As going from the bottom to the top, the spectra describe spectral changes from the top to the bottom electrode. The O 1s spectra of (b) Step B was also analyzed, and deconvoluted to fit the spectra into the two peak (530.7 and 531.7 eV), which correspond to HfO_2 and Al_2O_3 states, respectively.

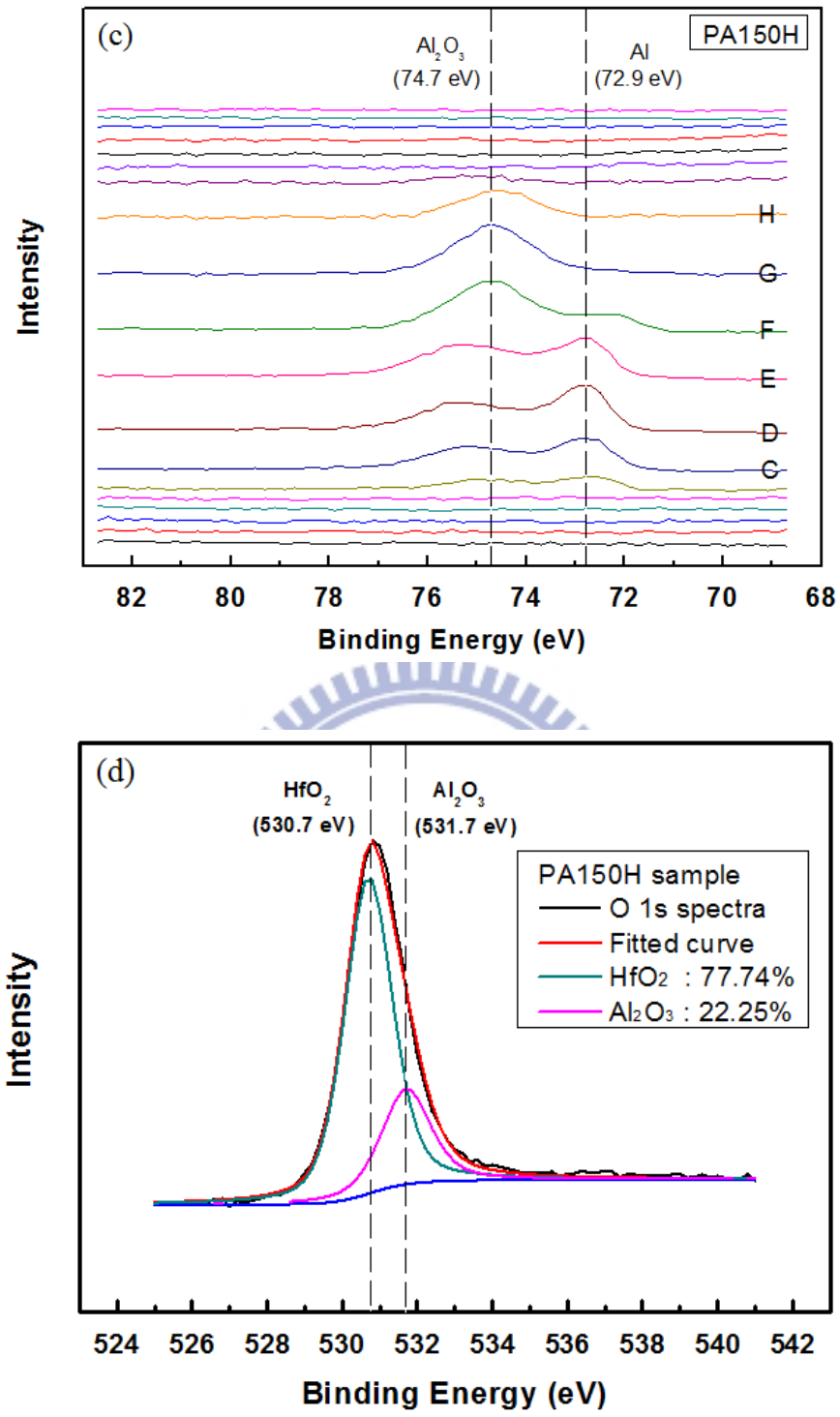

Fig. 3-15 Depth profiling of Al 2p core level spectra of Pd/HfO_x/TiN structures with thickness of (c) 150Å Al layer inserted after every 2 min Ar+ ion sputtering. As going from the bottom to the top, the spectra describe spectral changes from the top to the bottom electrode. The O 1s spectra of (d) Step H was also analyzed, and deconvoluted to fit the spectra into the two peak (530.7 and 531.7 eV), which correspond to HfO_2 and Al_2O_3 states, respectively.

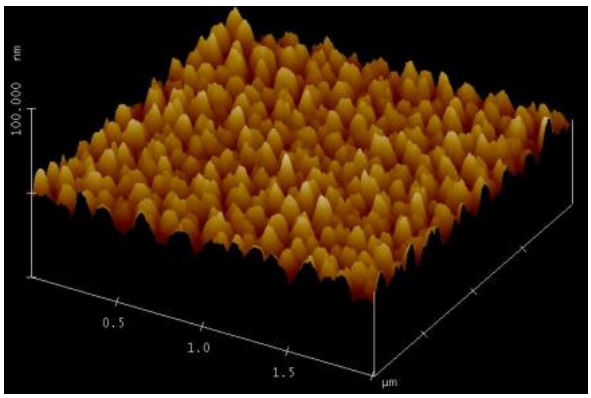

Fig. 3-16(a) AFM image of the as-grown HfO_x films.

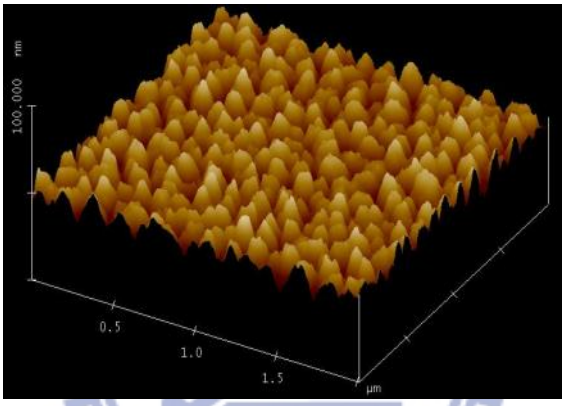

Fig. 3-16(b) AFM image of the as-grown HfO_x films under Ar RTA 400 °C for 90 seconds.

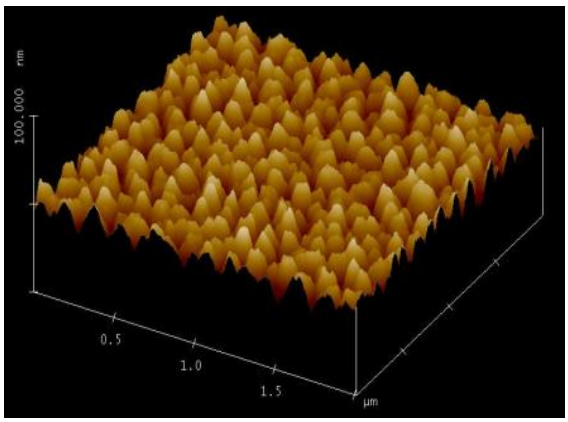

Fig. 3-16(c) AFM image of the as-grown HfO_x films under Ar RTA 500 °C for 90 seconds.

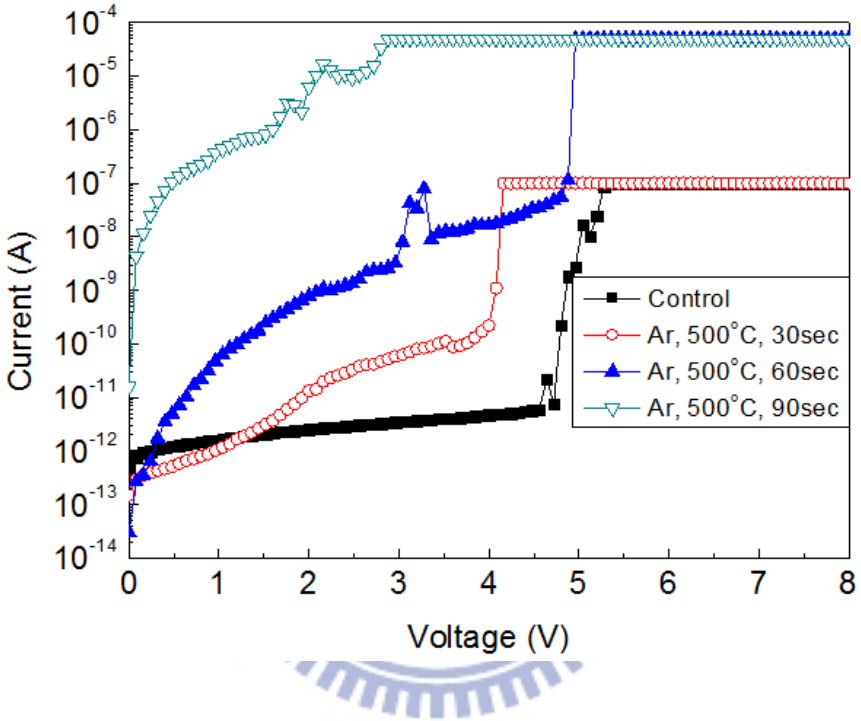

Fig. 3-17 Comparison on the forming process of Ni/HfO_x/TiN samples under different Ar RTA treatment conditions.

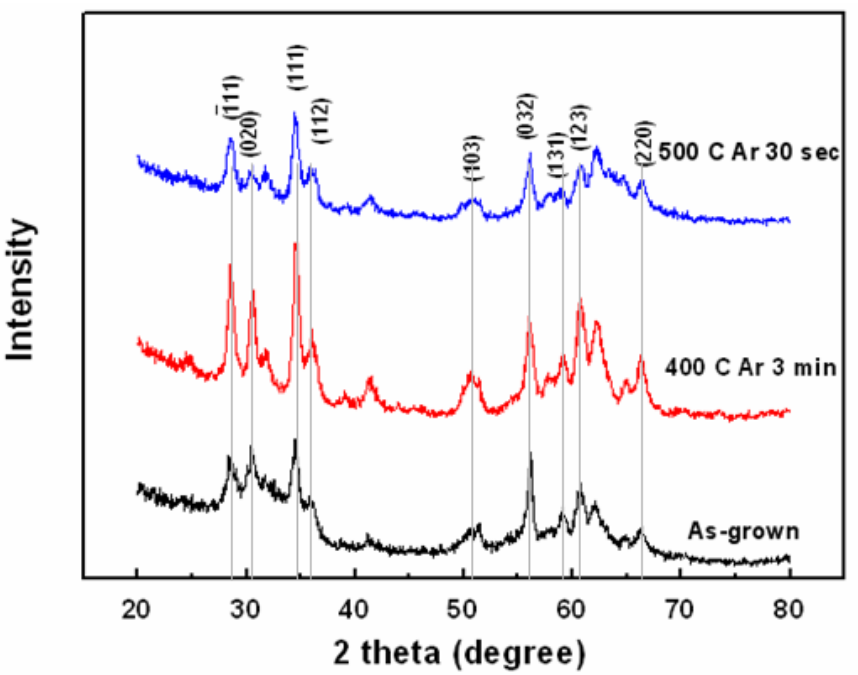

Fig. 3-18(a) XRD patterns of the HfO_x-based memory devices at various Ar RTA temperatures and treatment time.

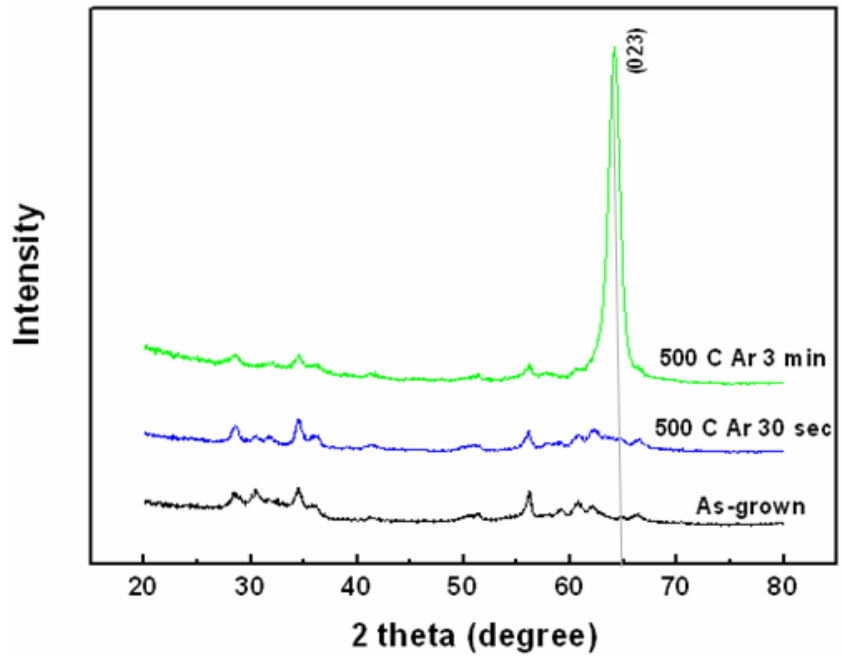

Fig. 3-18(b) XRD patterns of the HfO_x-based memory devices changes to strong (023) orientation when treated under longer treatment time.

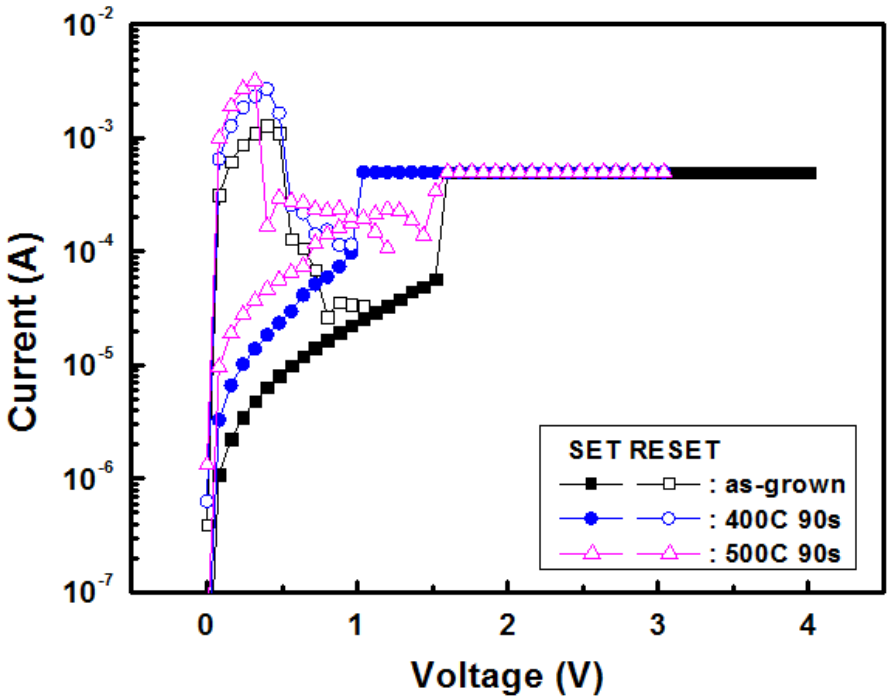

Fig. 3-19 The resistive switching behaviors of the Ni/HfO_x/TiN structures at different Ar RTA temperature for 90 seconds.

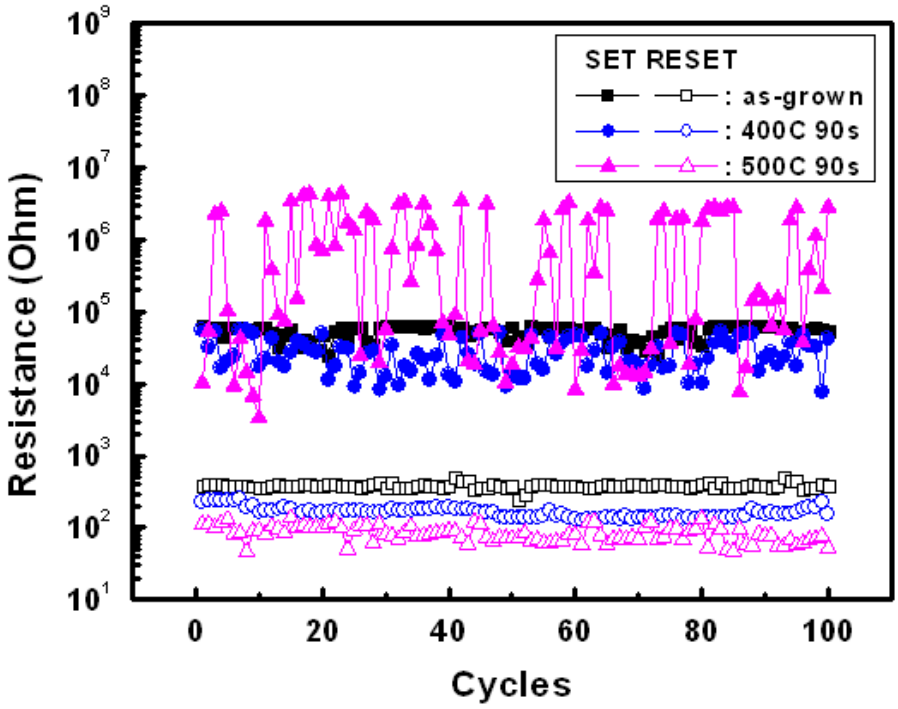

Fig. 3-20 The high and low resistive values at 0.1 V of the Ni/HfO_x/TiN structures at different Ar RTA temperature for 90 seconds.

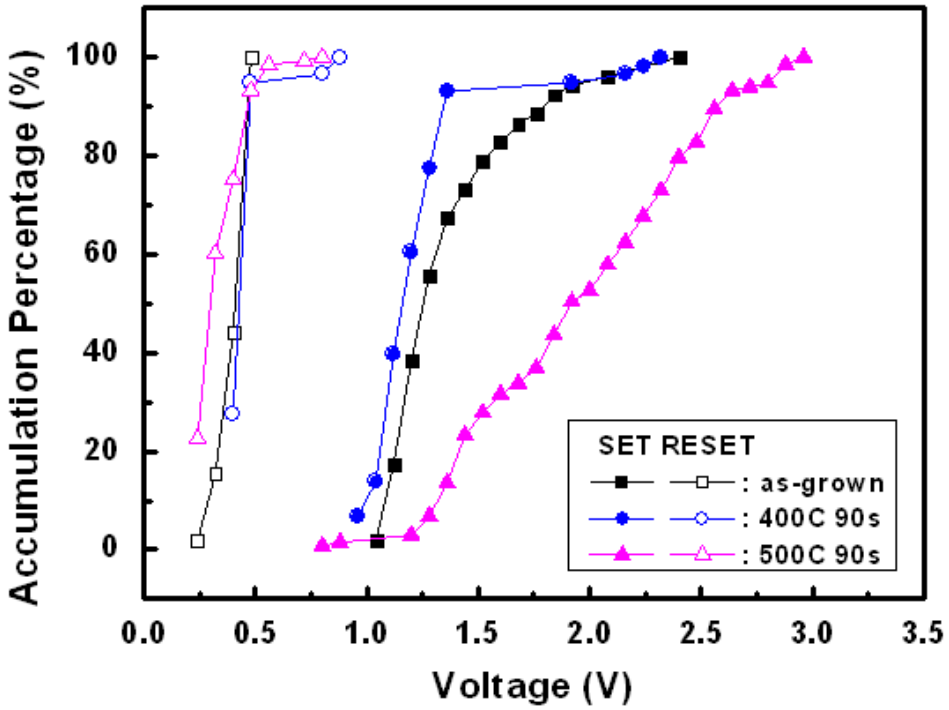

Fig. 3-21 The SET and RESET voltage distribution of the Ni/HfO_x/TiN structures at different Ar RTA temperature for 90 seconds.

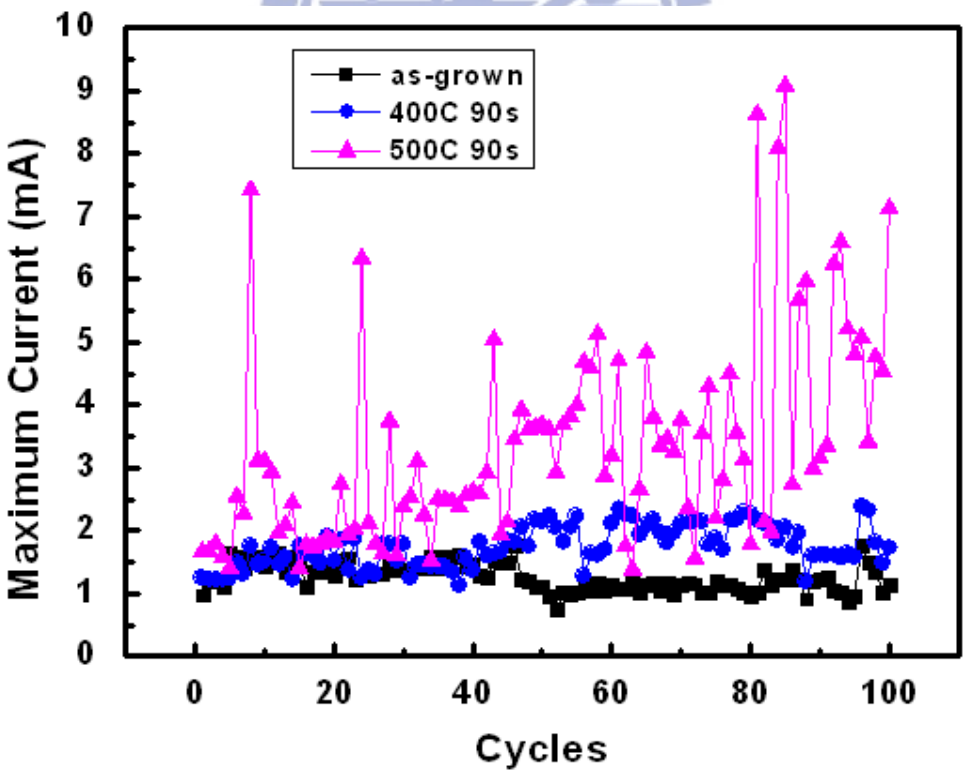

Fig. 3-22 The distribution of the maximum reset current of the Ni/HfO_x/TiN structures at different Ar RTA temperature for 90 seconds.

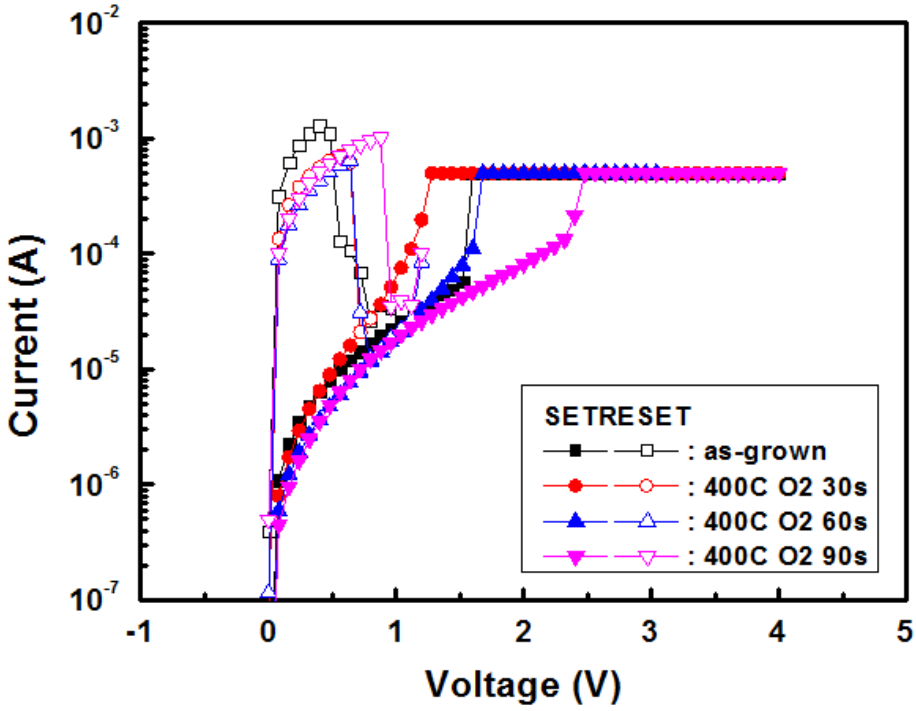

Fig. 3-23 Relative unipolar resistive switching curves of the Ni/HfO_x/TiN devices at various RTA treatment conditions in O_2 ambient for 400 °C.

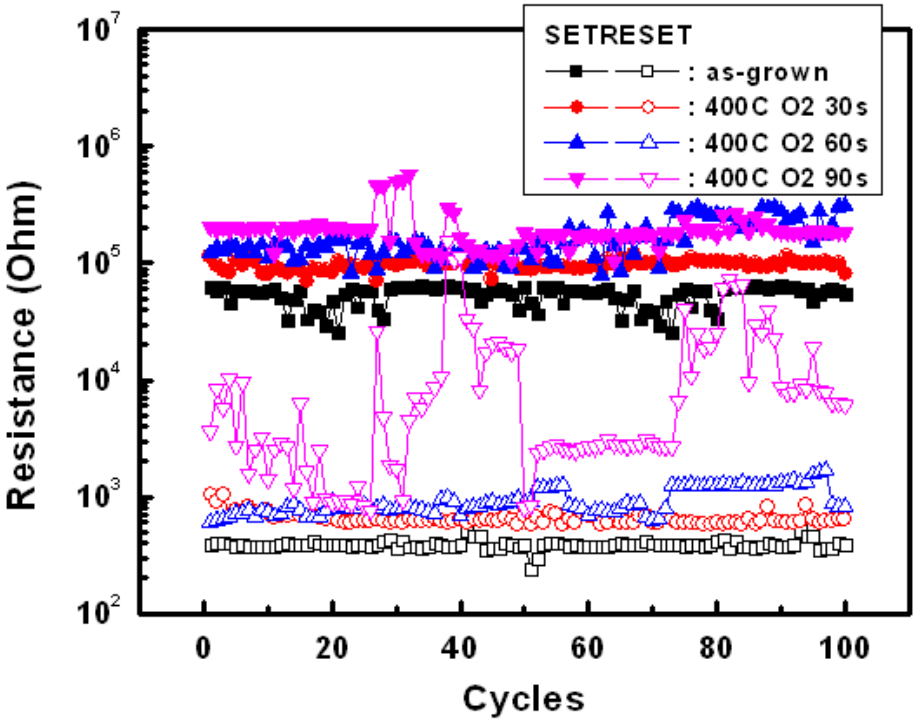

Fig. 3-24 Endurance characteristics of the Ni/HfO_x/TiN devices at various RTA treatment conditions in O_2 ambient for 400 °C.

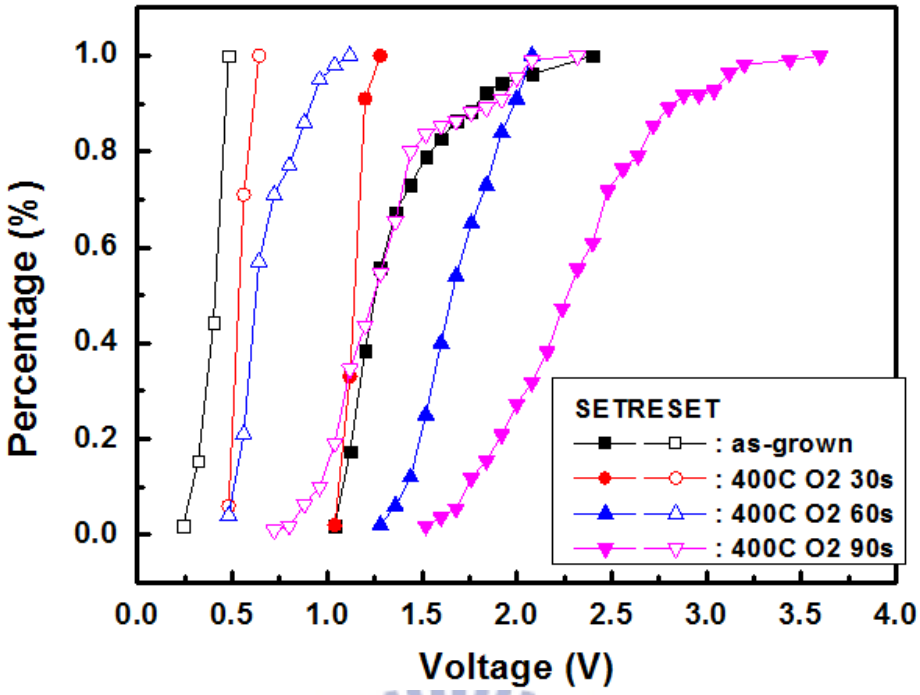

Fig. 3-25 Operation voltage values distribution of the Ni/HfO_x/TiN devices at various RTA treatment conditions in O_2 ambient for 400 °C.

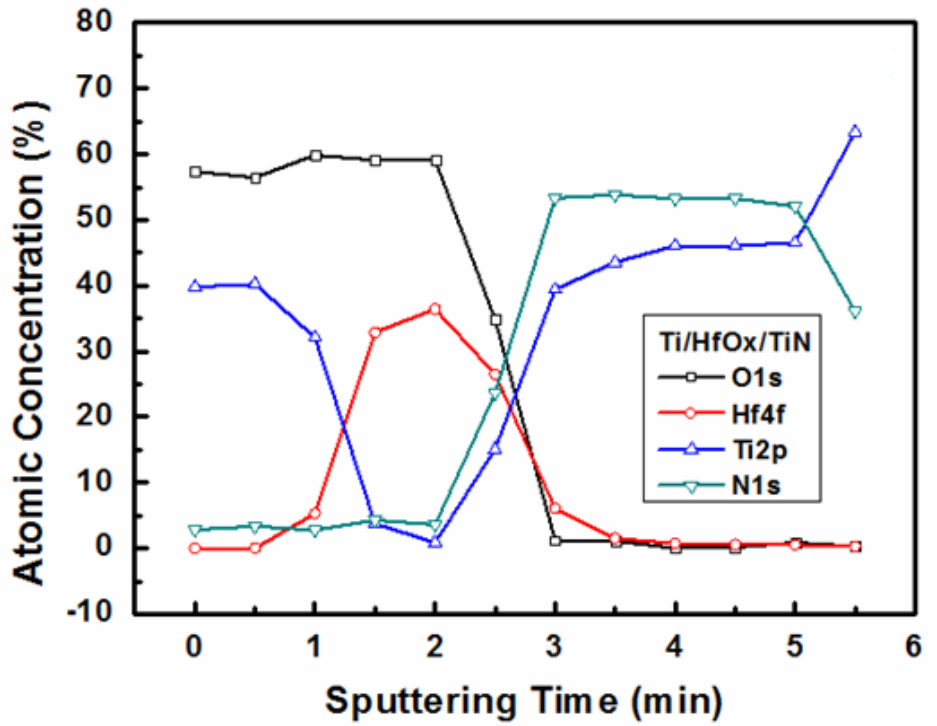

Fig. 3-26 AES depth profile of the Ti/HfO_x/TiN structure.

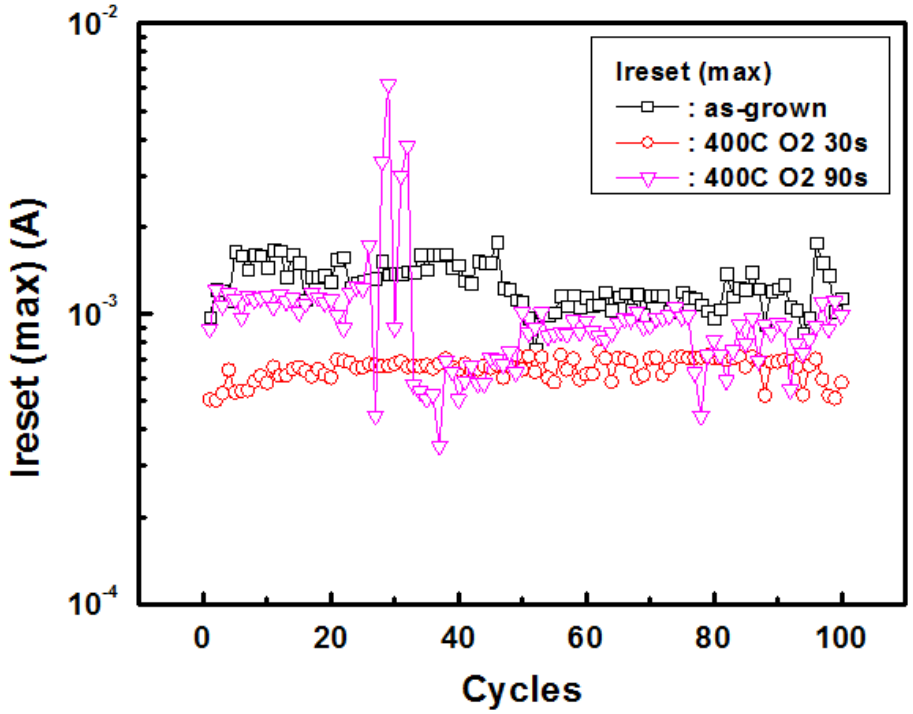

Fig. 3-27 Comparison on the I_{reset}(max) of the Ni/HfO_x/TiN devices at various RTA treatment conditions in O_2 ambient for 400 °C.

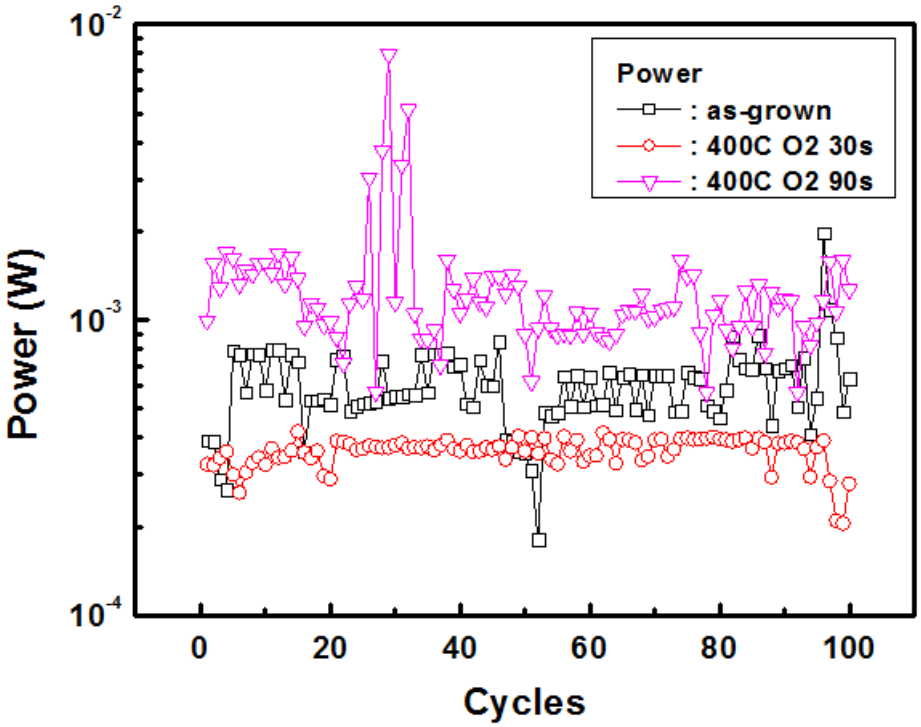

Fig. 3-28 Comparison on the RESET switching power of the Ni/HfO_x/TiN devices at various RTA treatment conditions in O_2 ambient for 400 °C.

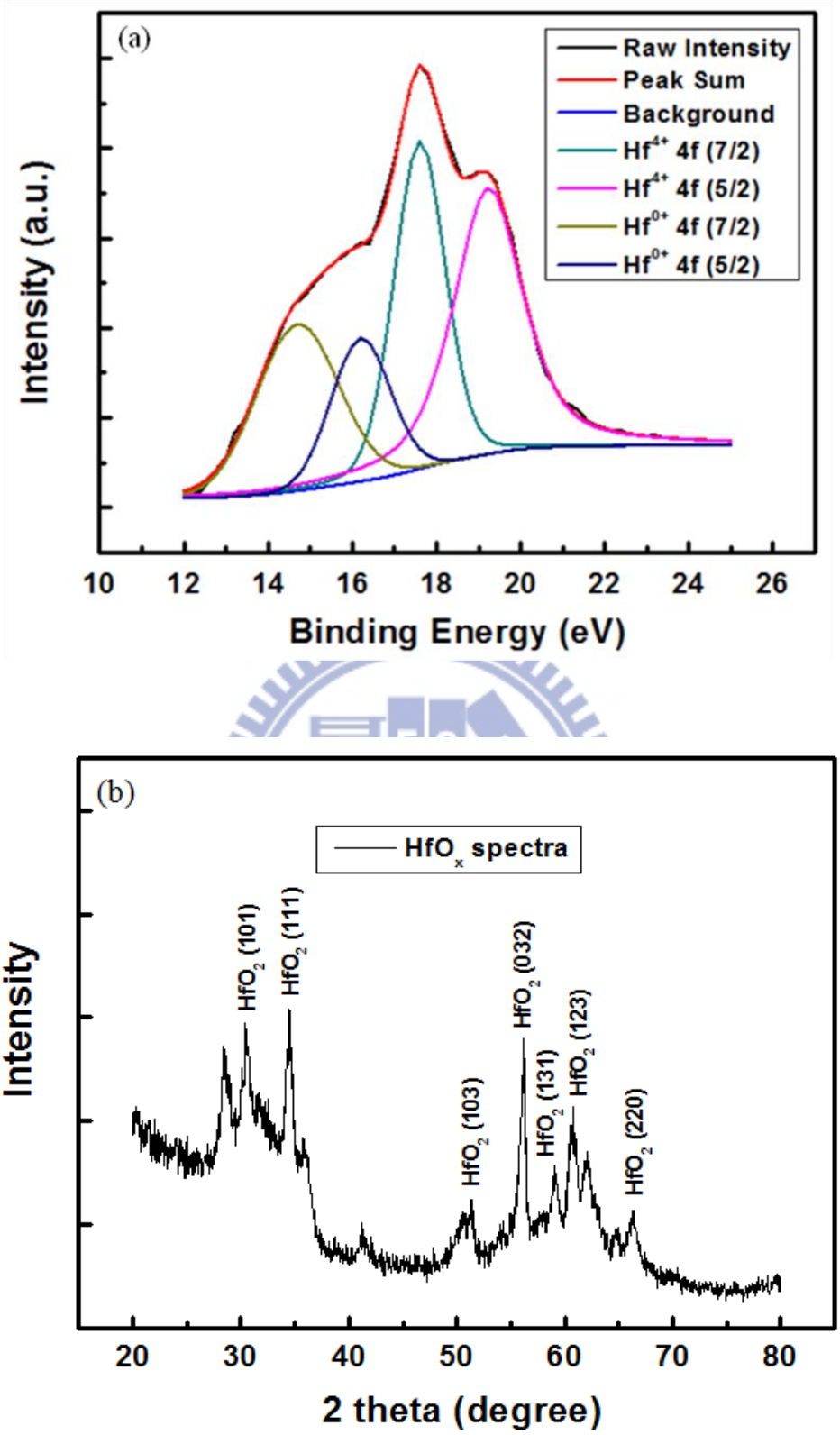

Fig. 3-29 (a) XPS spectra of Hf $4f_{5/2}$, $4f_{7/2}$ and Hf^{4+} $4f_{5/2}$, $4f_{7/2}$. (b) XRD patterns of HfO_x thin films deposited on the $TiN/SiO_2/Si$ substrate. Multiple red lines represent the intensity of various orientation peaks of the HfO_2 film.

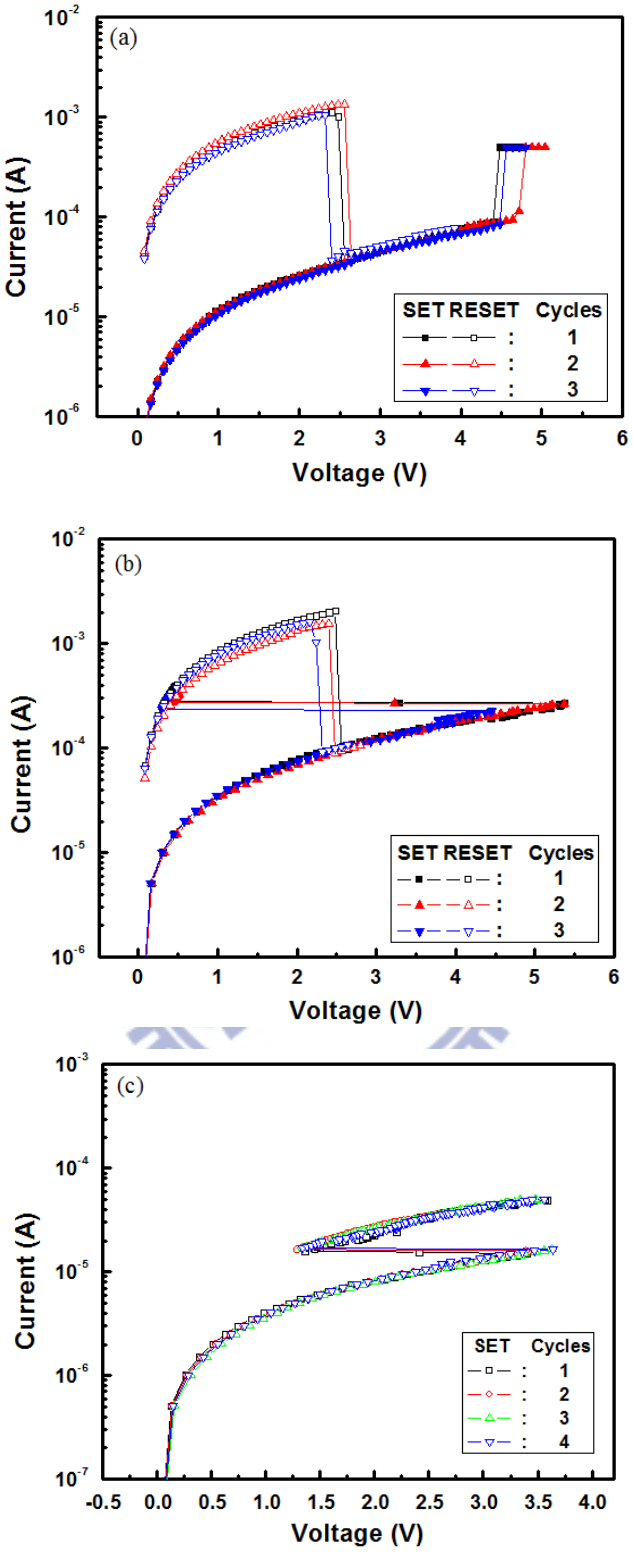

Fig.3-30 I-V characteristics of the Pt(E)/HfO_x/TiN sample using the (a) voltage mode operation for SET and RESET process, (b) current mode operation for SET and voltage mode for RESET processes under current compliance of 0.5 mA, and (c) current mode operation for SET under current compliance of 50 μA.

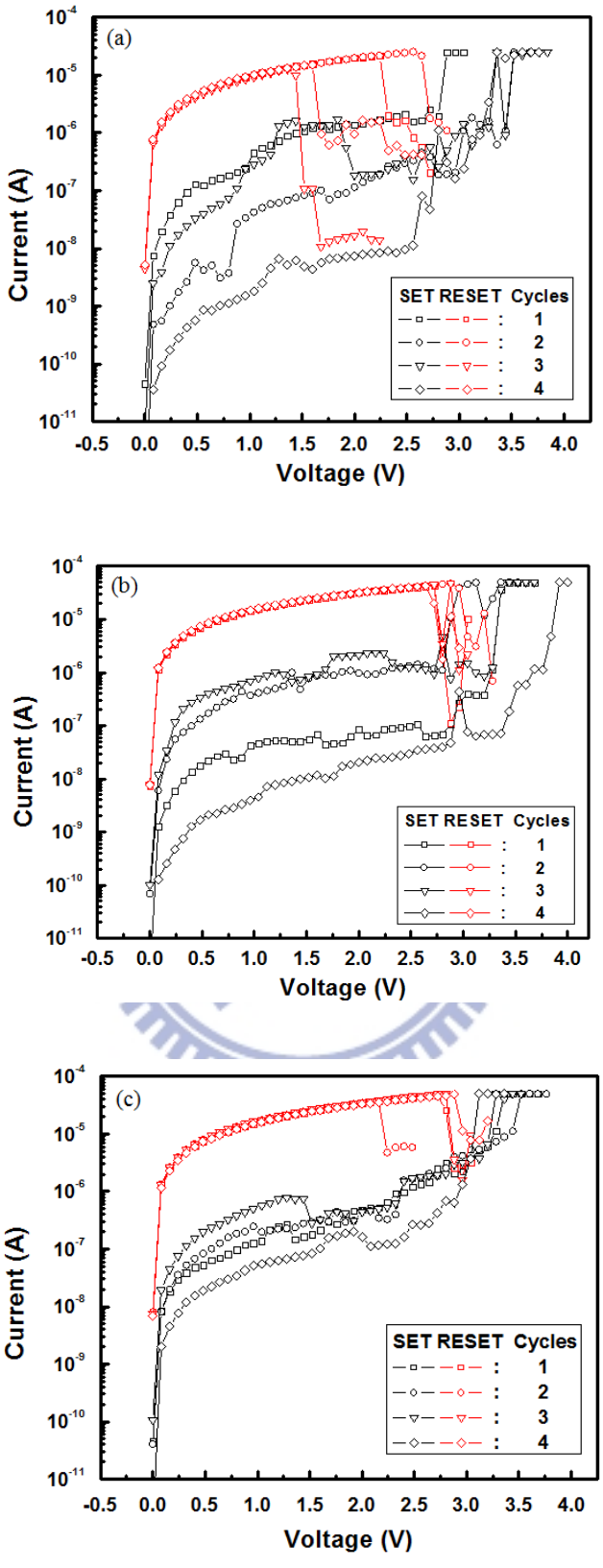

Fig. 3-31 Typical I-V curves of 4 consecutive sweeping cycles under voltage-mode operation of (a) Pt(S)/HfO_x/TiN, (b) Pt(E50+S)/HfO_x/TiN, and (c) Pt(E150+S)/HfO_x/TiN devices.

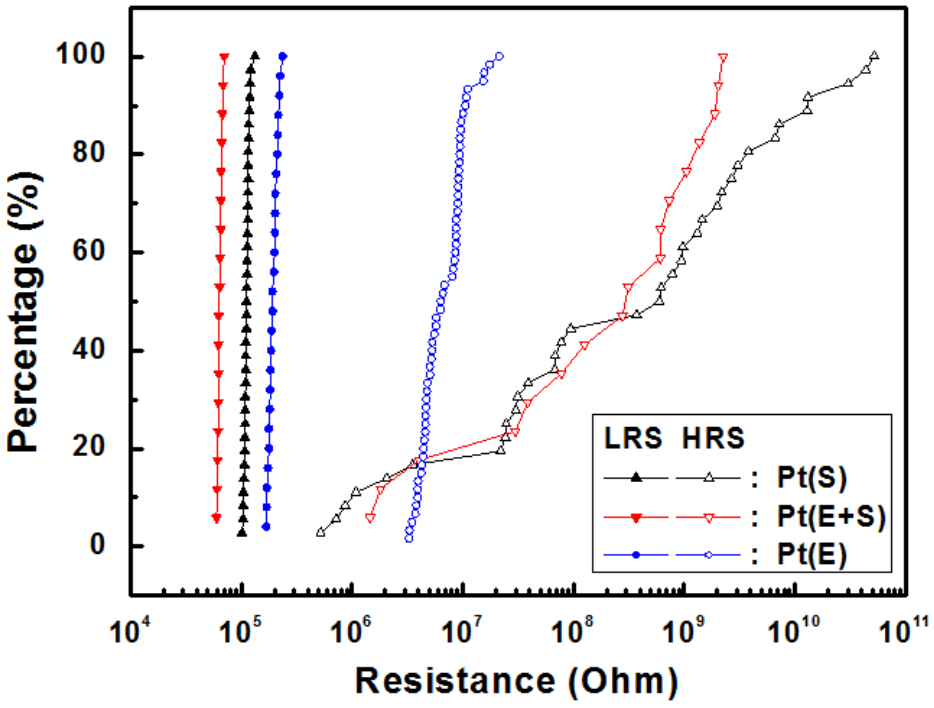

Fig. 3-32 High (empty) and low (solid) resistance value distribution of Pt(S)/HfO_x/TiN (upward-triangle, black), Pt(E50+S)/HfO_x/TiN (downward-triangle, red), and Pt(E150+S)/HfO_x/TiN device (circle, blue).

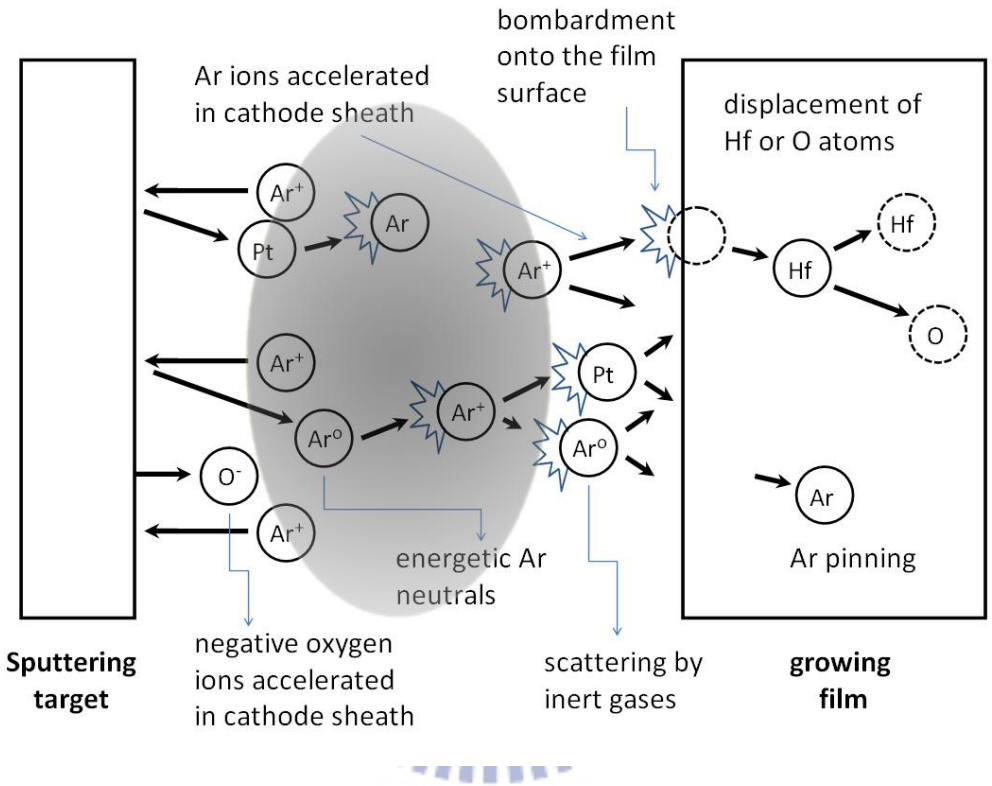

Fig. 3-33 Schematic illustration of the generation and primary collision process of the sputtered particles (Ar^+, Ar^o, O^-) in the sputtered-deposited films. After, energetic incident Ar ions are neutralized and reflected at the cathode (target) surface where they collide with the film surface to induce film damage.

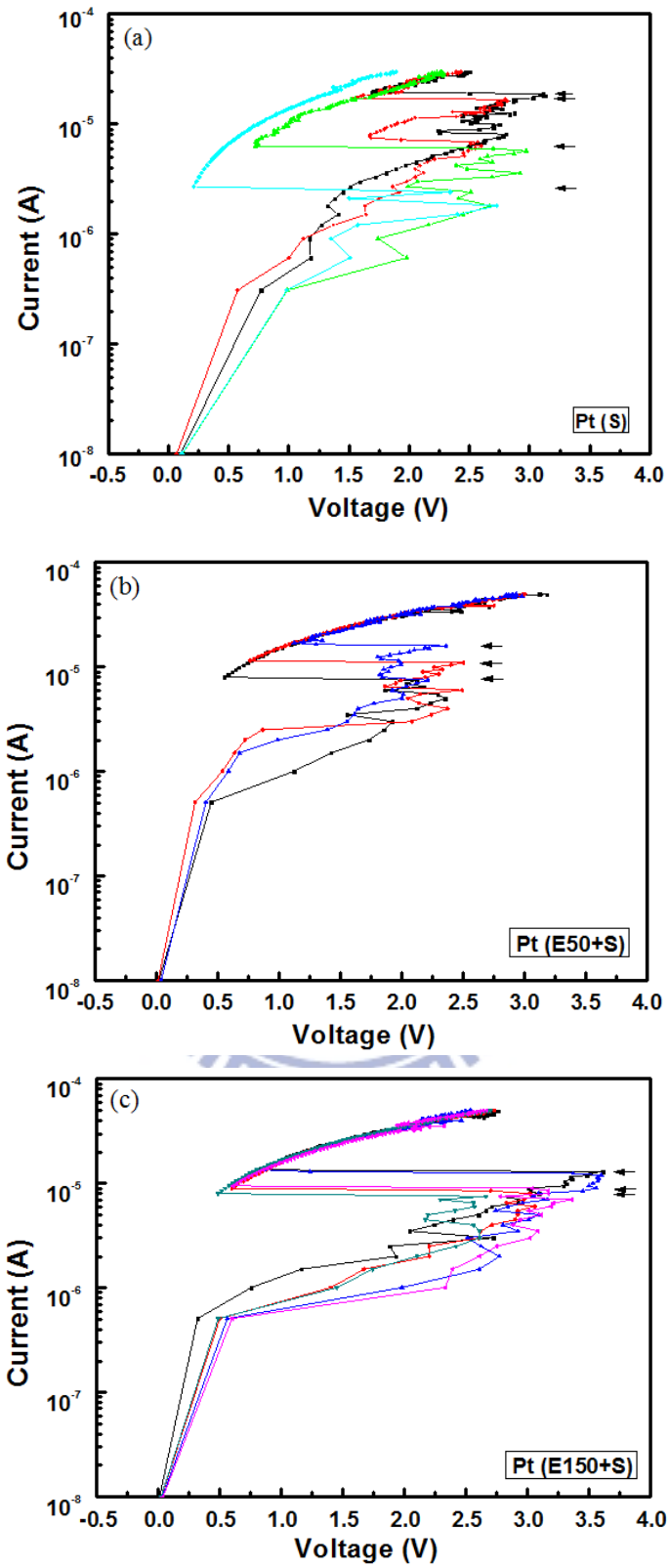

Fig. 3-34 Typical I-V curves of several consecutive sweeping cycles under current-mode operation of (a) Pt(S)/HfO_x/TiN, (b) Pt(E50+S)/HfO_x/TiN, and (c) Pt(E150+S)/HfO_x/TiN device.

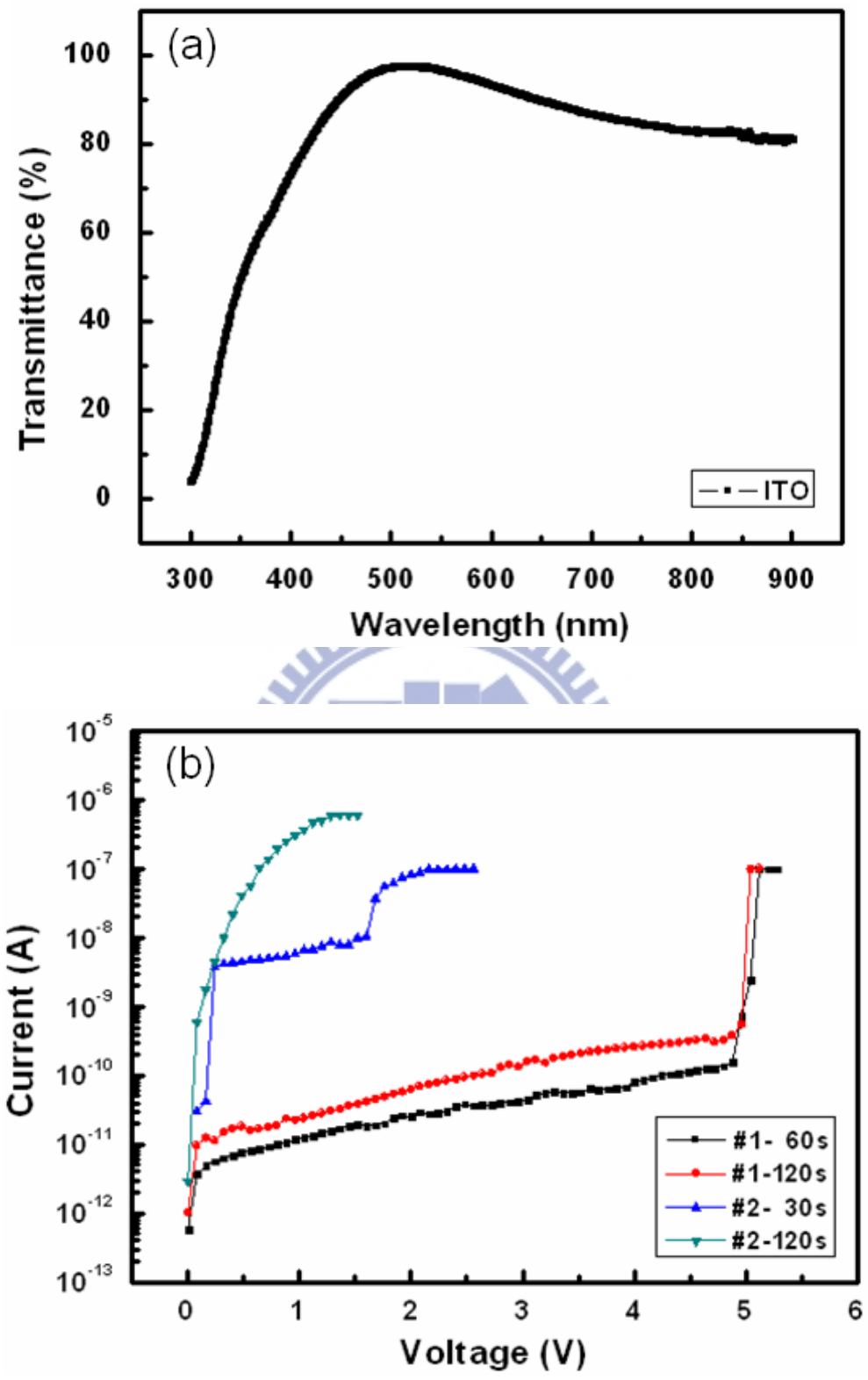

Fig. 3-35 (a) The transmittance of ITO/glass structure. (b) The I-V curves of forming process with UV light exposure, and each symbol represents different exposure condition: Untreated (square), #1-30s (up-triangle), #1-120s (down-triangle), and #2-120s (circle), respectively.

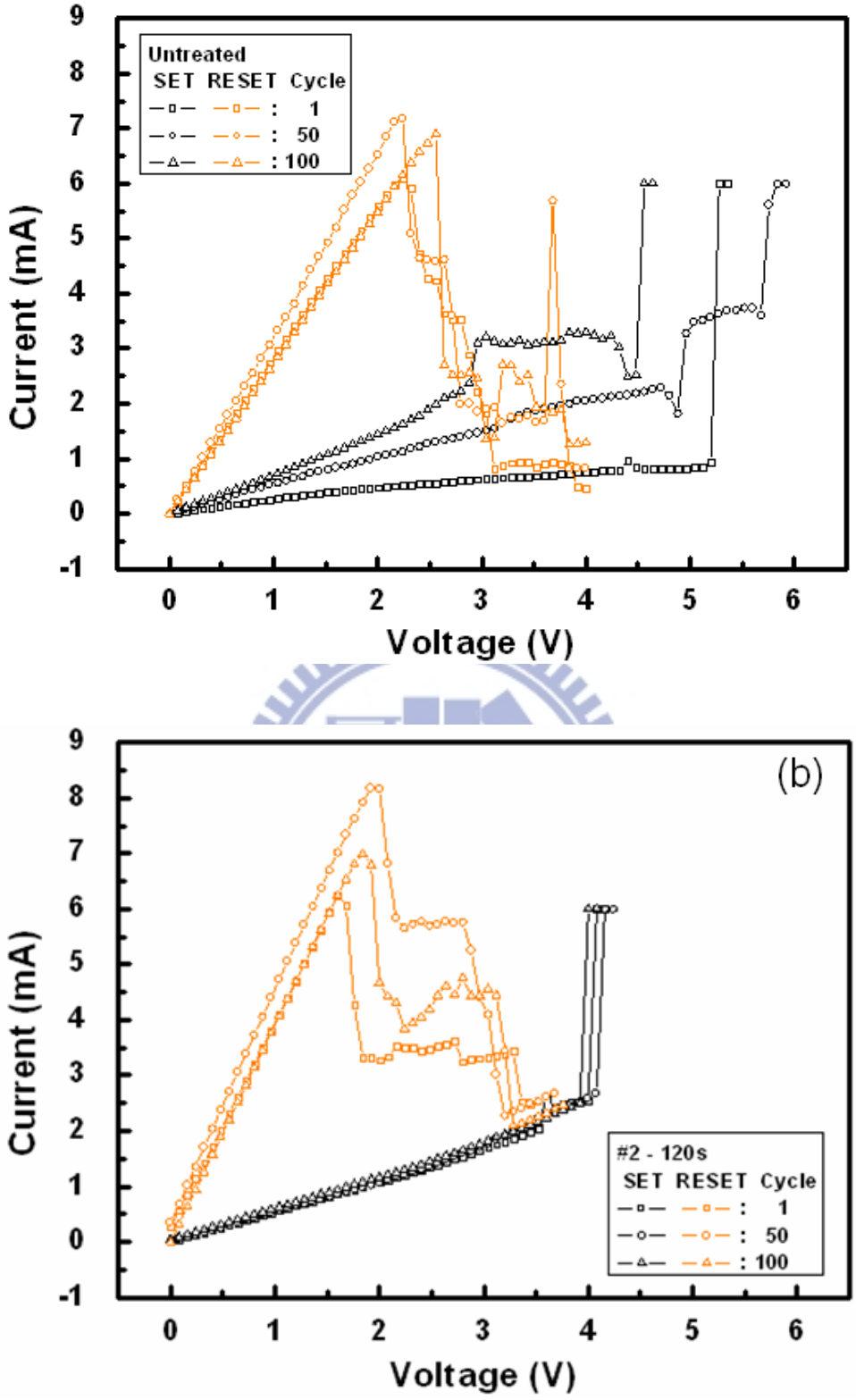

Fig. 3-36 The typical I-V characteristics of ITO/HfO_x/TiN device after applying 1st, 50th, and 100th voltage sweeping cycles of (a) untreated sample and (b) under of UV light exposure of 120s, respectively.

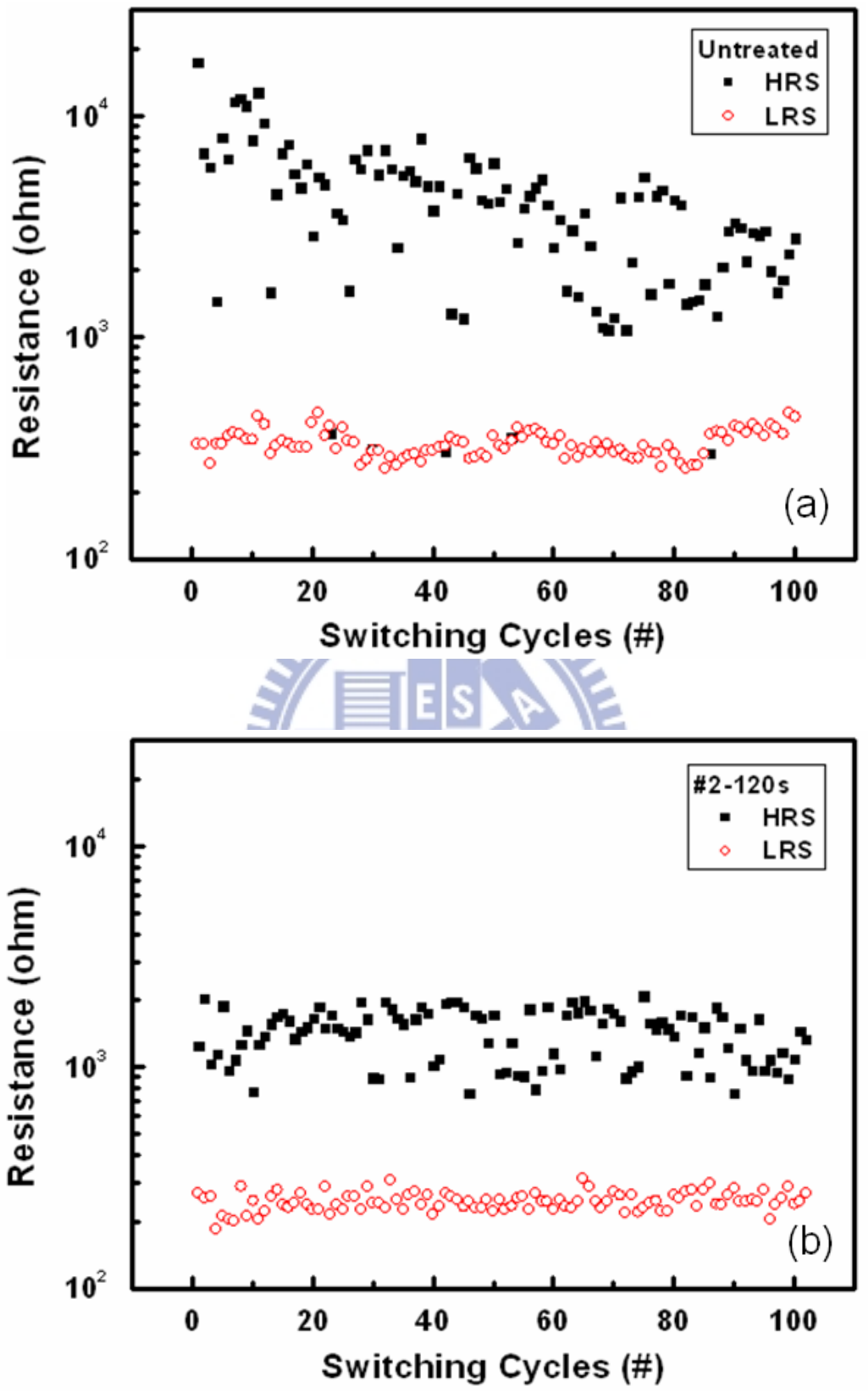

Fig. 3-37 Reset/set cycling endurance of ITO/HfO_x/TiN device of (a) untreated, and (b) under UV light exposure of 120 seconds (#2-120s), respectively.

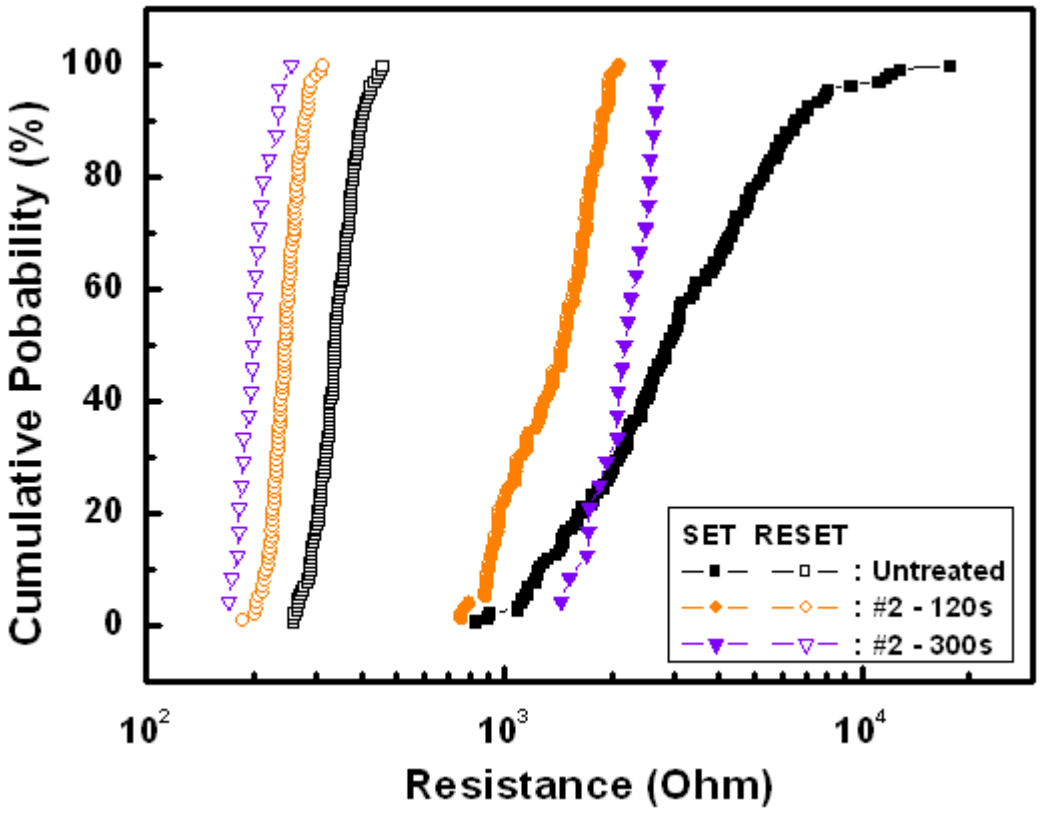

Fig. 3-38 Resistance distribution of HRS (solid) and LRS (empty) for ITO/HfO_x/TiN device of untreated (square), under UV light exposure for 120 (circle), and 300 seconds (down triangle).

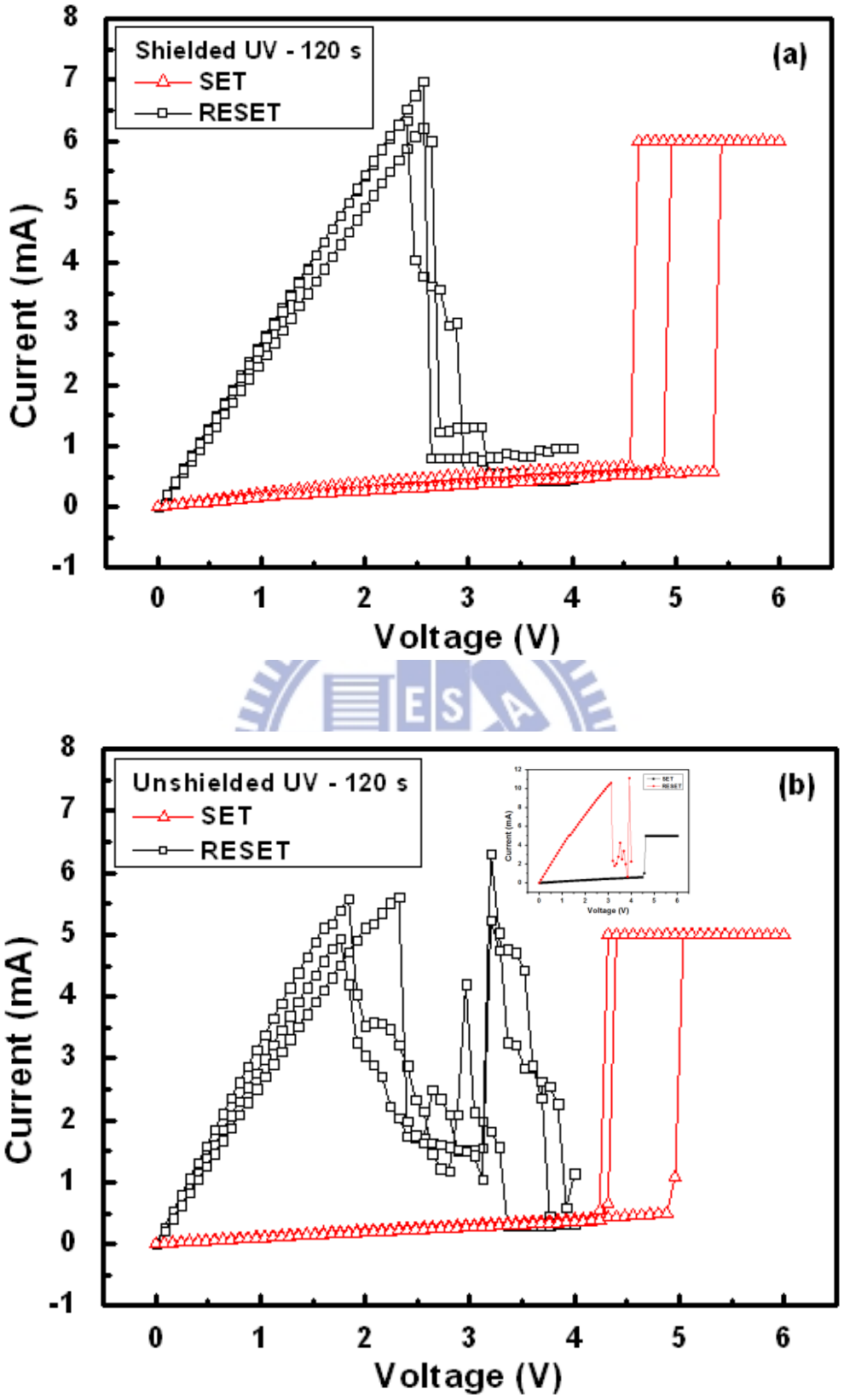

Fig. 3-39 (a) The I-V curves of Shielded UV-120 s device. (b) The I-V curves of Unshielded UV-120 s device.

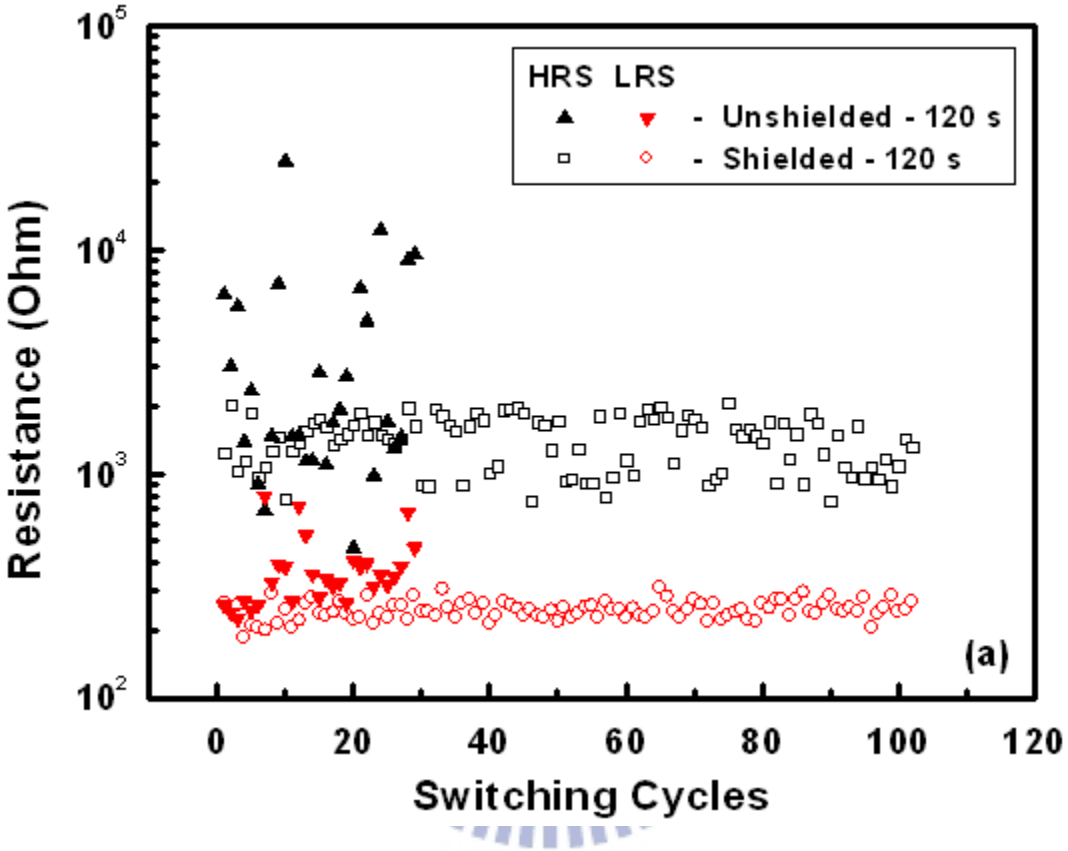

Fig. 3-40 Evolution of high and low resistance state during sequent voltage sweeping of Shielded UV-120 s and Unshielded UV-120 s samples.

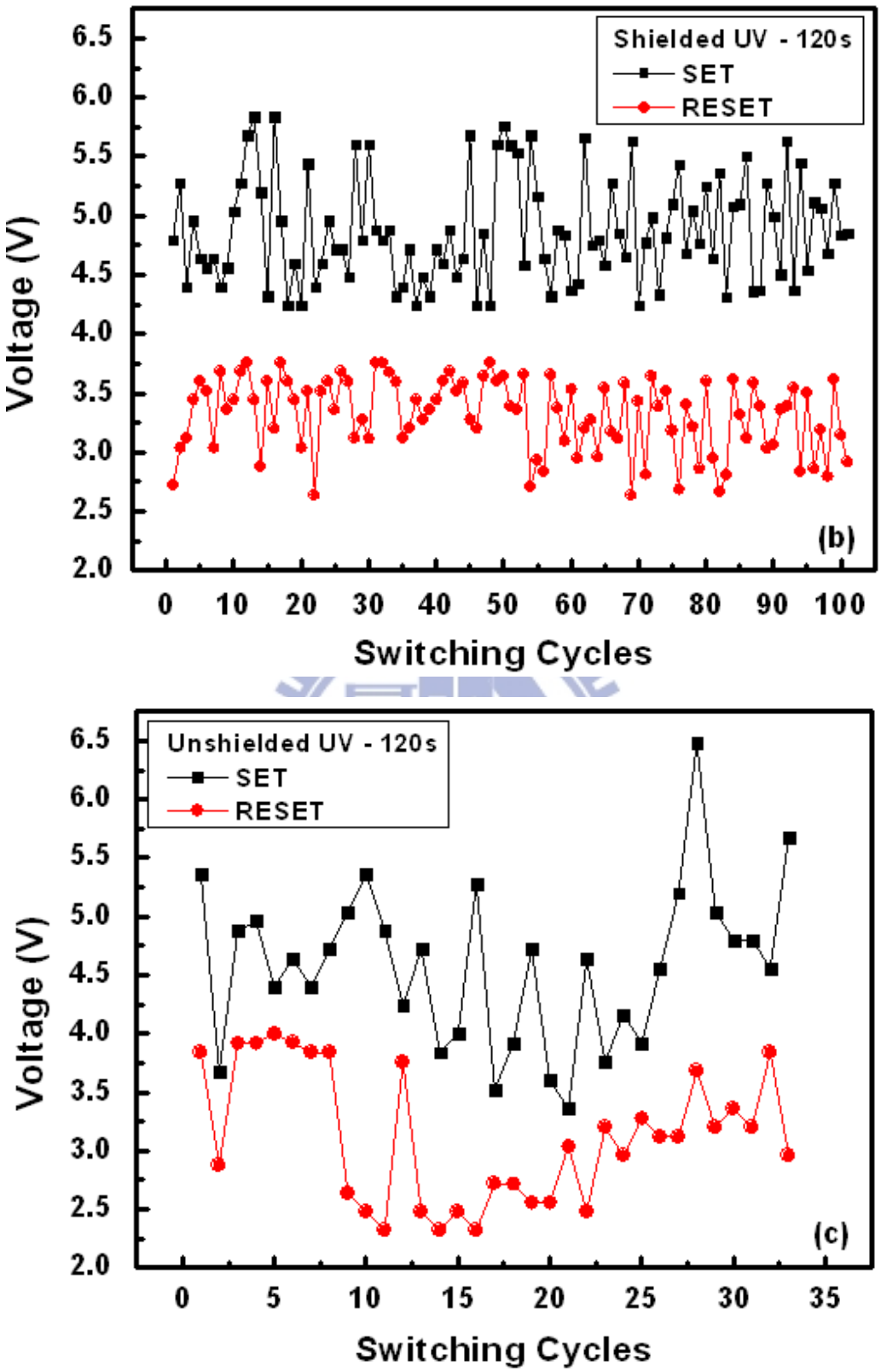

Fig. 3-41 Distribution of SET and RESET voltages versus switching cycles of (a) the Shielded UV-120 s devices, and (b) the Unshielded UV-120 s devices.

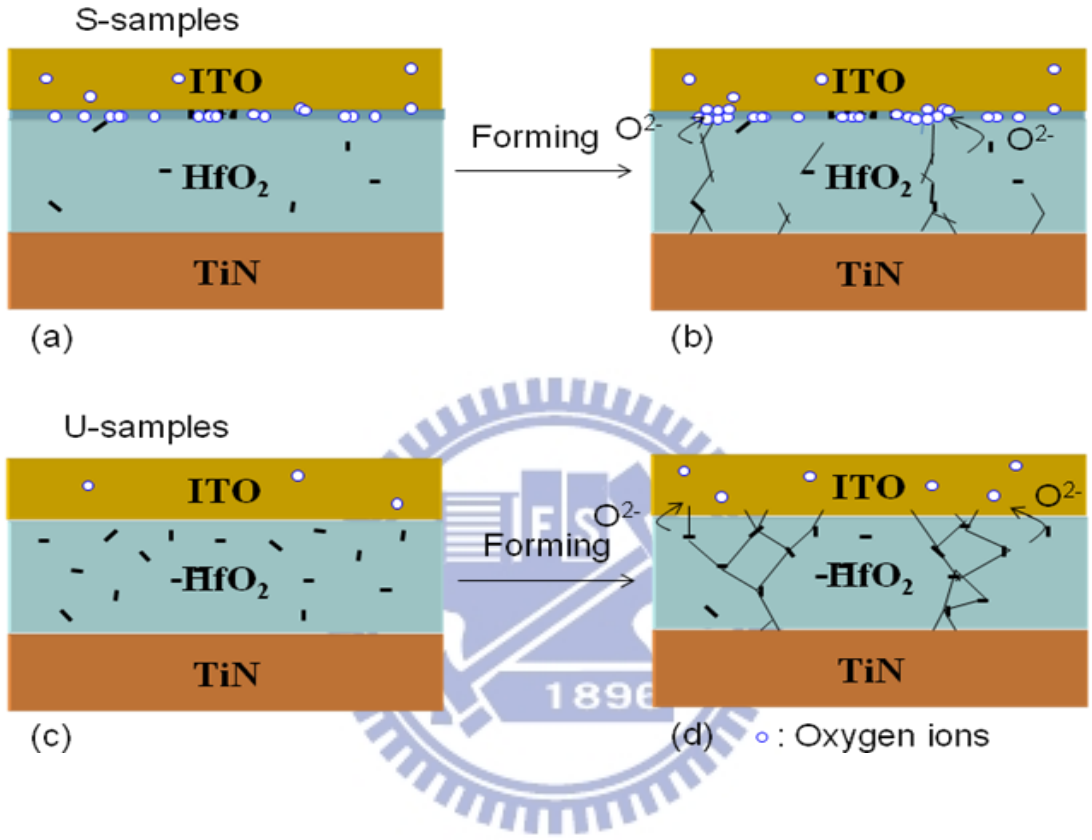

Fig. 3-42 Schematic diagrams show Shielded UV-120 s samples (a) after UV light exposure and (b) filament formation, and Unshielded UV-120 s samples (c) after UV light exposure and (d) filament formation.

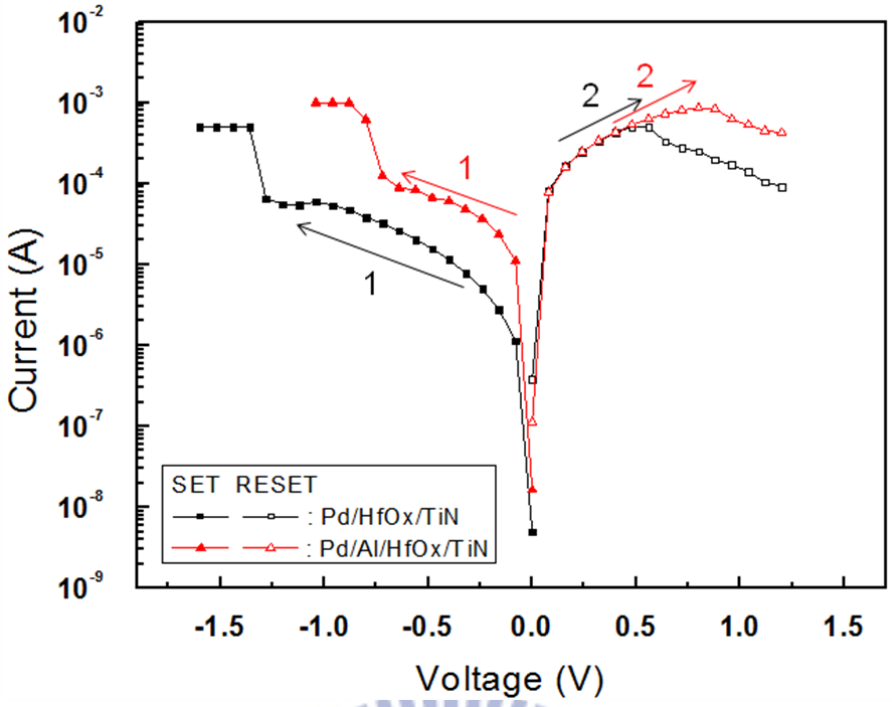

Fig. 3-43 The switching behaviors of the Pd/HfO_x/TiN and Pd/Al/HfO_x/TiN structure operated by negative bias for SET and positive one for RESET.

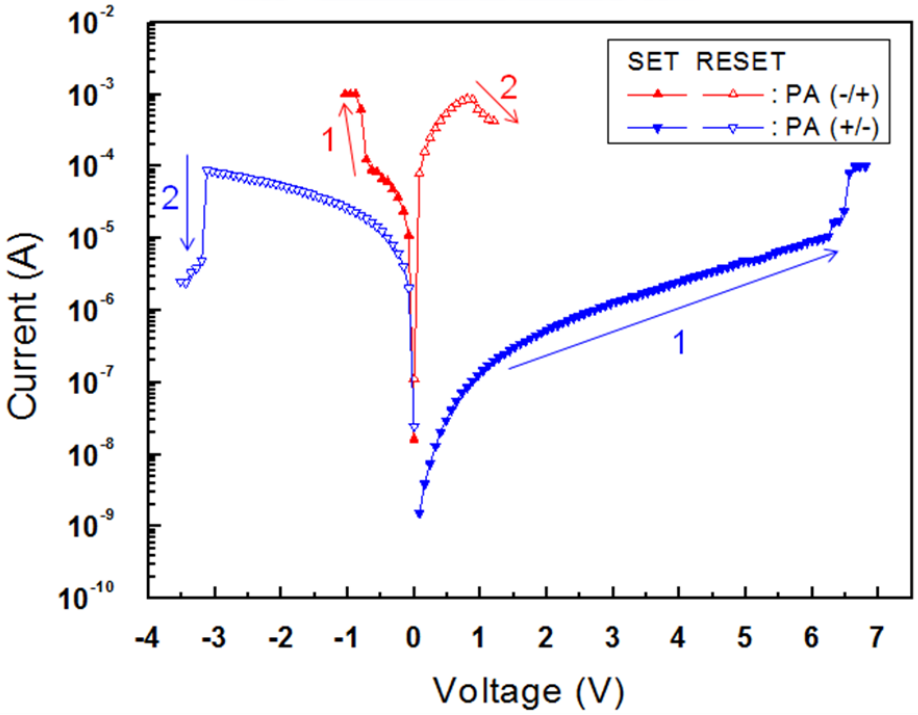

Fig. 3-44 The switching behaviors of the Pd/HfO_x/TiN structure operated by negative bias for SET and positive one for RESET (up-triangle) and positive for SET and negative for RESET (down-triangle).

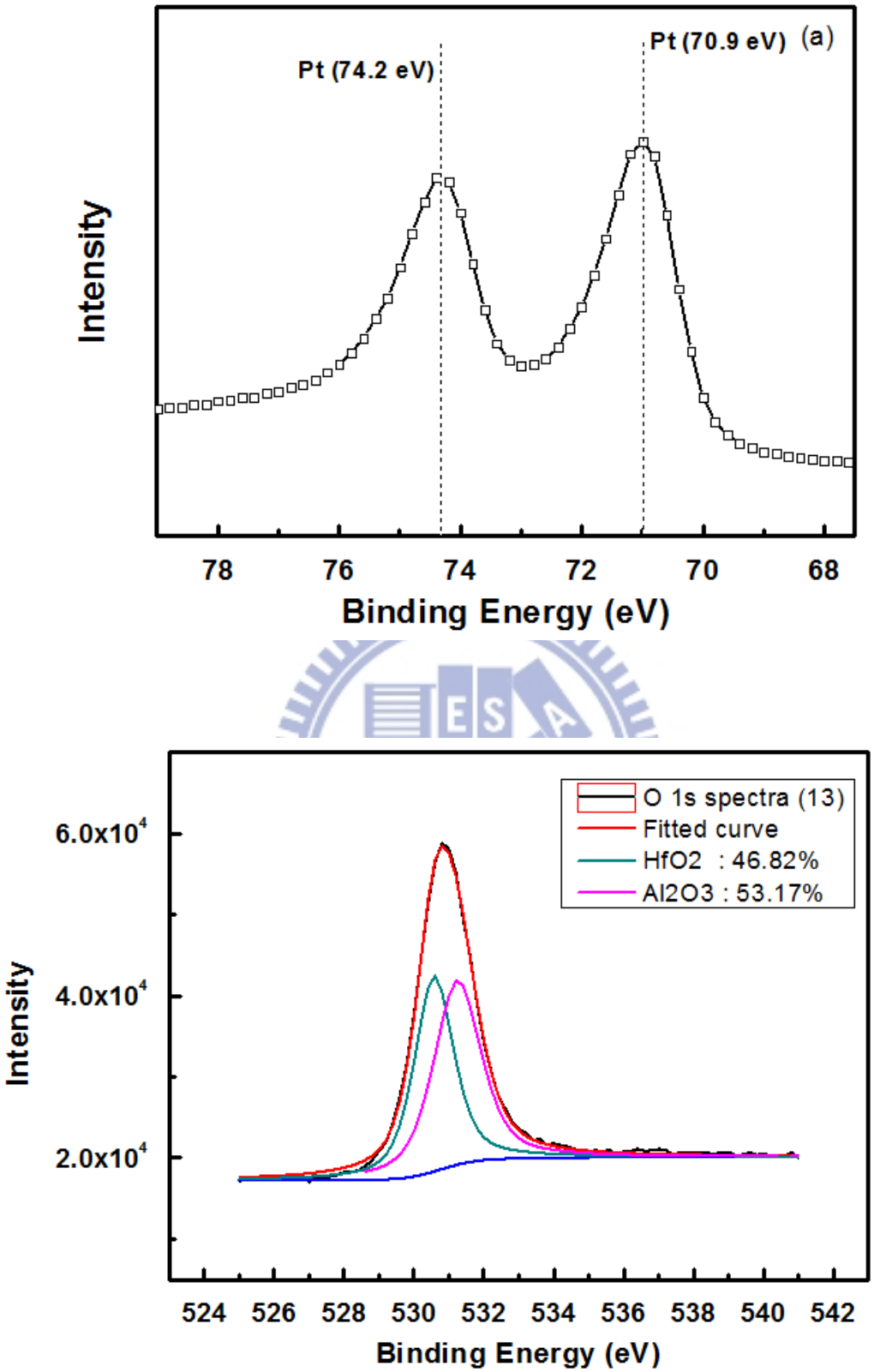

Fig. 3-45 XPS core level spectra of (a) Pt 4f and (c) Al 2p at the interface region.

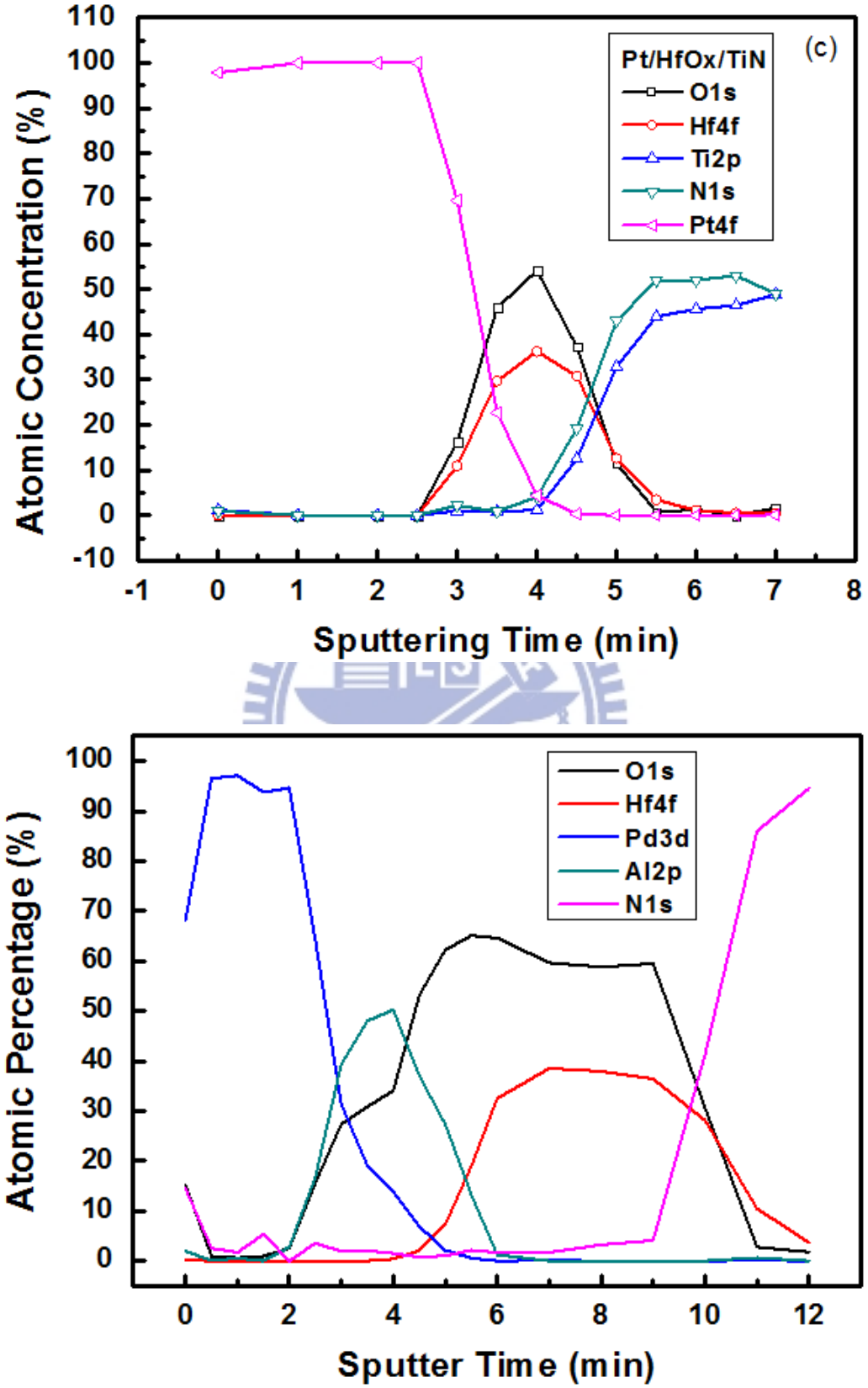

Fig. 3-45 AES depth profile of (b) $Pt/HfO_x/TiN$ and (d) $Ti/HfO_x/TiN$ structure.

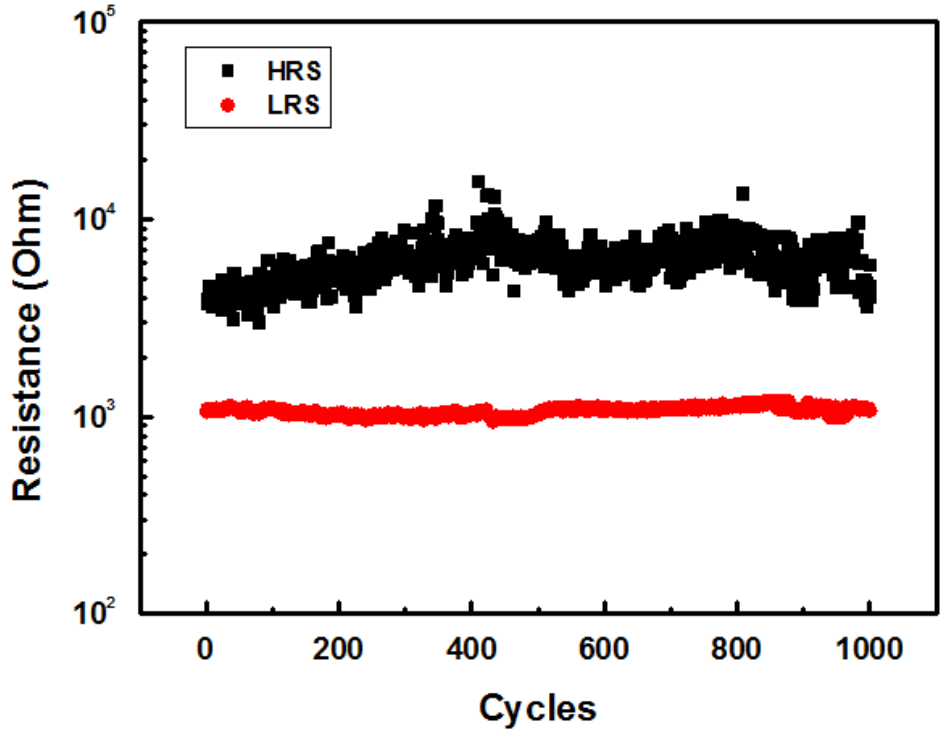

Fig. 3-46 Evolution of ON-state and OFF-state during sequent voltage sweeping

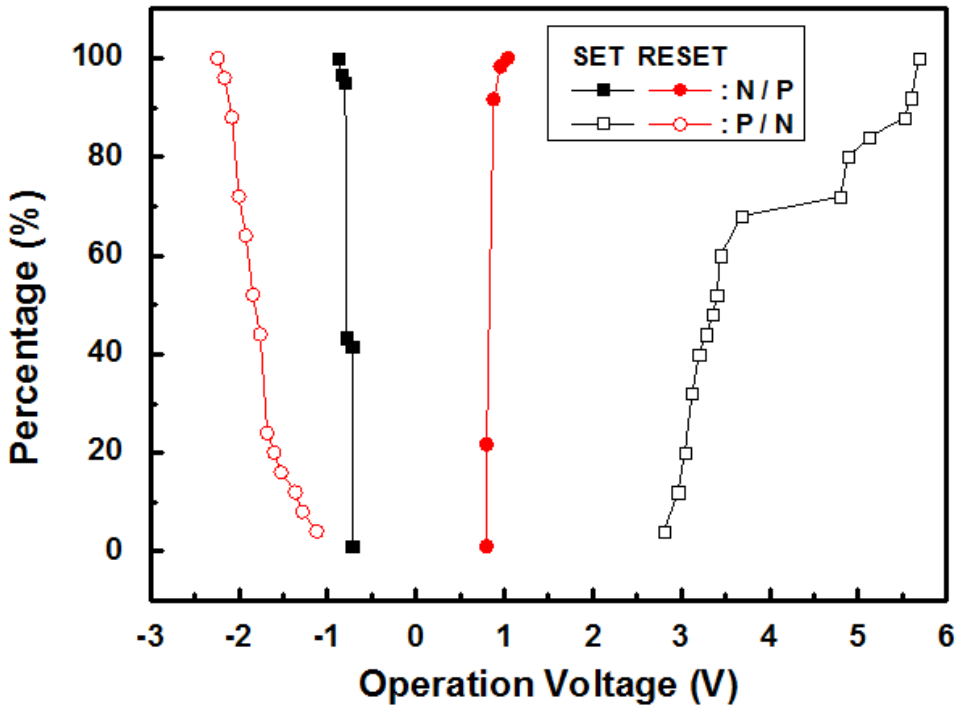

Fig. 3-47 Distribution of the SET and RESET voltage in Pd/Al/HfO_x/TiN devices under the two polarity of resistive switching operation.

Chapter 4 Results and discussion of the resistive switching properties in the Gd_2O_3-based memory devices

4.1 Introduction

Resistive states were first observed in the 1960s. Nevertheless, the reversible RS behaviors triggered by applied electric field have been extensively investigated for use as resistive random access memory (RRAM) in recent years. RRAM offers low power operation, fast switching, possibility of high-density integration, and CMOS compatibility, and it is one of the promising candidate materials for NVM [1]. Among the various candidate materials for RRAM devices, binary transition metal oxide such as NiO, TiO_2, ZrO_2, and ZnO, have been reported to demonstrate the reversible switching characteristics [2-5], but the detail switching mechanism are still debate. Evaluating other oxide materials is essential for a universal understanding of the switching mechanism of RRAM devices. The rare-earth oxide, Gd_2O_3, is very attractive for high-k application due to its large bandgap (5.6 eV), high dielectric constant (k=16), and higher thermodynamic stability. However, the application of Gd_2O_3 film for RRAM devices lacks thorough investigated. For rare-earth oxides, the CeO_2 [6,7] and Gd_2O_3 [8] films have been found to have reversible RS characteristics, demonstrating the relationship between oxide crystallinity and electrical properties. As for CeO_2, Lin et al. [6] have investigated the reversible RS behaviors of a sputtered CeO_2 thin film in a Pt/CeO_2/Pt device, and proposed that the switching mechanism is attributed to the formation and rupture of the conducting filaments by the redox reaction of the inner CeO_{2-x} and CeO_2. Cao et al. [8] investigated forming-free Gd_2O_3 films for memristor application. The authors reported that a resistance ratio from HRS to LRS of about six to seven orders of magnitude was achieved at a bias voltage of 0.6 V. However, the deposition temperature of their

Gd_2O_3 film was up to 730 °C during pulse laser deposition, which was not under the demand of the back-end fabrication process. The switching characteristic of Gd_2O_3 films fabricated at low temperature is still unknown and must be investigated further. In the next section, we investigate the reproducible and stable RS phenomenon, high to low resistance ratio, endurance, temperature effect, and switching parameters based on a Ti/Gd_2O_3/Pt device. In addition, we report the successful fabrication of a Gd_2O_3-based T-RRAM device and examine its electrical characteristics. Its RS properties, endurance, retention and switching mechanism under unipolar and bipolar operations are studied and discussed. A possible model based on the formation and rupture of the conducting filaments is proposed to elucidate the switching mechanism of the ITO/Gd_2O_3/ITO TRRAM device.

4.2 Experimental details

4.2.1 Experimental details of the Ti/Gd_2O_3/Pt RRAM devices

A bilayer metal Pt/Ti was deposited on SiO_2 layer as a bottom electrode by e-beam evaporation. Thin metal Ti was used to enhance the adhesion of Pt electrode on the SiO_2 layer. A 250 Å-thick Gd_2O_3 thin film was then deposited on Pt/Ti/SiO_2/Si substrates at room temperature (RT) by pulse laser deposition (PLD) with oxygen pressure of 0.01 Pa using a metal Gd target. (The stoichiometric transfer of complex target materials in a single-step process is an advantage of PLD.) Finally, the bilayer electrode Pt/Ti was deposited on the Gd_2O_3 thin film as the top electrode. A shadow mask with a diameter of 200 μm was used to define contact pad for measurement.

4.2.2 Experimental details of the ITO/Gd_2O_3/ITO T-RRAM devices

For the transparent RRAM, the commercial ITO glass was used as the bottom electrode and substrate. The PLD was then adopted to deposit Gd_2O_3 using ceramic

Gd_2O_3 target as the resistive layer of the TRRAM device at RT, 200, and 300 °C. Lambda physics of excimer laser was furnished by λ=248 nm, pulse duration of 25 ns, repetition rate of 3 Hz, and the laser energy of 500 mJ. The process parameter of oxygen pressure is 10 mtorr and the thickness is controlled to 25 nm. Finally, the ITO was used as a top electrode. A 100 nm-thick ITO thin film was deposited by dc sputter system using a shadow mask with a diameter of 1200 μm. Electrical characteristics were performed using Agilent 4156C semiconductor parameter analyzer (SPA) at RT. Current flow from the top to the bottom electrode was defined as positive sweep.

4.3 Resistive switching properties of Ti/Gd_2O_3/Pt thin films

4.3.1 Nonpolar resistive switching characteristics in Ti/Gd_2O_3/Pt devices

(a) XPS analysis:

The chemical compositions of the Gd_2O_3 films before and after the forming process were both analyzed by XPS. Fig. 4-1 shows the XPS spectra of Gd 4p of the as-grown sample (initial resistance state, IRS). The peak of Gd 4p in the spectra is located as a doublet at 148.1 and 142.5 eV. It stands for only a Gd oxide peak (Gd^{3+}) at the IRS [Fig. 4-1]. In contrast, the Gd peak shifts to a lower binding energy at the LRS [Fig. 4-2], indicating the emergence of the metallic Gd peak. The XPS peak of Gd 4p could be well-fitted to the metallic Gd and oxide Gd peaks by using Lorentzian and Gaussian distributions. Cao et al. [8] previously reported that the existence of metallic Gd inside Gd_2O_3 films corresponds to a forming-free RS behavior. We believe that the pre-existence of metallic Gd defects inside the as-grown Gd_2O_3 films is highly correlated to the forming process and that a large amount of defects within the Gd_2O_3 films, including oxygen vacancies and metallic Gd defects, can be induced by the forming process. In addition, Cao et al. further claimed that the forming-free behavior of Gd_2O_3 films is closely related to its specific deposition process and

internal microstructure. The Gd_2O_3 films cannot crystallize at room temperature during the PLD process. Therefore, the forming-free RS behavior found in the study by Gao, but not found in our study, may be attributed to the high deposition temperature (730 °C) during the Gd_2O_3 film deposition. This causes crystallization of Gd_2O_3 films, which can contribute to grain growth and formation of the metallic Gd defects on the grain boundaries. These defects facilitate the formation of conducting filaments without the forming process. Lee et al. also reported similar results, wherein the existence of metallic Ni dominates NiO films which required forming [9].

(b) Forming process:

A forming process is needed at the beginning to activate the RS behavior. A dc sweep voltage from 0 V to a certain positive voltage value was applied to the device with 0.1 μA compliance current. The forming voltage ($V_{forming}$) in the Ti/Gd_2O_3/Pt film is about 3.5 V shown as arrow 1 in Fig. 4-3. The forming process is a soft breakdown of the dielectric film and corresponds to the creation of percolation paths during voltage stress. The positive voltage is swept from 0 V to certain values without compliance current, and much larger current values in the low resistance state (LRS) can be obtained. A reversible dielectric breakdown can be sometimes observed by a sudden drop on the current value appearing at a certain voltage, and the state is switched back to a high resistance state (HRS). The voltage from HRS to LRS and LRS to HRS is defined as set voltage (V_{set}) and reset voltage (V_{reset}), and the values of V_{set} and V_{reset} are about 2.5 V and 1.2 V, respectively. The typical unipolar I-V curves and the operation sequence is shown as arrows 2 and 3 in Fig. 4-3. This result is different from the previous reports on the Pt/Gd_2O_3/Pt RRAM structure wherein the authors claim that their Gd_2O_3 devices have a forming-free function [8]. Their Gd_2O_3 film was deposited at a temperature of 730 °C, which is much higher than ours (RT).

High deposition temperature can form several polycrystalline structures with cubic and monoclinic composite phases inside Gd_2O_3 film in their devices, but this phenomenon does not occur in low-temperature fabricated device.

(c) Asymmetric unipolar resistive switching:

Interestingly, after the forming process, the reversible resistive switching can also be performed under negative bias, shown as arrows (2) and (3) on the left side of Fig. 4-3. A sudden drop on the current values occurred at -1.6 V, and the state switched to another HRS. By applying a negative bias again, the HRS can be switched back to LRS, similar to the switching behavior shown in the positive side. An asymmetry of the I-V curves under the two polarity operation was clearly observed. We propose that this factor is attributed to the asymmetry of our MIM structure (Ti and Pt were used as top and bottom electrode, respectively).

To confirm further that the behavior observed was not an accidental event, the repetitive resistive switching was tested. As shown in Figs. 4-4 and 4-5, the resistive switching I-V curves from HRS to LRS and from LRS to HRS in three cycles can be both obtained repetitively by applying the positive or negative bias to the device. Two resistance states at the same bias polarity can be distinguished without overlap. The electrical characteristics under the positive operation are much more stable than those under the negative one. Furthermore, the V_{set} values under the negative operation (|-11| V) are much higher than those at the positive side (2.5 V), even though there is a distribution of V_{set} values under both positive and negative operations. On the contrary, the V_{reset} exhibits no distinct dependence on the polarity. Fig 4-6 shows the resistance values versus switching cycles under the positive operation. The resistance values were obtained at 0.3 V in each dc sweep. During the repetitive switching cycles, the high to low resistance ratio was observed to be larger than one order of

magnitude in positively operated devices, while it was larger than four orders of magnitude in the negative ones (not shown here). Fig. 4-7 compares the accumulative percentage versus operation voltage of the positively and negatively operated devices. Large distributions on resistance values are clearly observed under the negative operation. The average switching value of V_{set}, V_{reset}, resistance values of HRS (R_h) and LRS (R_l) state at 0.3 V is about 1.67 V, 0.63 V, 60 KΩ, and 150 Ω for the positive operated devices, and -9.78 V, -2.46 V, 8.8 GΩ, and 57 Ω for the negative ones, respectively. Distinct switching characteristics on the two operation polarities are observed from the collected data shown above. Several factors have been proposed to influence the switching parameters, such as forming process, electrode material, operating type, deposition process and condition, crystallinity, and treatment condition of TMO material. As our Ti/Gd_2O_3/Pt samples are performed under the same fabrication process and measurement system, the difference in electrode material may be dominant key points in causing the asymmetry of switching properties.

(d) Possible switching mechanism:

Based on the proposed unipolar switching mechanism, the formation and rupture of the conducting filamentary paths may be most suitable for the switching mechanism of the Ti/Gd_2O_3/Pt device. Anode electrode plays an important role during switching, and it greatly dominates the switching characteristics [10,11]. Ti electrode is the anode under a positive operation, while Pt metal is the anode under a negative one. Ti is a reactive metal and has a low Gibbs free energy to oxygen compared with the noble metal Pt, which effectively modulates the migration of oxygen ions during resistive switching. Ti serves as an oxygen reservoir to preserve oxygen ions as it has many multiple valance states [12]. From the X-ray photoemission spectroscopy (XPS) shown in Fig. 4-8, the main peak shifts from 454.1 eV (main peak of Ti spectra) to a

higher binding energy, clearly showing that the oxidation occurs at the Ti/Gd_2O_3 interface. During the SET process, once oxygen ions are extracted to the Ti anode, the oxygen ions can be confined near the conducting filamentary paths by oxidizing with the reactive Ti, while the Pt anode cannot, as shown in Figs. 4-9 (a) and (c). The non-oxidizing property of Pt guarantees the easy movement of oxygen ions or atoms along the grain boundaries to the atmosphere, and it possesses the random distribution of oxygen ions for the fluctuant switching behaviors. During the RESET process, some of the oxygen ions inside the Ti metal can effectively go back to re-oxidizing the Gd metal, making the RS more stable than the Pt anode shown in Figs. 4-9 (b) and (d). Because the distribution of the oxygen ions greatly dominates the stability of the switching parameters [10,13], this may cause the difference in the switching properties between positive and negative bias operations, as shown in Fig. 4-7. Based on the discussion above, we further confirm that the different electrical properties between positive and negative operations are mainly attributed to the distinction of the anode metal.

4.3.2 Conduction mechanisms in Ti/Gd_2O_3/Pt devices

In order to understand the conduction behavior and resistive switching mechanism of the Ti/Gd_2O_3/Pt device, the HRS and LRS of the I-V curves were analyzed according to different conduction mechanisms. Based on the ln (I)-ln (V) plot in Fig. 4-10, a slope close to 1 in the LRS indicates that the conduction mechanism has an ohmic behavior (inset of Fig. 4-10). We surmise that the LRS conduction of the device may be explained by the filamentary conduction model. In contrast, the experimental I-V curve in the HRS shows a nonlinear slope, indicating a different conducting behavior. Ohmic conduction is observed to be dominant in the low voltage region to 0.24 V (Fig. 4-10). However, the conduction behavior in the

applied voltage region of 0.24-1.44 V shows a linear relation with a slope of about 2, which corresponds to trap-related space charge-limited conduction (SCLC).

Based on the above discussion, a possible switching mechanism of the Ti/Gd_2O_3/Pt capacitor under unipolar operation is proposed. During the initial forming process using a positive bias, the conducting paths, which consisted of oxygen vacancies and metallic defects, are generated in the Gd_2O_3 thin film. Therefore, the state after the forming process switched to a LRS, and the coexistence of the metallic and oxide Gd peaks can be observed from the XPS analysis [Fig. 4-2]. When a positive electric field is repeatedly applied to the top electrode, a large current flowing through the conducting filaments causes thermal rupture of the filaments. Consequently, the state switches from LRS to HRS. Thus, the formation and rupture of the conducting filaments, triggered by the electric field and joule heating effect, is responsible for the switching mechanism of the Ti/Gd_2O_3/Pt devices.

4.4 Resistive switching properties of ITO/Gd_2O_3/ITO T-RRAM devices

In this section, we investigate the deposition temperature effect on the unipolar and bipolar resistive switching characteristics. The surface morphology, crystallinity, grain size, reaction with underlying layer, etc. are greatly influenced by the deposition temperature. Several groups have reported that the film's deposition temperature is a key factor on the switching properties. Kim et al. reported that the resistance ratio of HRS and LRS increased with increasing the substrate temperature, owing to increasing the crystallinity under 700 °C than that of 500 °C. M. Fujimoto et al. also proposed that PCMO thin films properties were depended mainly on the PCMO deposition temperature. However, they further mention that resistivity of the Pt/PCMO/Pt is a key issue for a stable resistive switching behaviors, which depends

greatly on the deposition temperature. It is considerably important to understand the substrate temperature effect that directly influence the growth mode in order to be able to control the types and density of defects that are formed during PLD process. This will ultimately determine the thin film orientation and microstructure, film morphology, and film properties. Therefore, we investigated the resistive switching characteristics by changing the growth temperature of Gd_2O_3 films to modify Gd_2O_3 thin films properties.

4.4.1 Thin film properties of the ITO/Gd_2O_3/ITO T-RRAM devices

Fig. 4-11 shows the crystallinity of ITO/Gd_2O_3/ITO devices where the Gd_2O_3 films were deposited at 25 °C (G-25), 200 °C (G-200), and 300 °C (G-300) by using X-ray diffraction (XRD) analysis. From this figure, the Gd_2O_3 films are found to be crystallized when the substrate temperature was over 200 °C, as clearly shown in the enlarged figure (Fig. 4-12). Only (400) peak of the Gd_2O_3 film is observed, indicating that the Gd_2O_3 films were grown with a (400)-perferred orientation on ITO/glass substrate. The crystallinity of the Gd_2O_3 films are enhanced with increasing the substrate temperature [14]. Furthermore, the top view of the G-25, G-200 and G-300 samples were investigated by scanning electron microscopy (SEM) as shown in Fig. 4-13 ~ Fig. 4-15, respectively. The G-300 samples in Fig. 4-14 exhibit more apparent crystalline shapes than that of G-25 ones, which is consistent with the observed XRD data shown in Fig. 4-12. The micro-crystalline structure composed of defects, dislocations, and grain boundaries inside Gd_2O_3 films, which inevitably plays an important role on resistive switching behaviors [8]. The high resolution transmission electron microscopy (HR-TEM) image of G-25, G-200 and G-300 samples are shown in Fig. 4-16 ~ 4-17, respectively. The samples with polycrystalline structure often exhibit resistive switching including defects and oxygen vacancies, which can easily

facilitate oxygen ions migration under an applied voltage and form conducting filaments. Thus, the resistive switching phenomenon is observed in the polycrystalline structure. Fig. 4-18 compares the transmittance of ITO/Gd_2O_3/ITO devices under different growth temperature. The logo under the transparent device can be seen clearly owing to the transparent ITO, Gd_2O_3, and glass substrate, as shown in Fig. 4-19. Distinction on the transmittance of the three samples was attributed to the distinction on the structural composition.

In considering the fundamental theory of film nucleation and growth and how this theory applies to the PLD technique, as recently reviewed by Greene, we can separate the discussion into the three conventional modes of film nucleation and growth, including (1) three-dimensional island growth (Volmer-Weber), (2) two-dimensional full-monolayer growth (Frank-van der Merwe), and (3) two-dimensional growth of full monolayers followed by nucleation and growth of three-dimensional islands (Stranski-Krastinov). Depending on the thermodynamics relating the resistive film and substrate surface energies and film-substrate interface energy, one of these growth modes can be followed during thin film growth. Once the cohesive energy of the film atoms is greater than the cohesive binding between the film and substrate atoms, then the Volmer-Weber growth (island growth) tends to occur and result in the formation and growth of isolated islands. On the contrary, if the cohesive energy between the film and substrate atoms is larger than the film itself, Frank-Van der Merwe growth (layer-by-layer growth) would prefer and consists of deposition of one monolayer at a time and results in a very smooth film. According to Greene's review, a cluster that is large enough to be treated as a continuous solid, the free energy can be given as:

$$\Delta G = a_1 r^2 \Gamma_{c-v} + a_2 r^2 \Gamma_{s-c} - a_2 r^2 \Gamma_{s-v} + a_3 r^3 \Delta G_v \qquad (4\text{-}1)$$

where r is the radius of the cluster, Γ's are the interface energies, $\triangle G_v$ is the change in volume free energy on condensation of the cluster, and the a's are constants that depend on the shape of the nuclei. The subscripts c,s, and v refer to the cluster, the substrate, and the vapor, respectively. The volume free energy per unit volume of the cluster can be written as:

$$\Delta G = -\frac{kT}{\Omega}\ln\left(\frac{P}{P_e}\right) = -\frac{kT}{\Omega}\ln(\zeta) \tag{4-2}$$

where P is the pressure of the arriving atoms, P_e is the equilibrium vapor pressure of the film atoms, k is Boltzmann's constant, T is the absolute temperature, Ω is the atomic volume of the film atoms, and ζ is the supersaturation. The expression neglects the exchange of atoms between a cluster and the substrate surface, but only for the free condensation of a cluster from a vapor. Both increased atom deposition rate and reduced substrate temperature will increase the supersaturation, thus the volume free energy will become more negative. However, the contribution of the supersaturation term was inside the natural-logarithmic, so, the substrate temperature may directly affect the volume free energy ΔG more. The free-energy barrier for nucleation is given as follows:

$$\Delta G^* = \frac{4\left(a_1\Gamma_{c-v} + a_2\Gamma_{s-c} - a_2\Gamma_{s-v}\right)^3}{27\left(a_3\Delta G_v\right)^2} \tag{4-3}$$

and the nucleation rate as:

Jc = (Arrival rate of atoms at critical-size nucleus) × (Concentration of critical nuclei)

The atom arrival rate is proportional to the concentration of the mobile atoms on the surface and to the surface diffusion coefficient. The concentration of critical nuclei will be proportional to the quantity $\sim \exp\left(\frac{-\Delta G^*}{kT}\right)$

From the above mathematics, we can draw a correlation between the several parameters. With substrate temperature increases, a decrease in the net surface/interface free energy or the volume free energy shifts to more negative will produce a decrease in the critical size, causing a decrease in the total free-energy barrier needed for cluster nucleation, and an increase in the cluster nucleation rate. An increase of substrate temperature during PLD process would increase the surface diffusion coefficient of the adsorbed vapor atoms, thus, the atom arrival rate will be increased. The concentration of critical nuclei is also increased as the temperature increases, since it is proportional to the temperature. It can also shifts the volume free energy to more negative values and lower the free-energy barrier for nucleation, thus a more crystalline surface will be obtained. A model for film morphology was given by Grovenor et al. derived from experiments on films grown in high vacuum. They proposed that the film morphology would as a function of substrate temperature, $T_h=T/T_m$, where T is the temperature of the substrate and T_m is the melting temperature in K. As the substrate temperature increases, the T_h value tends to shift toward the larger value, which means that there is larger surface energy for the surface atoms to diffuse and migrate during film deposition. The preceding scenarios for the details of film nucleation and growth show that film growth is highly dependent on material parameters and deposition conditions. This could be used to explain why the samples have larger grain size and stronger crystallinity when samples are deposited at high temperature.

4.4.2 Bipolar resistive switching characteristics in ITO/Gd_2O_3/ITO T-RRAM devices

(a) Resistive switching characteristics:

The typical bipolar I-V characteristics of the ITO/Gd_2O_3/ITO devices are shown

in Fig. 4-20. As can be seen in Fig. 4-20, three devices all exhibit a bipolar resistive switching behavior, and the resistance switching from the ON to OFF state can only be realized under positive voltages, indicating the switching properties are voltage polarity dependent. The switching from OFF to On and ON to OFF exhibits only a gradual change on G-25 samples, while a great abrupt change is clearly observed on G-300 ones. To evaluate the memory performance of the ITO/Gd_2O_3/ITO device, the endurance characteristics were measured. Fig. 4-21 compares the endurance characteristic of the three cells and the device was measured in the voltage list sweep mode by performing a series of consecutive set/read/reset/read cycles. The RT deposited devices exhibit the short-lived switching properties and switching-failure among the several times of switching cycles, while the resistance values in both states become stable with the deposition temperature at the bias voltage of 0.1 V are ~14.5 and 27 for the G-200 and G-300 films, respectively. From the above measured data, the different deposited temperature of Gd_2O_3 film, which may be correspondent to different Gd_2O_3 film's microstructure observed from XRD and TEM image, revealing the correlation between microstructure and the I-V curves, resistive switching, endurance, and resistance ratio. Among various oxide materials, the relation between oxide film's microstructure and switching properties have been reported, such as oxygen partial pressure during deposition in NiO film [9], thickness in ZnO films [15], annealing effect in Al_2O_3 films [16], doping effect in ZrO_2 films [17] and deposition temperature in PCMO films [18]. In this study, we focus the topic on deposition temperature during Gd_2O_3 film deposition. The temperature effect during oxide films deposition have been investigated in NiO [19] and PCMO [18] thin films. Lee et al. investigated the switching characteristics of epitaxial NiO films grown on SrRuO3 films at 25 °C (NiO-RT) and 500 °C (NiO-500). The crystallite size of epitaxial NiO is more than thrice that of NiO grown at RT by XRD analysis, so, the density of the

grain boundaries in NiO grown at RT is expected to be higher than that in NiO grown at 500 °C. This result in a larger barrier formed between NiO-RT and the Pt top electrode reflecting an abrupt change of measured current at a voltage, while low barrier formed at NiO-500/Pt interface only exhibits gradual change [19]. Kim et al. reported that the PCMO films exhibited hysteretic I-V characteristics only when films were grown at larger than 600 °C [18]. Only crystalline PCMO films exhibited reversible switching behavior in Au/PCMO/Pt structure while noncrystalline films do not. Although the authors have made explanation on their respective devices, however, the detailed switching mechanism is quite controversial between various oxide materials. Therefore, it is essential to explore the unique characteristics on RS behaviors in view of Gd_2O_3 films.

(b) XPS analysis

Based on the above experimented data, we rationally suggest that the increase of the crystalline peak is responsible for the improvement of the switching characteristics. The XPS analysis was performed for the G-25 amd G-300 samples with all peaks referring to the C1s peak at the binding energy (BE) of 284.6 eV. As shown in Fig. 4-22 and 4-23, Gd 4d spectrum was deconvoluted into metallic state (Gd^{0+}) and oxidized state (Gd^{3+}) using Gaussian and Lorentz distribution, indicating the bulks of G-25 and G-300 films are non-fully oxidized. The metallic (Gd^{0+}) / oxidized (Gd^{3+}) composition ratio in Gd 4d spectrum was calculated to be 65.5 % / 34.5 % and 49.3 % / 50.7 % for the G-25 and G-300 samples, as shown in the inset of respective figure. The G-25 samples exhibit higher portion on the metallic states than that of G-300, which reflects higher leakage current on the as-grown samples, as shown in Fig. 4-20. The large amounts of defects in the Gd_2O_3 film, including oxygen vacancies or metal atoms, etc., may lead to the low initial resistance. The oxidized

portion inside Gd_2O_3 films increases with the temperature increases to 300 °C, which is consistent with the experimental data that the (400)-perferred orientation on Gd_2O_3 films increases. Higher deposition temperature during PLD process can make Gd_2O_3 films more densification, thus result in lower leakage current and stronger oxidized states peak on 300 °C deposited samples. Therefore, we believe that the distinction on micro-structure of Gd_2O_3 films can contribute on the RS properties, thus dominate the RS characteristics.

(c) Electrical characteristics of the 300 °C-deposited Gd_2O_3 films:

Fig. 4-24 shows the resistance values of initial resistance state (IRS), OFF state, and ON state as a function of reciprocal temperatures. It is found that the current of the IRS and HRS both exhibits positive dependence on temperature, implying the semiconductor-like behavior. The relationship between the resistance of IRS and OFFS and temperature can be well fitted to $R = R_o \exp(Ea/kT)$, where R_o is a constant independent of temperature, *k* the Boltzmann's constant, T the temperature, and Ea is the activation energy for charge carriers. The Ea for the IRS and HRS are 0.81 and 0.19 eV, respectively. Different from the HRS, the resistance values of the LRS increases with increasing temperature, which indicates the conduction mechanism is metallic like. Because the conducting paths in the LRS and HRS are mainly dominated by the metallic defects and oxygen vacancies, the preexistence of the metallic defects will have great impact on RS properties [8,9]. From previous reports by Cao et al. based on a $Pt/Gd_2O_3/Pt$ structure, they claimed that the forming-free behavior in Gd_2O_3 film is closely related to its specific deposition process and the internal microstructure [8]. The high resistance of the as-deposited film and the increased oxygen pressure during the preparation process may indicate the lower content of metallic Gd in the film, which required the forming process to realize RS

behavior. Seo et al. reported that the polycrystalline NiO films with high concentration of metallic nickel defects show bi-stable memory switching, while the films with low concentration of metallic nickel defects show mono-stable threshold switching [9]. Park et al. have found that the irreversible low resistance state facilitates further increases of Ni filaments channels and Ni filament density that resulted from the grain structure changes in the NiO_x film by simultaneous high-resolution transmission electron microscopy (HRTEM) and electron energy-loss spectroscopy (EELS) [20]. Kim et al. claimed that the resistive switching of Au/PCMO/Pt sandwich structure depends on the mixed valence state Mn^{4+}/Mn^{3+} of Mn ions in the metal/PCMO interface domains [18]. Among various oxide materials, the contents of metallic defects inside oxide film display a universal influence on RS characteristics. Therefore, adequate control on the contents of metallic defects inside oxide films is critical to determine whether the RS behavior reliable or not. For the G-25 samples, less oxidized states peak of Gd_2O_3 films reveals lower oxygen contents will involve the switching behavior, thus lead to smaller resistance ratio. The large amounts of metallic defects inside Gd_2O_3 films causes the conducting filaments hard to be ruptured from the lower oxygen contents, therefore, several times of switching failure are often observed from ON to OFF state. This phenomenon is greatly improved on the G-300 samples with lower metallic defects inside Gd_2O_3 films. More oxygen ions would be involved to trigger the RS behavior back to the semiconductor-like OFF state. Furthermore, the deposition temperature of Gd_2O_3 films under 300 °C by PLD will cause inter-diffusion between the Gd_2O_3 and bottom electrode (BE) ITO [21], which easily forms an interfacial layer (IL) in the interface to suppress the oxygen ions migration to the BE ITO. Yook et al. claimed that ITO electrode singly deposited on PPV polymer cannot induce any metal oxide formation during sputter deposition, resulting in no bistable behavior during forward and

backward scans [22]. We suggest that similar results are observed when ITO deposited on Gd_2O_3 oxide, thus the poor RS characteristics was observed at the G-25 samples, while the polarity dependent RS behaviors emerges at the G-300 one. Therefore, a more reliable RS characteristic can be obtained on the G-300 films.

In the case of memory switching, we measured the characteristic behavior of each state under various electrical and thermal environments on 300 °C-deposited samples. The dependence to size area is experimented to reveal more about the switching mechanism of the ITO/Gd_2O_3/ITO memory devices, as shown in Fig. 4-25. The current values show no dependence on size area in the LRS while decreases with size area decreases in the HRS, suggesting the presence of local conducting filaments for the present bipolar RS. We also measured the retention characteristics of both the ON state and OFF state under RT and 85 °C environment. At RT, ON and OFF state keeps its resistance value of about 100 and 3000 ohm without any change for 30000 s as shown in Fig. 4-26, while the resistance ratio margin decreases to 30% of its initial value when at 85 °C. These thermal characteristics can be explained by filled electrons existing in the deep defects level of the Gd_2O_3 band gap. Under an increased thermal energy, these electrons can be detrapped leading to decrease in ON state resistance value, thus, a much smaller retention margin will be observed. However, even after this change, the film still shows the reproducible switching behavior and recovers the initial OFF state resistance value after applying RESET voltage.

(d) Switching parameters relationship:

To further understand the corresponding relationship on operation voltage and current compliance versus resistance ratio, the detailed switching parameters are operated and tested here. In Fig 4-27, the I-V curves operated at fixed set voltage (V_{set}) of -2 V and ranging the reset voltage (V_{reset}) within 0.8 ~ 2.4 V, respectively. All the

V_{reset} in the range from 0.8 to 2.4 V all exhibit the bistable switching characteristics, and the resistance ratio increases with V_{reset} from 2 to 30 shown in Fig 4-28. Only 0.8 V of the V_{reset} is needed to perform the reset process. In addition, the measurement tests on the negative bias side are also investigated and discussed. The I-V curves operated at fixed V_{reset} of 2 V and ranging the V_{set} from -0.6 to -2.6 V, respectively, as shown in Fig 4-29. We can obtain the similar results like Fig 4-27 that the resistance ratio increases with V_{set} from 1.4 to 31.4 shown in Fig 4-30. All the V_{set} ranging from -0.6 to -2.6 V demonstrates the bistable resistive switching, and only -0.6 V is capable of switching the device to LRS. Among the above results, we further confirm that the switching mechanism mainly depend on the migration of the oxygen ions between Gd_2O_3 film and the thicker interfacial layer. The stable and reliable resistance values of HRS and LRS can be precisely modulated by the applied voltage, which implies that the Joule heating effect can be excluded during resistive switching. Furthermore, owning to the resistance values can be well controlled during operation, the multi-level states are possible to be achieved. From the results above, we believe that the Gd_2O_3 film can be a good candidate for the application on T-RRAM devices.

4.4.3 Conduction mechanisms in ITO/Gd_2O_3/ITO T-RRAM devices

To understand conduction behavior of the ITO/Gd_2O_3/ITO memory devices, the plots of *ln(|I|)* versus *ln(|V|)* of both LRS and HRS currents for the Gd_2O_3 devices are shown in Fig. 4-31. In the LRS, the conduction behavior is believed to be Ohmic conduction with a slope of linear line of 1, which is related to thermally excited electrons hopping from one trapped state to the next state. On the contrary, a completely distinct conducting mechanism was observed in the HRS region. In the HRS, the conduction behavior in the low voltage region is clearly observed to be the Ohmic conduction, which also shows a linear slope of 1. However, the *ln(|I|)* versus

ln(|V|) curves show a almost linear line with a slope of 2 in high voltage region, which corresponds to trap-related space charge limited current (SCLC).

Based on the above results, the conducting mechanism in the HRS and LRS of the ITO/Gd_2O_3/ITO memory devices can be depicted as follows. Forming process is like a soft breakdown of the dielectric film and would correspond to the percolation paths creation during the voltage stress. A large number of defects such as oxygen vacancies, metallic defects, and dislocations are generated in Gd_2O_3 film during forming process, along with oxygen ions migration toward the bottom ITO electrode. The large amounts of preexisted metallic defects inside the 25 °C-deposited samples lead to large leakage current on the IRS and OFF state. The extended defects gather together and form stronger and more conducting filaments, finally, resulting in a switch to low resistivity (LRS). At this time, conducting filaments are formed and connect the top and bottom ITO electrode, so the thermally excited carriers transport or hop through the filament path exhibiting Ohmic conduction behavior in the LRS, shown as branch 2 in Fig. 4-31. The metallic behavior on the LRS shows clear evidence that the thermally excited conducting carriers mainly mediate through the metallic Gd defects, which was formed during forming process. The Ohmic conduction can be held on as the voltage sweeping back to the positive bias (as branch 3), until a sudden drop on the current value at certain positive bias. Then, the state switched to HRS. The current with a linear dependence on voltage in branch 2 switches to a square term dependence on voltage in branch 3 at high voltage indicating that the dominant conducting mechanism changes from Ohmic conduction into SCLC conduction. Since the Ohmic conduction is highly related to the contents of defects inside Gd_2O_3 film, such as oxygen vacancies and metallic defects, a sudden drop on the contribution to total conducting current in branch 3 can be attributed to reducing the contents of defects, especially the metallic Gd defect. Therefore, we

suggest that the switching from LRS to HRS attributed to the oxygen ions migration from bottom ITO electrode to Gd_2O_3 film to re-oxidize with the metallic Gd defects, so the trap-controlled conducting current can be observed at high voltage. The 25 °C-deposited samples with much metallic defects and less oxygen ions inside the oxide films, which reflects a strong Ohmic conducting current on HRS and reluctance to switch back to HRS. In addition, the semiconductor-like behavior on the HRS reveals a structural difference to LRS, which strongly support the reoxidization between metallic Gd defects and migrated oxygen ions. When the applied voltage is low enough (< 0.6 V), the thermally generated carriers are more than the injected carriers from the electrode, so the I-V curve is dominated by Ohmic conduction, as shown in branch 4.

4.5 Conclusion

We successfully fabricated the Gd_2O_3 film for the application on RRAM device at room temperature by pulse laser deposition. The switching characteristics in $Ti/Gd_2O_3/Pt$ capacitor structure is investigated and discussed. XPS analysis data examines the distinction of the chemical composition between pristine and after forming samples, which confirms that the metallic Gd defect inside the Gd_2O_3 films is necessary for the resistance switching behaviors. We also observed that the resistance switching behaviors of $Ti/Gd_2O_3/Pt$ devices are highly correlated with the anode electrode. Under positive bias operation, more than 100 switching characteristics can be observed with low voltage and resistance dispersion, while the switching properties becomes unstable and turn into a large fluctuation on resistance and voltage values when the devices are operated under negative bias. We have explained this phenomenon in terms of the anode material. This work demonstrates the switching properties of Gd_2O_3 film and its dependence on electrode material under a unipolar

operation.

For the T-RRAM devices, highly transparent RRAM devices were successfully fabricated in this work based on ITO/Gd_2O_3/ITO sandwich structure on a glass substrate. The devices exhibit reliable and reproducible resistive switching characteristics under bipolar operation for more than 2000 switching cycles, low operation voltage about 1.6 V, and good data retention for more than 50000 seconds. Based on the results of XPS analysis, the different composition ratio on the metallic (Gd^0) / oxidized (Gd^{3+}) was calculated to be 65.5 % / 34.5 % and 49.3 % / 50.7 % for the 25 °C and 300 °C-deposited samples, respectively. The large amounts of defect in the Gd_2O_3 film, including oxygen vacancies or metal atoms, etc., may greatly dominate the switching characteristics. The Gd_2O_3 particles gain higher kinetic energy to migrate on to the surface and are easier to grow larger grain at 300 °C, resulting in the improvement in crystallinity of Gd_2O_3 film, more densification on film's structure, and lower leakage current. Therefore, a larger high to low resistance ratio can be obtained.

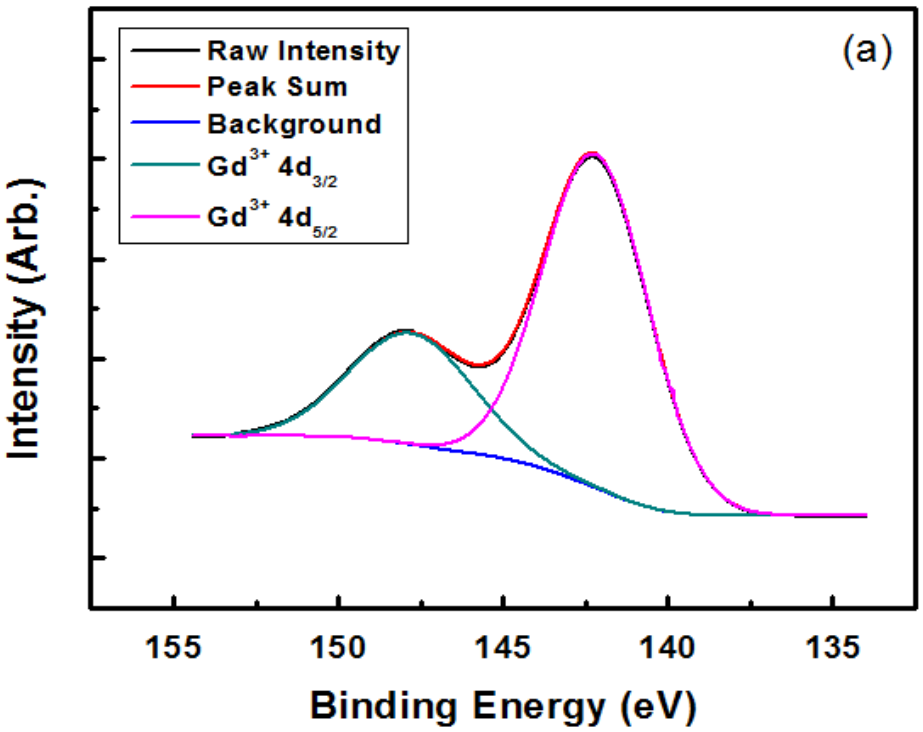

Fig. 4-1 The XPS spectra of the Gd 4p peaks at the initial resistance state.

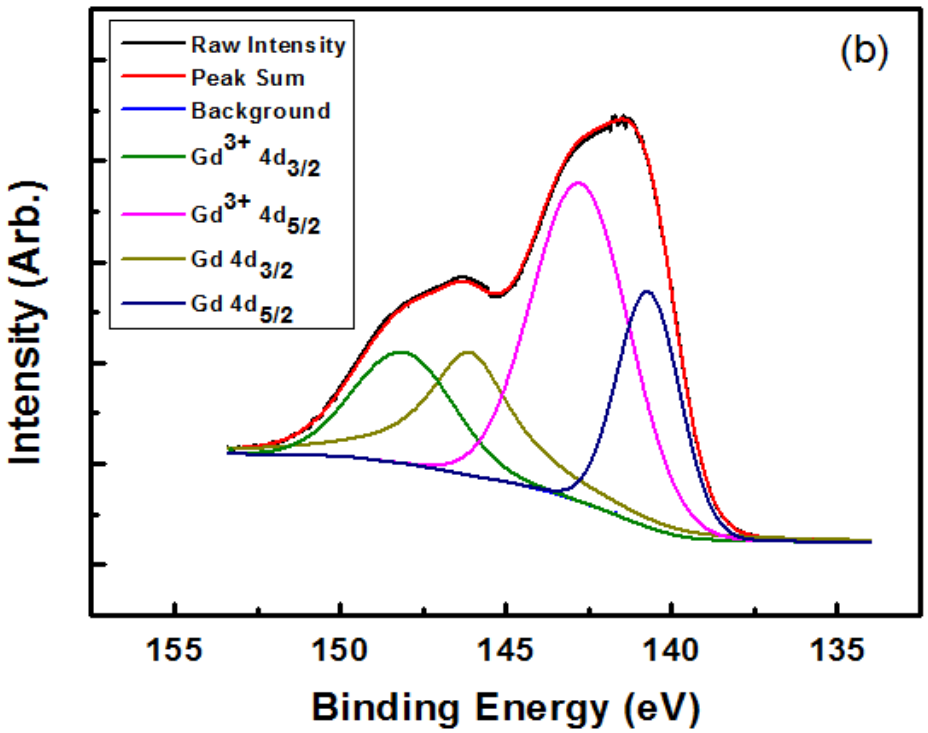

Fig. 4-2 The XPS spectra of the Gd 4p peaks at the low resistance state.

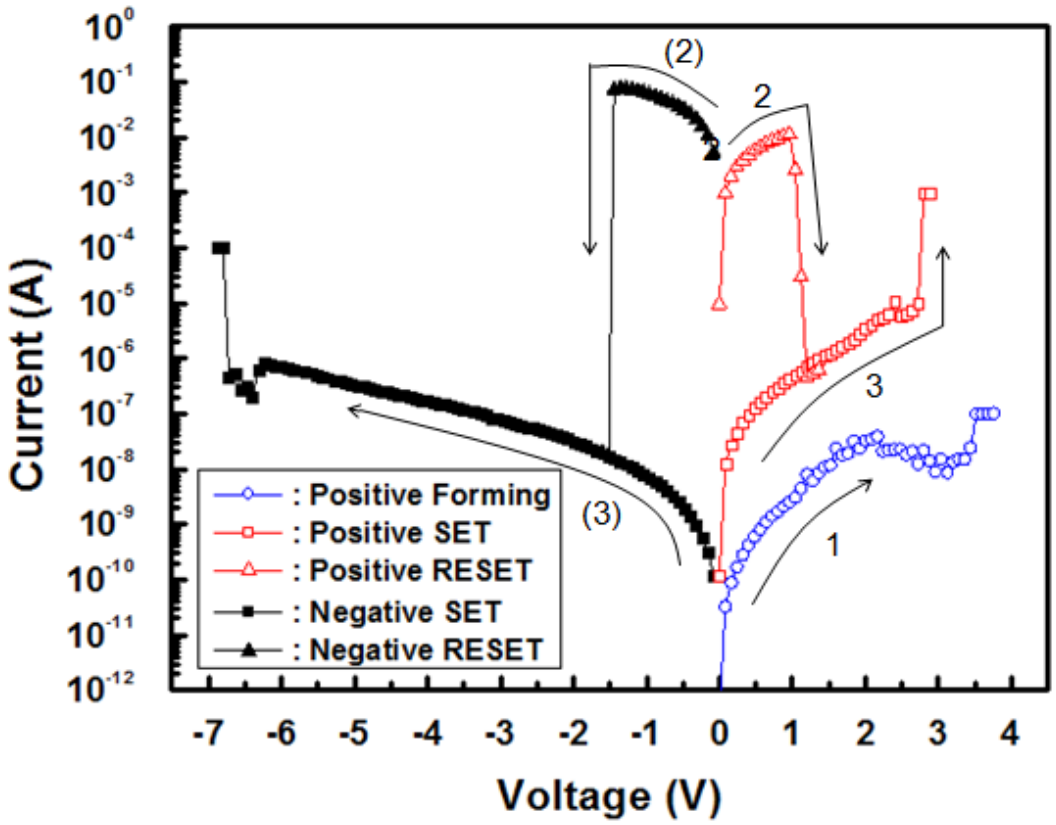

Fig. 4-3 Typical unipolar I-V characteristics of RRAM device based on Ti/Gd_2O_3/Pt capacitor structures. Blue line represents the forming process. Red and black lines represent I-V characteristics under the positive and negative bias operation, respectively.

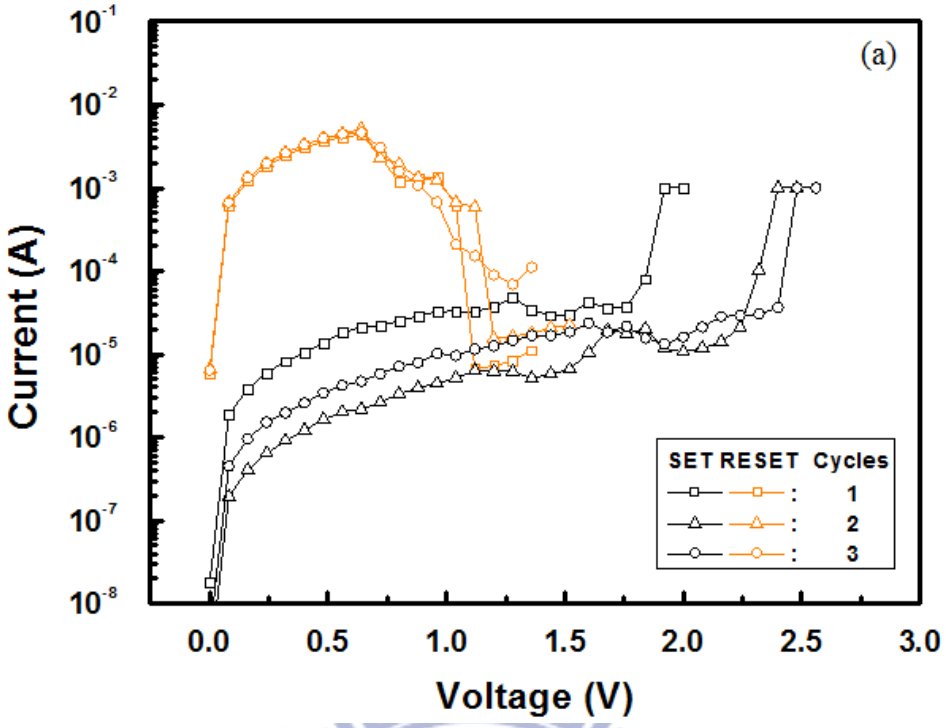

Fig. 4-4 I-V curves of continuous three switching cycles of the Ti/Gd_2O_3/Pt capacitor structures under positive bias operation.

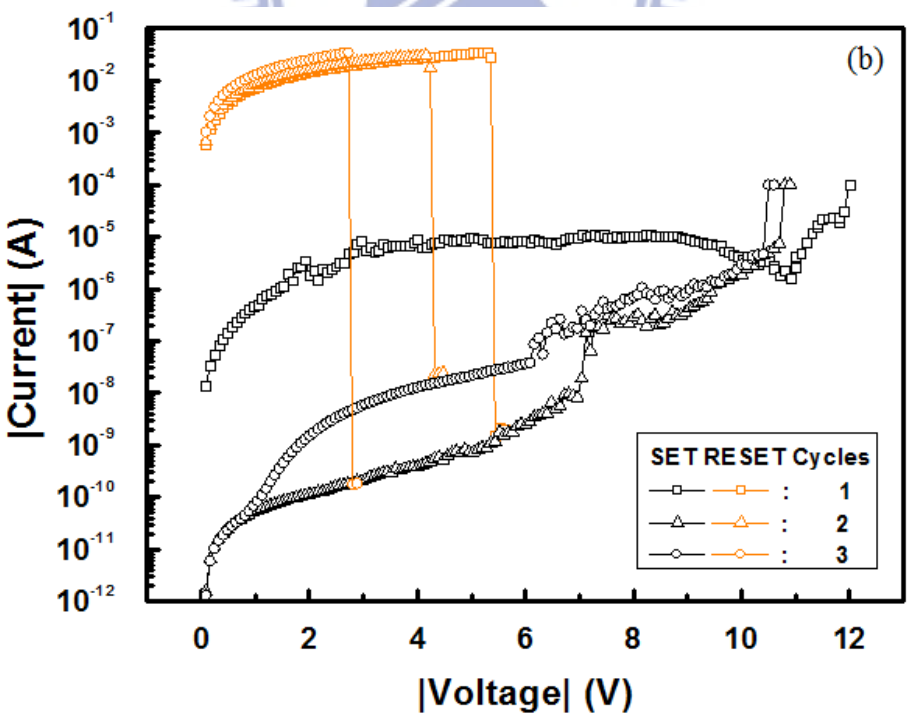

Fig. 4-5 I-V curves of continuous three switching cycles of the Ti/Gd_2O_3/Pt capacitor structures under negative bias operation.

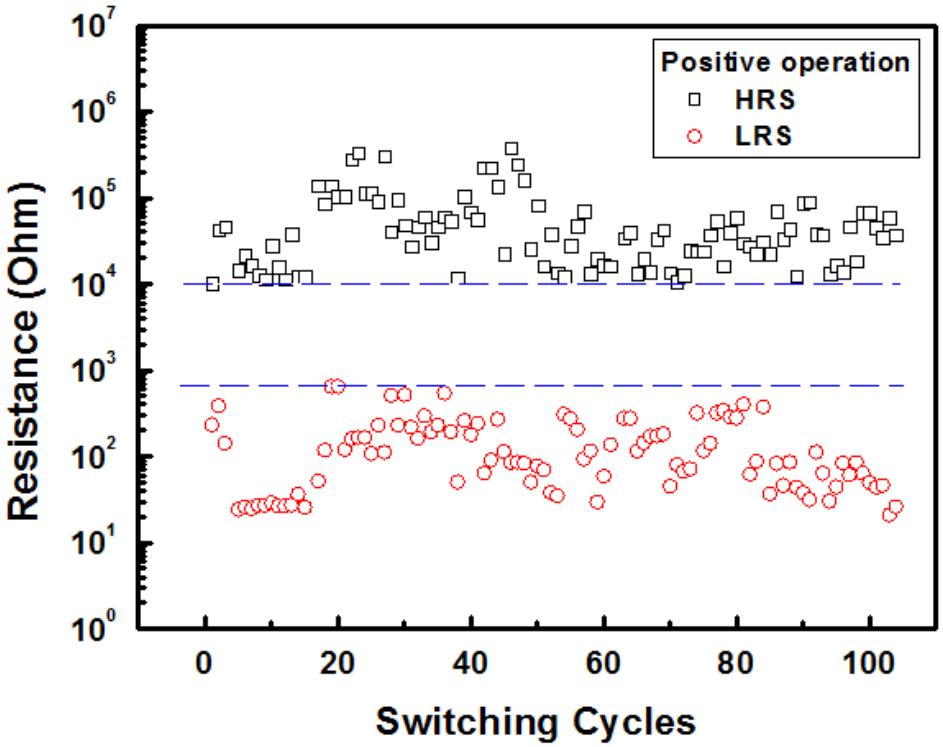

Fig. 4-6 Endurance test of the Ti/Gd_2O_3/Pt capacitor structures under a positive bias operation.

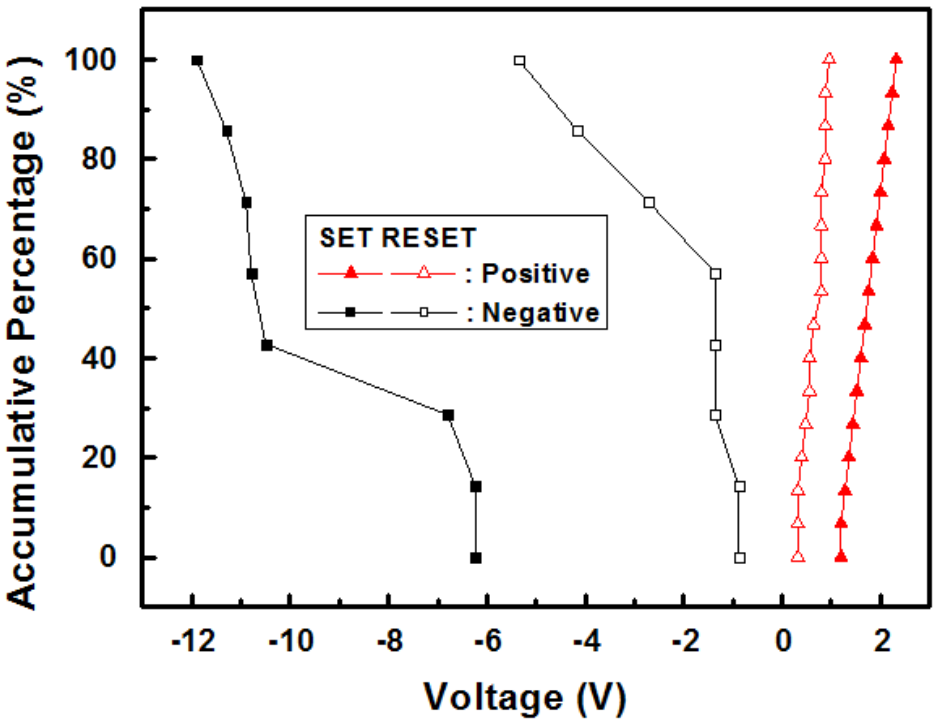

Fig. 4-7 Distribution of the V_{set} and V_{reset} of the Ti/Gd_2O_3/Pt capacitor structures under positive bias operation (up-triangle) and negative bias operation (square).

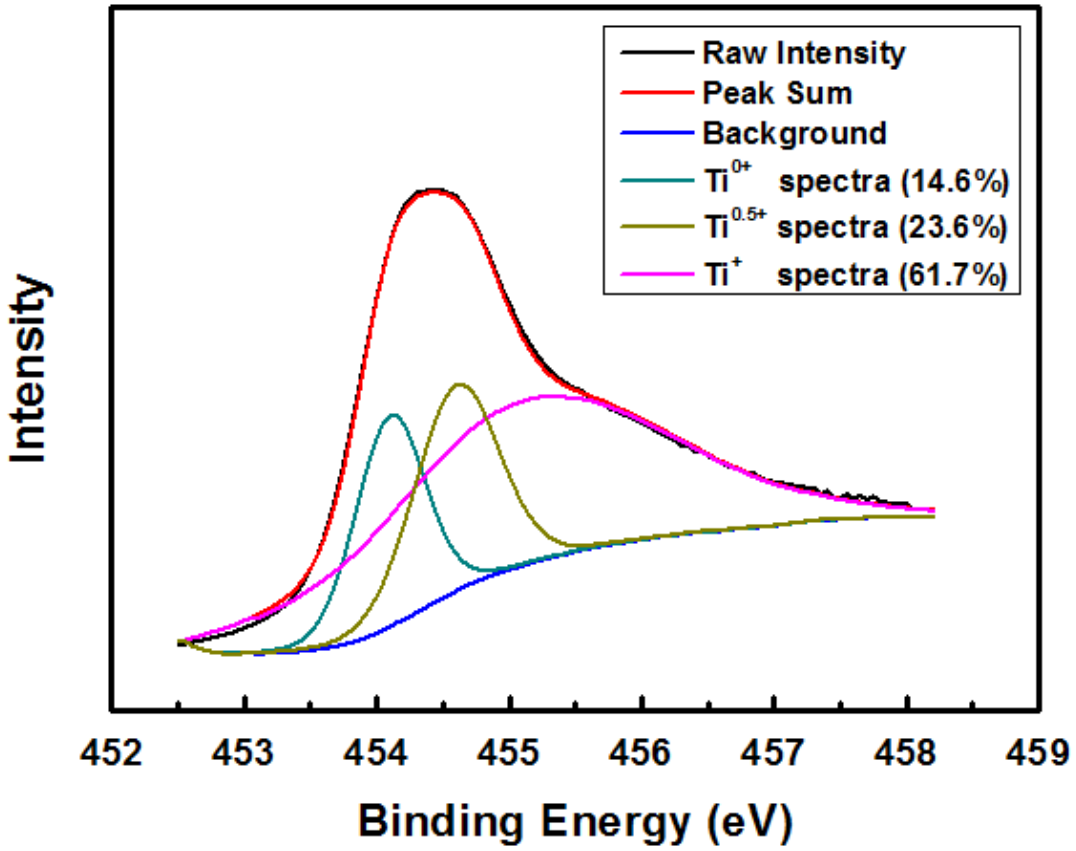

Fig. 4-8 XPS Ti 2p $_{3/2}$ level spectra fitted with Gaussian function of Ti^{0+}, $Ti^{0.5+}$, and Ti^{+} peak.

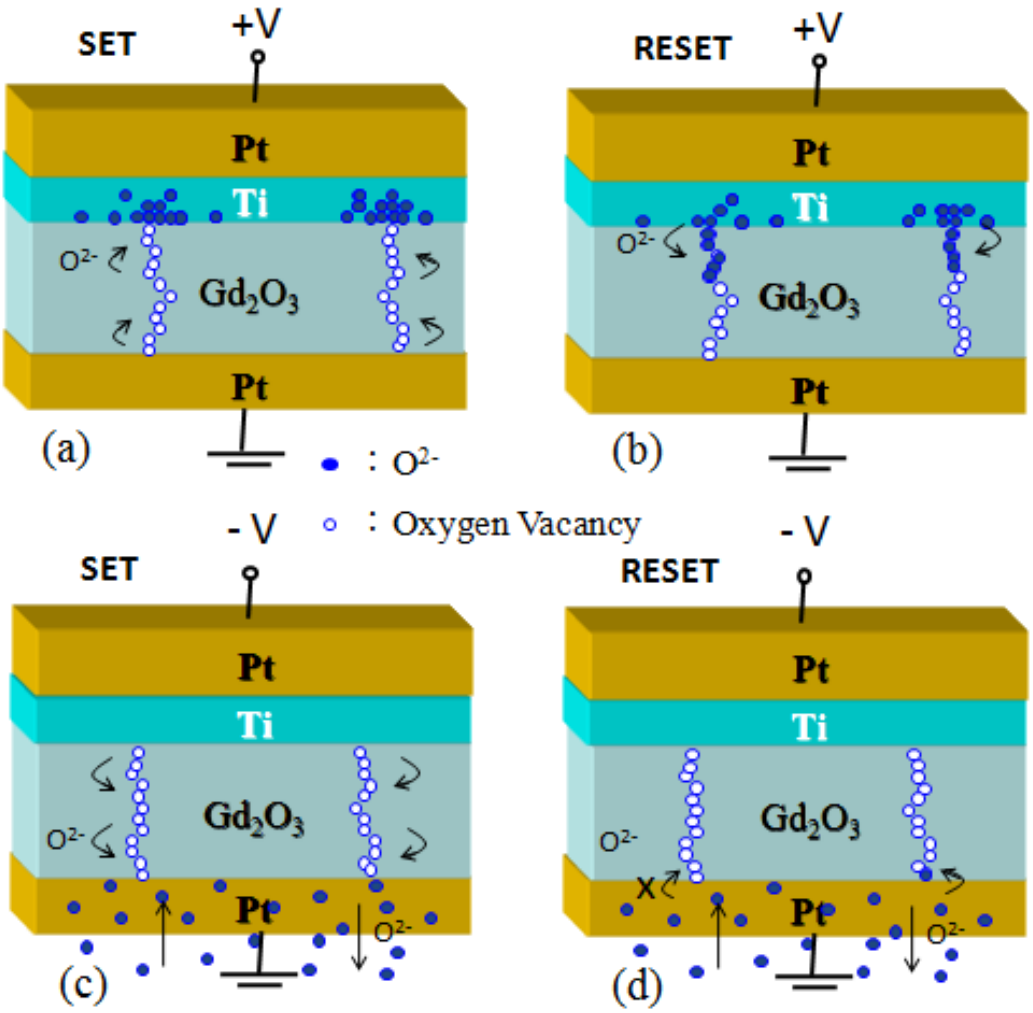

Fig. 4-9 Schematic pictures of the Pt/Ti/Gd_2O_3/Pt structure operated under (a) SET, and (b) RESET process under positive bias, and (c) SET, and (d) RESET process under negative bias operation. Solid and empty circle symbols represent the oxygen ions and oxygen vacancies, respectively.

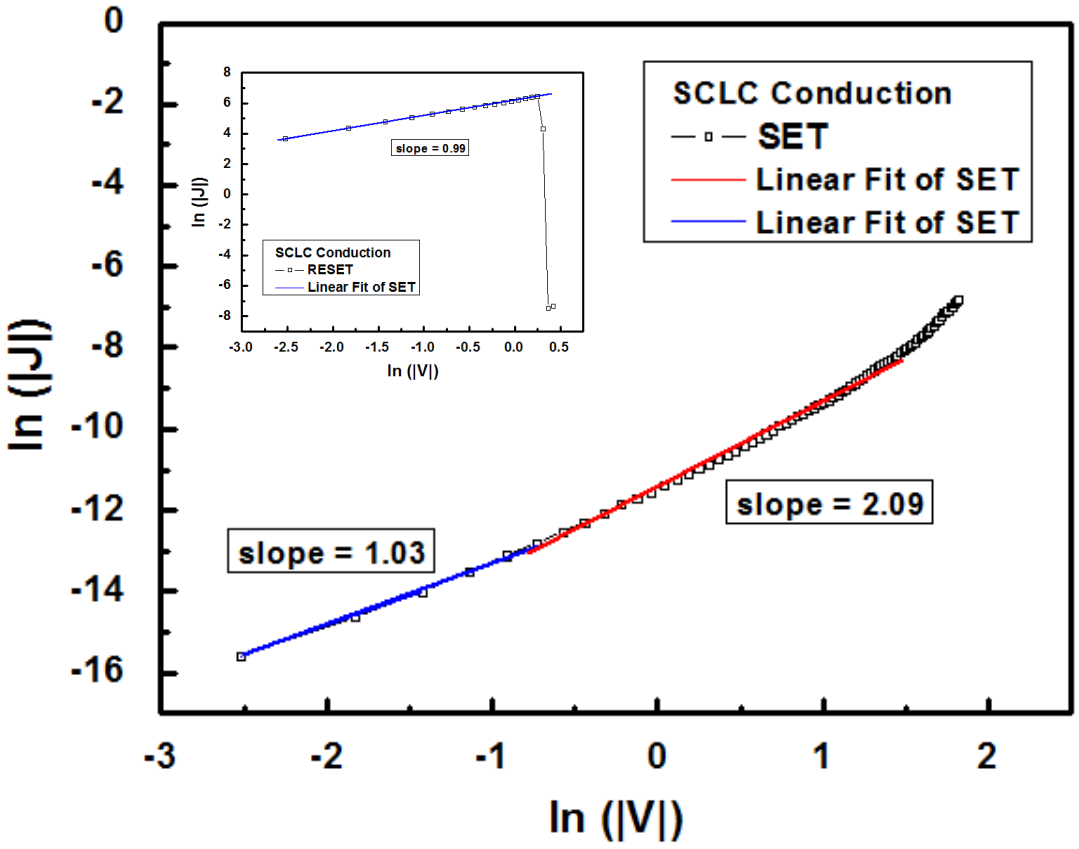

Fig. 4-10 I-V characteristics of the Ti/Gd_2O_3/Pt device plotted in ln (I) – ln (V) scale. Both HRS and LRS are included on the plot.

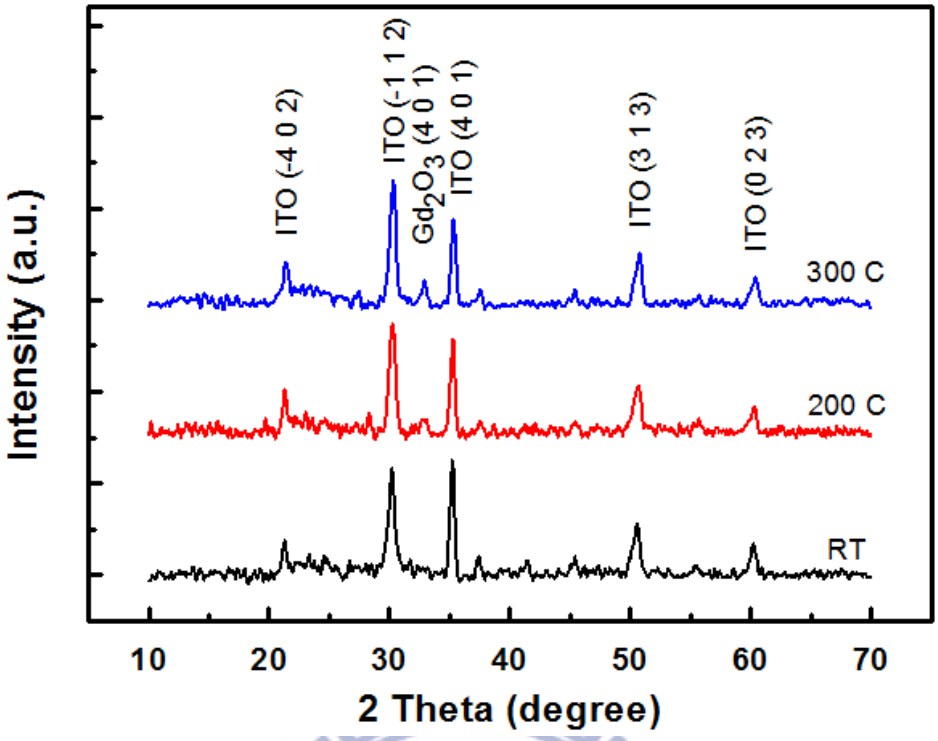

Fig. 4-11 The XRD patterns of the ITO/Gd_2O_3/ITO devices.

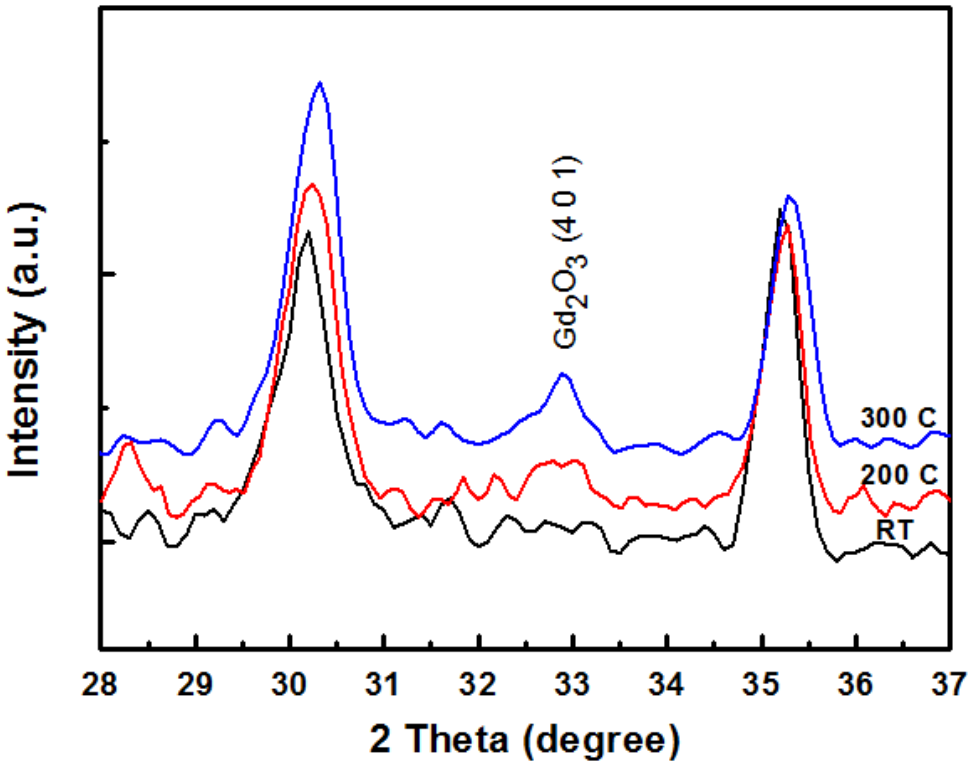

Fig. 4-12 Enlarge image of the XRD patterns of the ITO/Gd_2O_3/ITO devices.

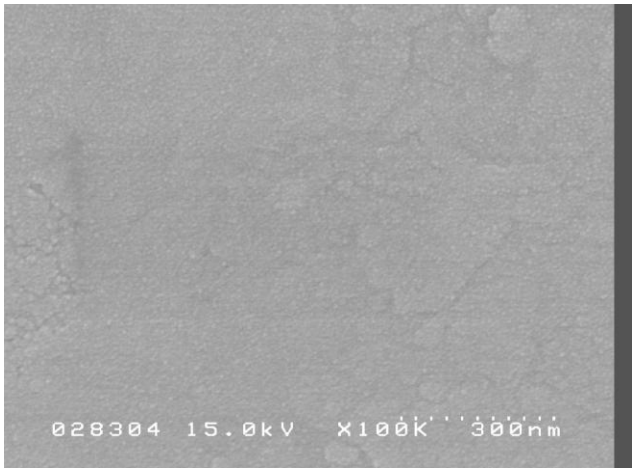

Fig. 4-13 Surface morphology image of the Gd_2O_3 films grown at 25 °C.

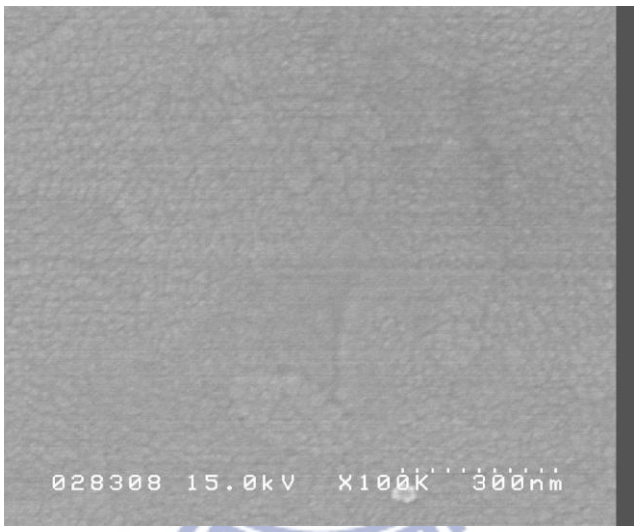

Fig. 4-14 Surface morphology image of the Gd_2O_3 films grown at 200 °C.

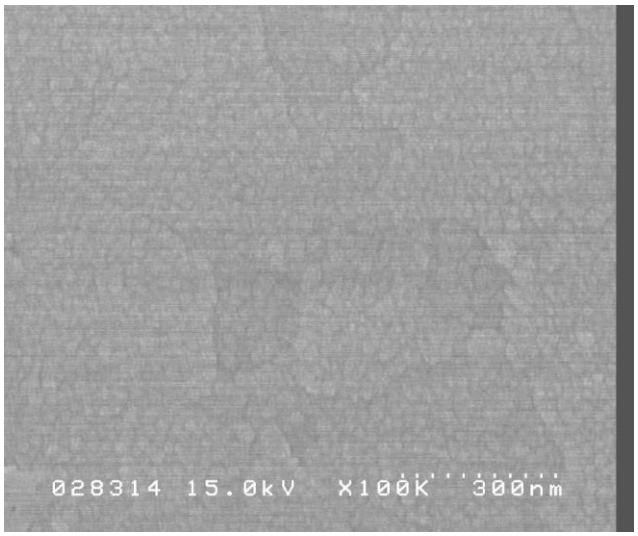

Fig. 4-15 Surface morphology image of the Gd_2O_3 films grown at 300 °C.

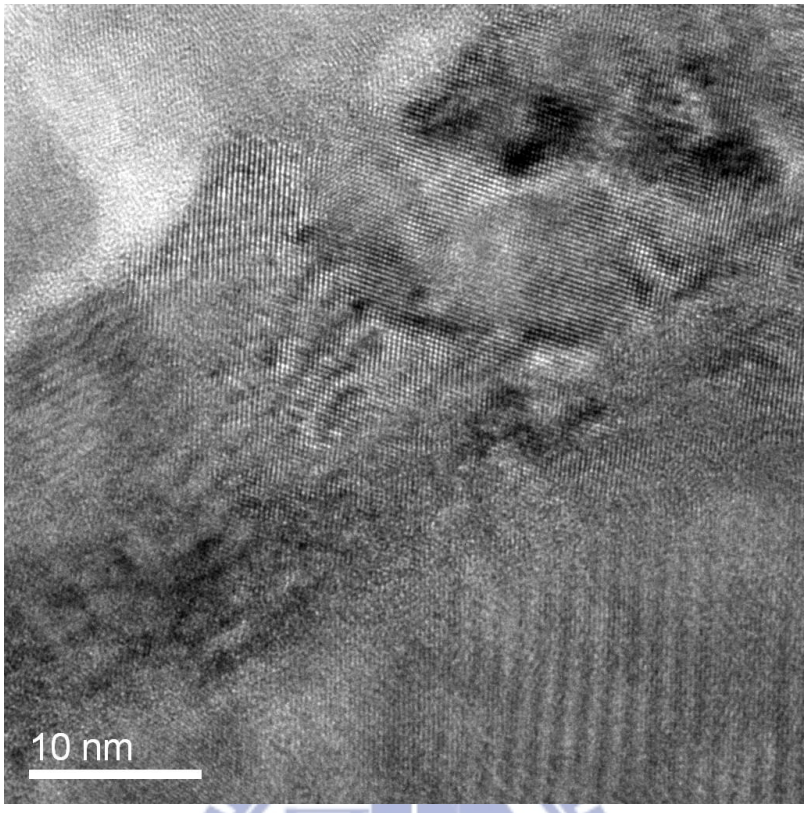

Fig. 4-16 Cross-sectional TEM image of the ITO/Gd_2O_3/ITO films grown at 25 °C.

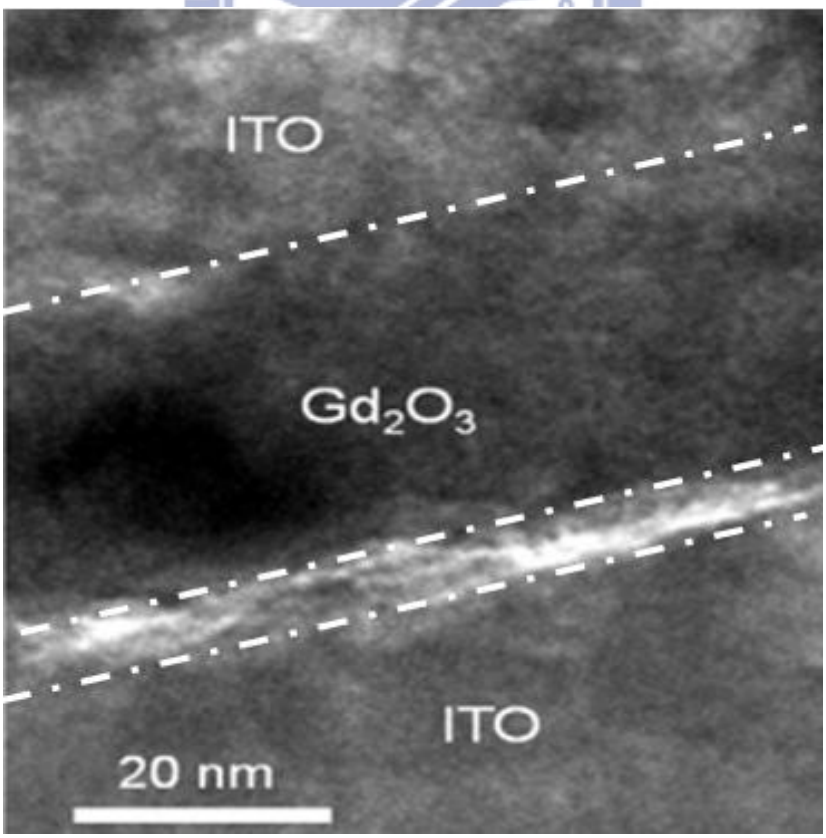

Fig. 4-17 Cross-sectional TEM image of the ITO/Gd_2O_3/ITO films grown at 300 °C.

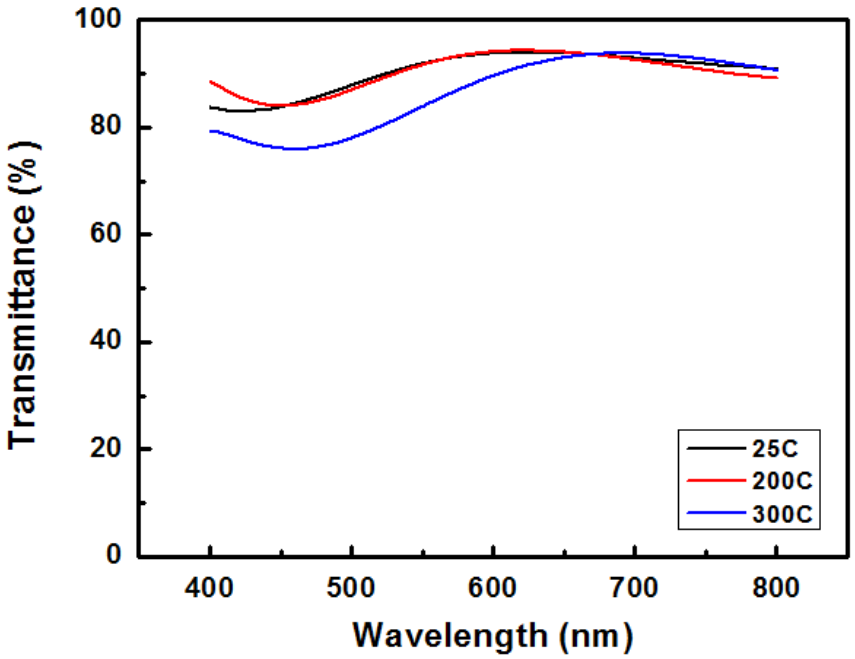

Fig. 4-18 Transmittance of the ITO/Gd_2O_3/ITO structure grown at various growth temperature of 25, 200, and 300 °C under wavelength of visible light in the range of 400-800 nm.

Fig. 4-19 The logo under this transparent ITO/Gd_2O_3/ITO structure is clearly been seen.

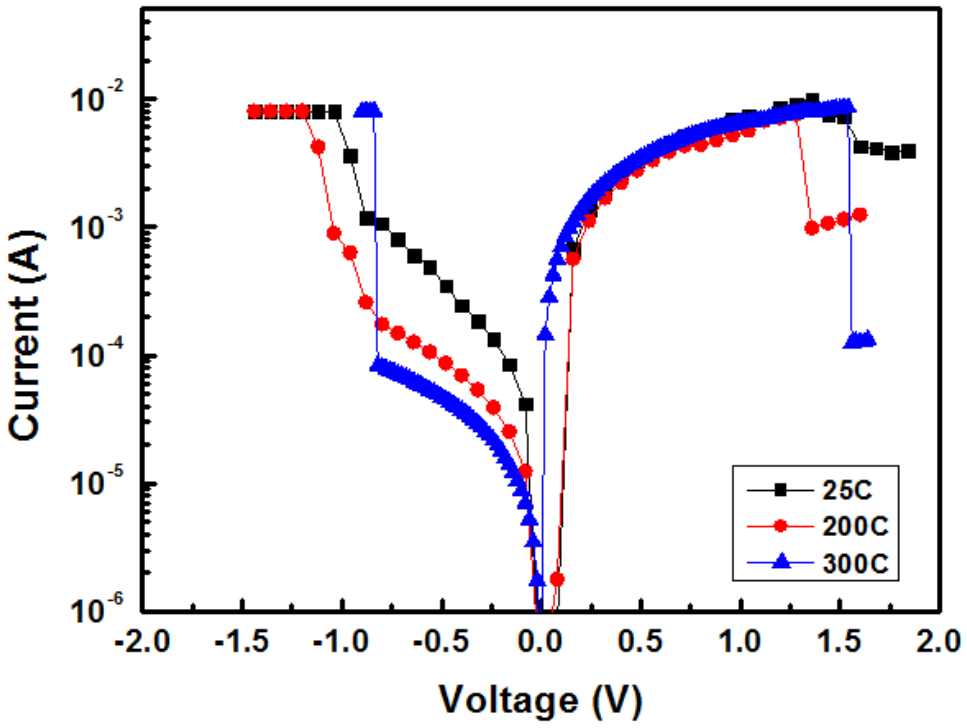

Fig. 4-20 I-V curves of the Gd_2O_3 films grown at various growth temperature of 25, 200, and 300 °C.

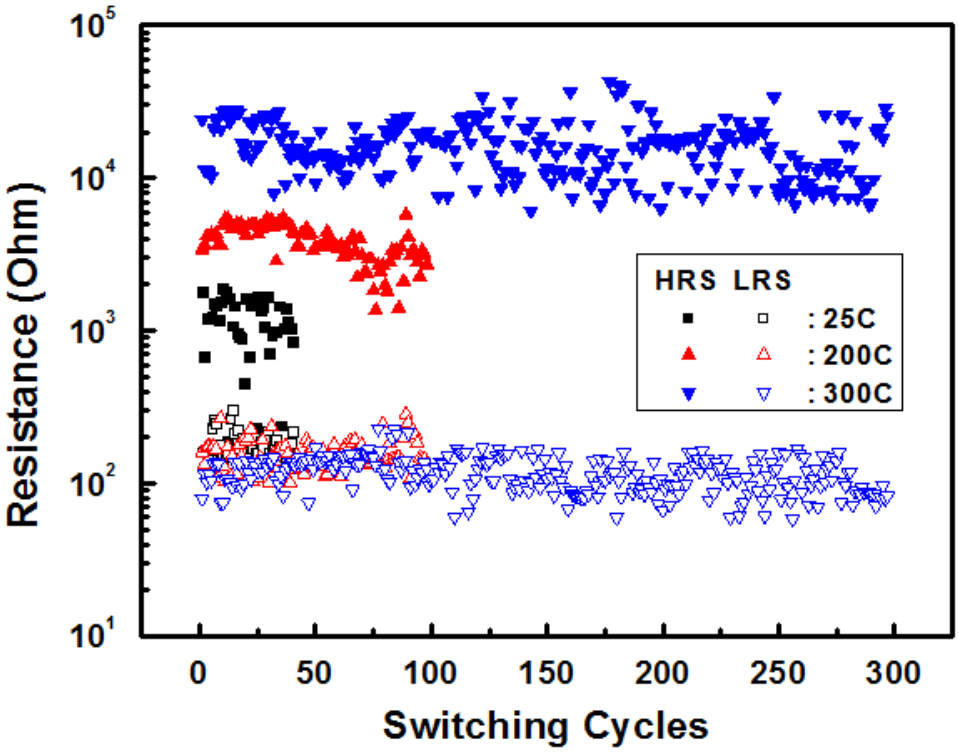

Fig. 4-21 Endurance test of the Gd_2O_3 films grown at various growth temperature of 25, 200, and 300 °C.

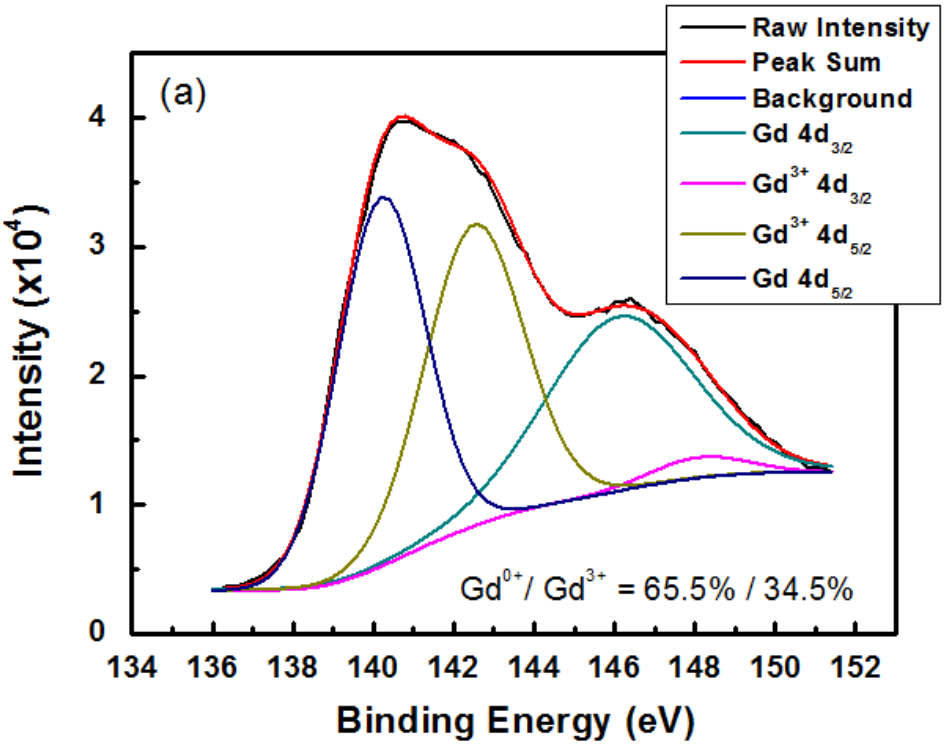

Fig. 4-22 XPS spectra of Gd $4d_{3/2}$, $4d_{5/2}$ and Gd^{3+} $4d_{3/2}$, $4d_{5/2}$ of the Gd_2O_3 films grown at 25 °C.

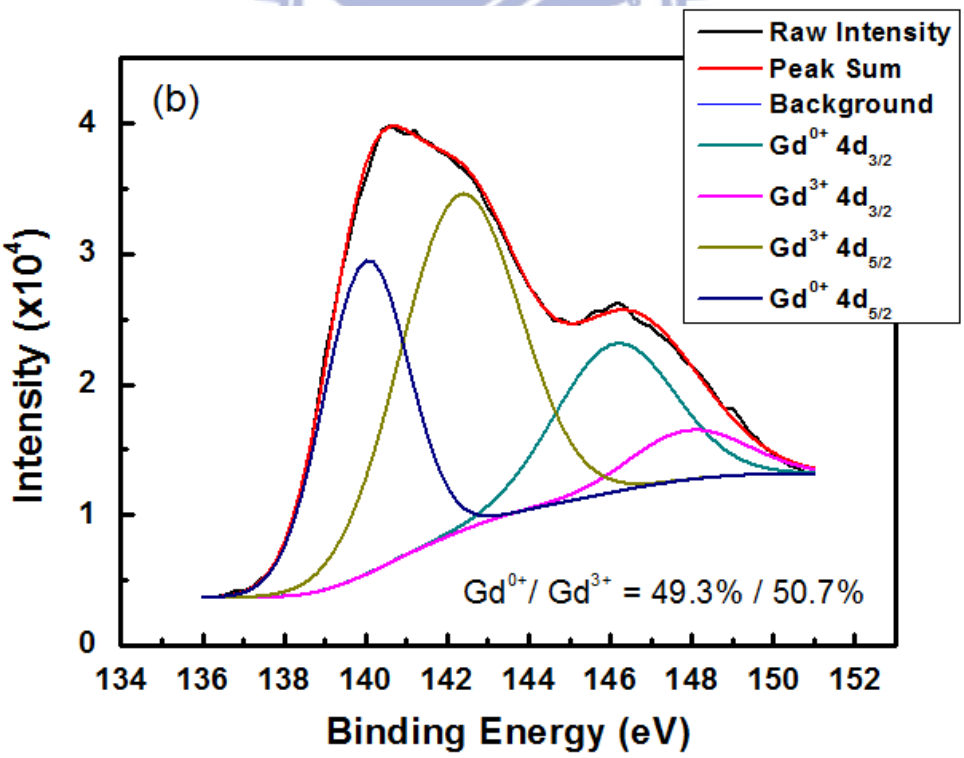

Fig. 4-23 XPS spectra of Gd $4d_{3/2}$, $4d_{5/2}$ and Gd^{3+} $4d_{3/2}$, $4d_{5/2}$ of the Gd_2O_3 films grown at 300 °C.

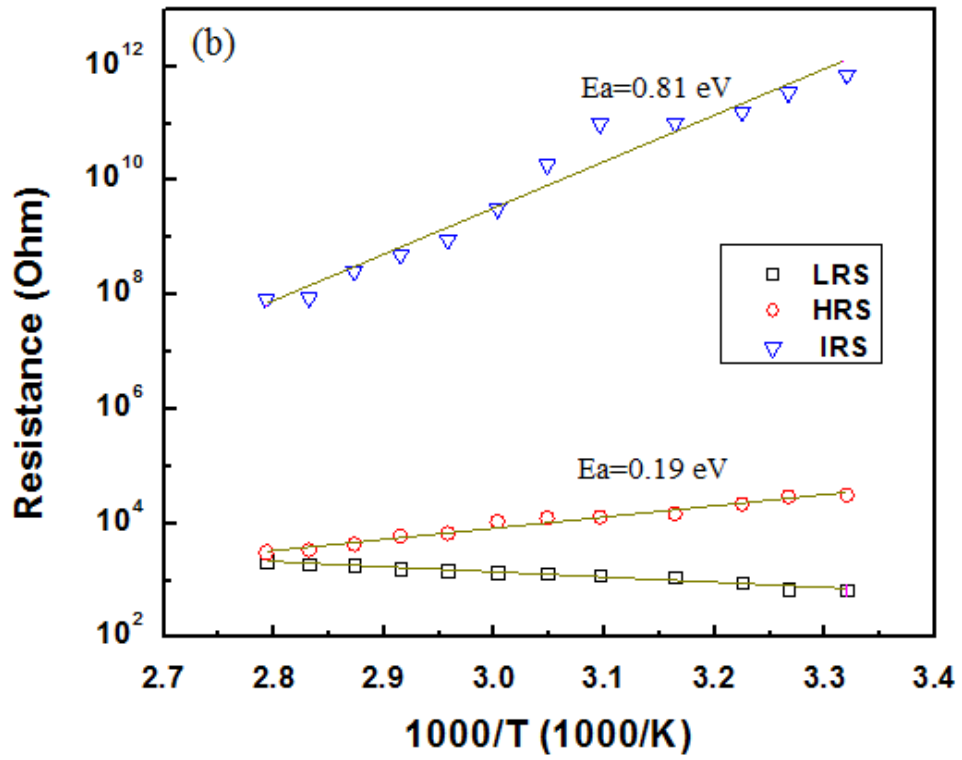

Fig. 4-24 Resistance values of IRS, HRS, and LRS according to temperature of the Gd_2O_3 films grown at 300 °C.

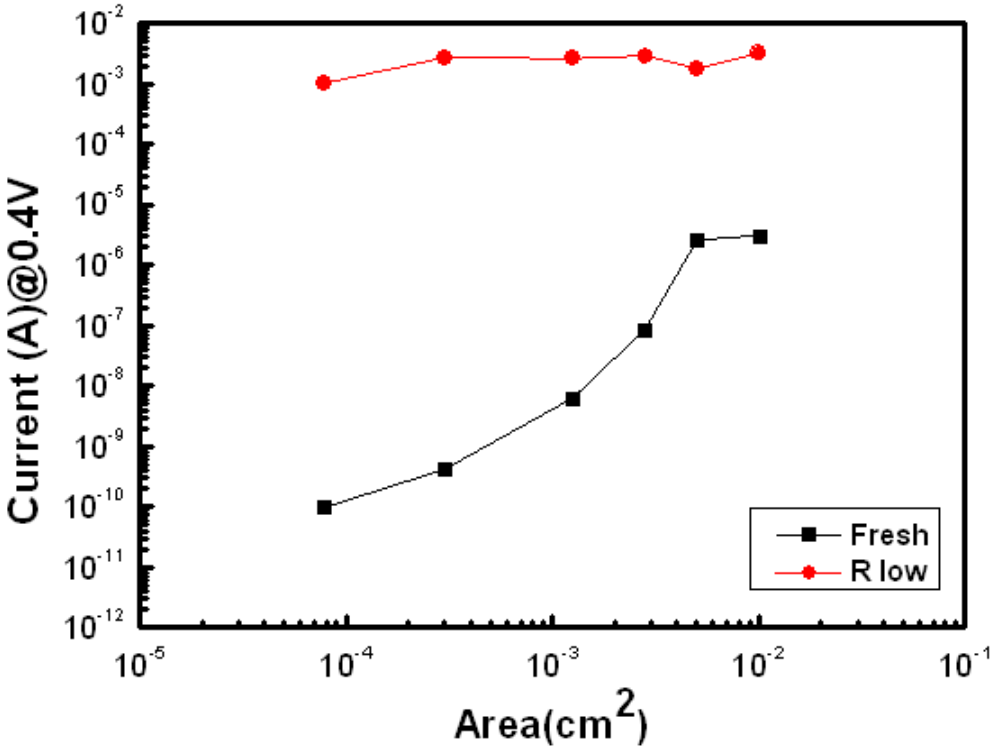

Fig. 4-25 Cell size versus respective IRS and LRS resistance values measured at 0.4 V of the Gd_2O_3 films grown at 300 °C.

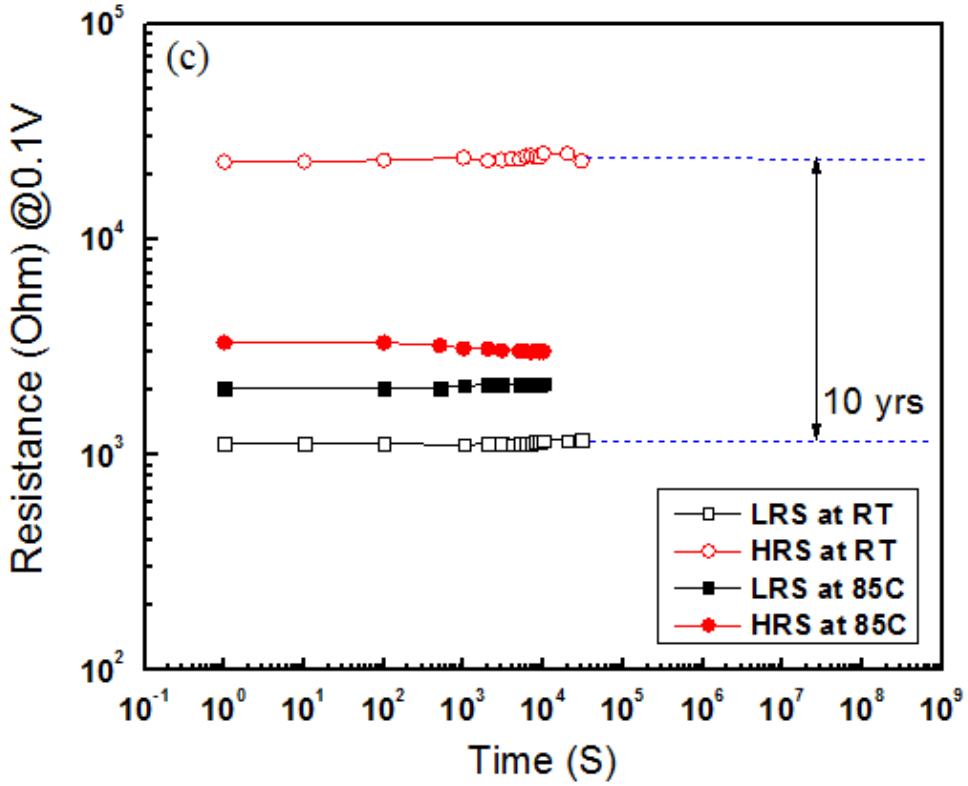

Fig. 4-26 Surface morphology image of the Gd_2O_3 films grown at 300 °C

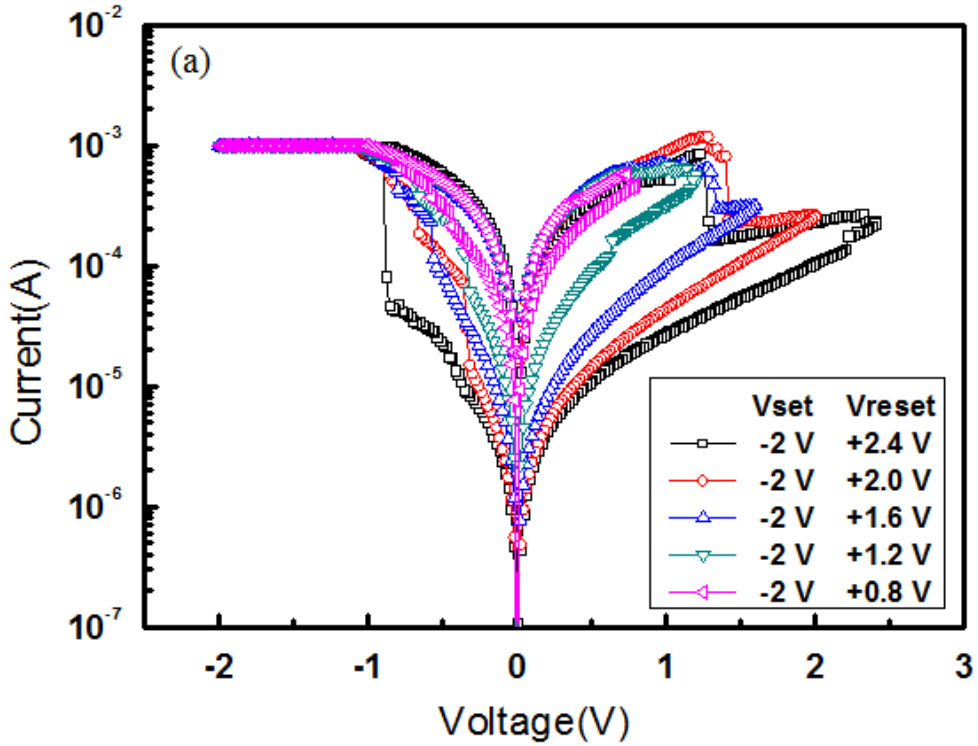

Fig. 4-27 Resistive switching test by applying fixed -2 V for SET but varying the RESET voltage bias from +0.8 to +2.4 V.

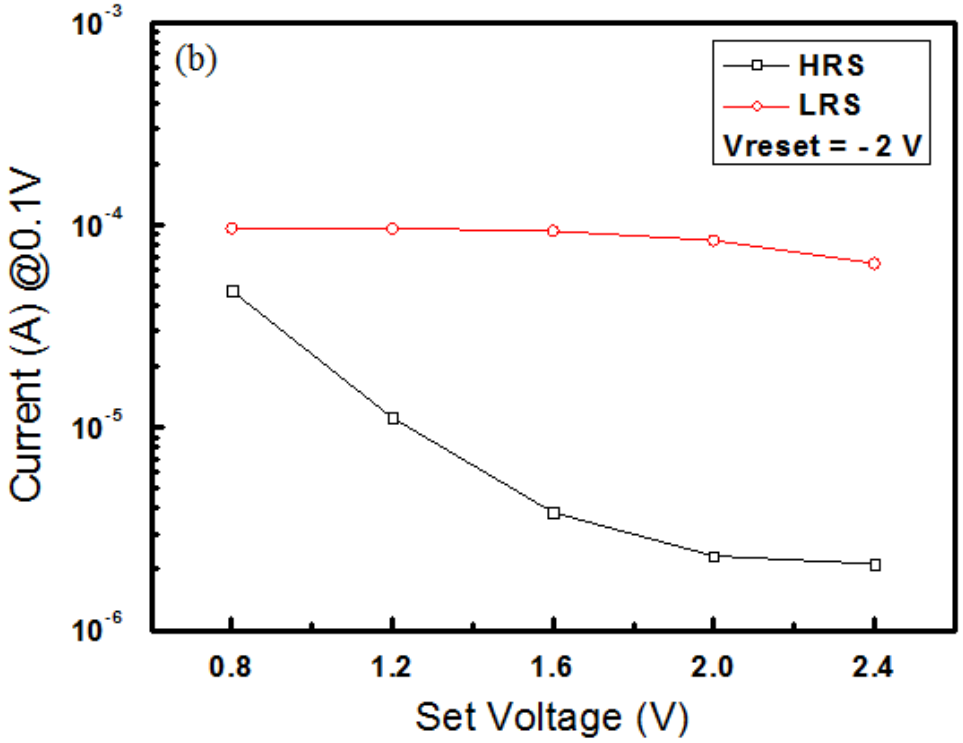

Fig. 4-28 LRS to HRS current ratio at 0.1 V as a function of SET voltage.

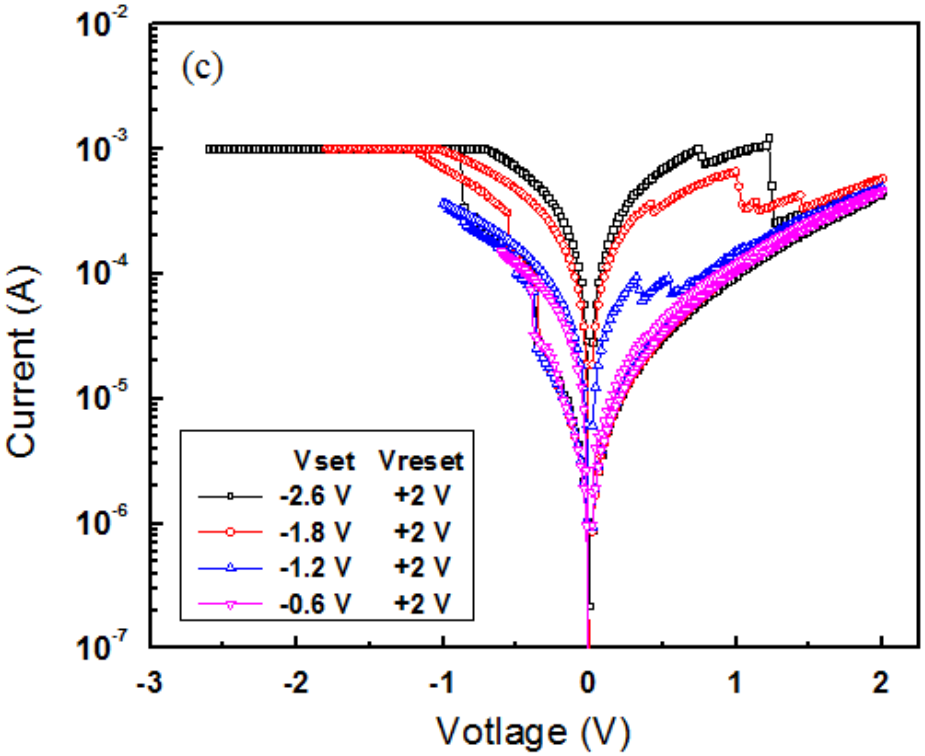

Fig. 4-29 Resistive switching test by applying fixed 2 V for RESET but varying the SET voltage bias from -0.6 to -2.6 V.

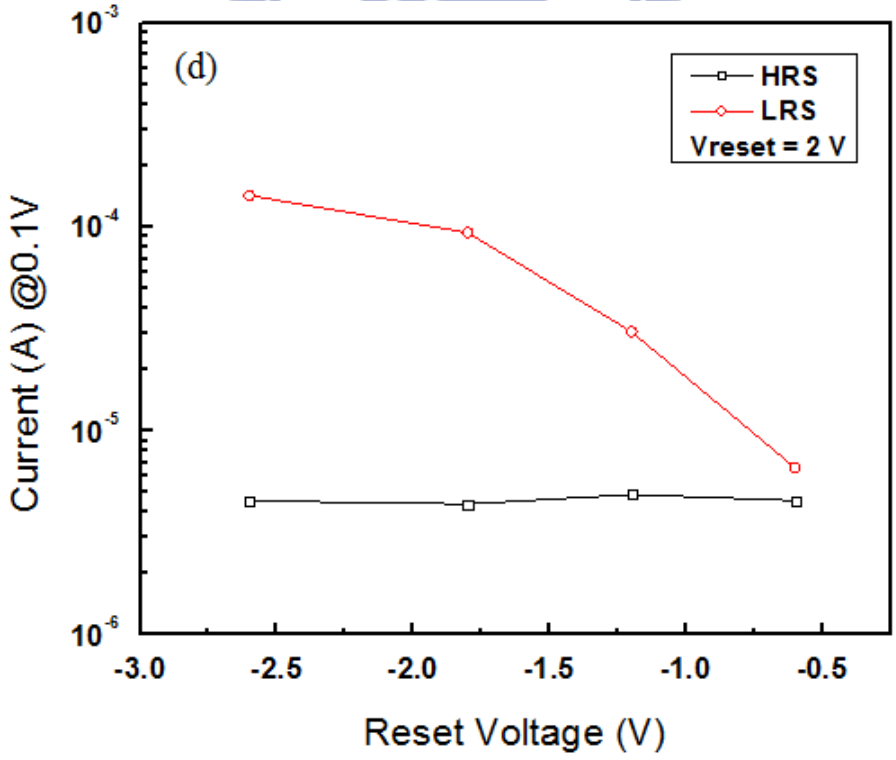

Fig. 4-30 LRS to HRS current ratio at 0.1 V as a function of RESET voltage.

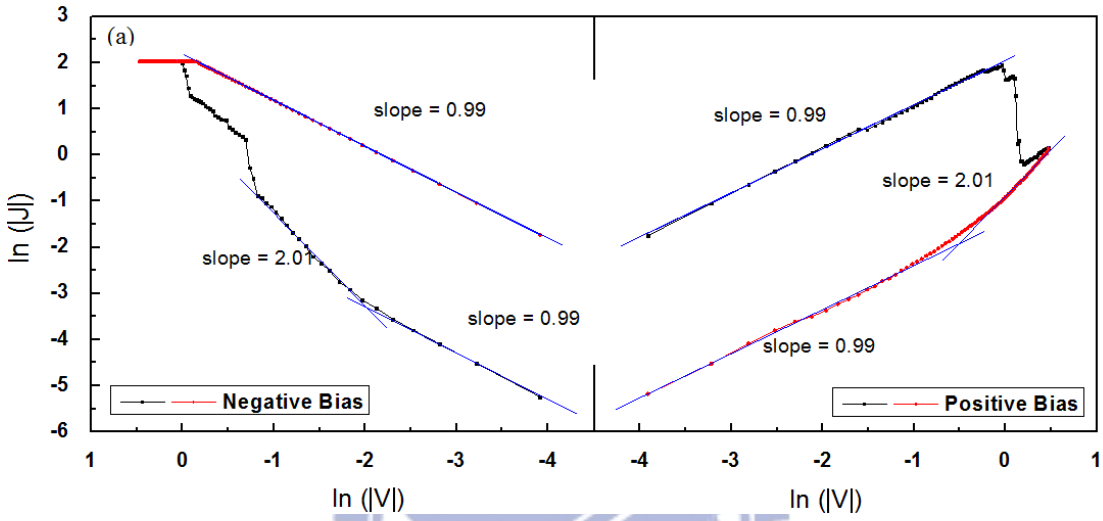

Fig. 4-31 I-V characteristics of both positive and negative bias regions of the ITO/Gd2O3/ITO device plotted in a ln (|J|) - ln (|V|) curve. Both ON-state and OFF-state are included on this plot.